

Aus der Neurologischen Klinik der Universität Heidelberg  
(Geschäftsführender Direktor: Prof. Dr. med. Wolfgang Wick)  
Abteilung für Neuroradiologie  
(Ärztlicher Direktor: Prof. Dr. med. Martin Bendszus)

# Effect of Gradient Vectors Scheme and Noise Correction on Fractional Anisotropy in Diffusion Tensor Imaging of the Peripheral Nervous System

Inauguraldissertation  
zur Erlangung des Doctor scientiarum humanarum (Dr.sc.hum.)  
an der  
Medizinischen Fakultät Heidelberg  
der  
Ruprecht-Karls-Universität

vorgelegt von  
M.Eng. (Biomedical Engineering) Bo Ma  
aus  
Peking  
2019

Dekan: Prof. Dr. med. Andreas Draguhn

Doktormutter: Prof. Dr. rer. nat. Dipl.-Phys. Sabine Heiland



# TABLE OF CONTENTS

<b>LIST OF TABLES .....</b>	<b>III</b>
<b>LIST OF FIGURES .....</b>	<b>IV</b>
<b>LIST OF SYMBOLS AND ABBREVIATIONS.....</b>	<b>V</b>
<b>1 INTRODUCTION .....</b>	<b>1</b>
1.1 General Description of Diffusion Tensor Imaging (DTI).....	2
1.1.1 Concept of Self-Diffusion and its Development to DTI.....	2
1.1.2 Derivation of Diffusion Tensor D and Anisotropy Indices in MRI.....	5
1.1.3 DTI in Peripheral Nerves.....	17
1.2 DTI Limitations on PNS.....	18
1.2.1 Selection of Gradient Vectors Scheme .....	19
1.2.2 Noise Impact on Anisotropy Indices .....	20
1.3 Aim of the Project.....	22
<b>2 MATERIAL UND METHOD.....</b>	<b>23</b>
2.1 Tailored Diffusion Gradient Scheme for Peripheral Nerves.....	23
2.1.1 General Requirements for Gradient Vector Numbers.....	23
2.1.2 Tailored Gradient Vector Scheme for Peripheral Nerves .....	24
2.1.3 Conventional Gradient Vector Schemes .....	40
2.2 Noise Correction.....	44
2.2.1 Noise propagation in DTI.....	44
2.2.2 Noise correction methods .....	48
2.2.3 Options of Signal Combination in Practice .....	51
2.3 Phantom Experiments.....	52
2.3.1 Peripheral Nerve Phantom.....	52
2.3.2 MR System and Protocol.....	53
2.3.3 Post-processing of Acquired MRI Data.....	54
<b>3 RESULTS .....</b>	<b>56</b>
3.1 Tailored Gradient Vectors Scheme .....	56
3.1.1 Coverage of the DGV scheme .....	56
3.1.2 Finding the Optimum DGV .....	61
3.1.3 Validation of simulation results in Phantom study .....	62
3.1.4 Comparison with Established Gradient Schemes.....	64
3.2 Noise Correction.....	67
3.2.2 Noise propagation correction.....	67

<b>4</b>	<b>DISCUSSION</b> .....	<b>76</b>
4.1	Tailored diffusion gradient scheme for peripheral nerves .....	76
4.2	Robust noise correction method in DTI .....	78
<b>5</b>	<b>SUMMARY</b> .....	<b>81</b>
<b>6</b>	<b>REFERENCES</b> .....	<b>85</b>
<b>7</b>	<b>PAPERS PUBLISHED</b> .....	<b>93</b>
<b>8</b>	<b>CURRICULUM VITAE</b> .....	<b>94</b>
<b>9</b>	<b>ACKNOWLEDGEMENT</b> .....	<b>96</b>
<b>10</b>	<b>EIDESSTAATLICHE VERSICHERUNG</b> .....	<b>97</b>

**LIST OF TABLES**

Table 2.1: FA, b value and corresponding derived diagonal tensor.....	33
Table 2.2: SIEMENS gradient Schemes.....	41
Table 2.3: Jones gradient schemes.....	42
Table 2.4: DSM Schemes .....	43
Table 2.5: Table of variables used in the noise correction.....	48
Table 3.1: Final Optimal DGV Schemes .....	63

## LIST OF FIGURES

Figure 1.1: Particle path of a molecule experiencing 3-dimensional Brownian motion ..	3
Figure 1.2: Diagram example of the Stejskal-Tanner diffusion gradients.....	10
Figure 1.3: The comparison of phase changes .....	11
Figure 1.4: Diffusion measurements example .....	13
Figure 1.5: Eigenvalues $\lambda_1$ $\lambda_2$ and $\lambda_3$ along corresponding eigenvectors.....	15
Figure 2.1: Comparison between conventional scheme and DGV scheme.....	25
Figure 2.2: Diffusion propagator of the nerve tissue (Orientation: Z-direction).....	26
Figure 2.3: Cross section displaying the diffusion propagator .....	27
Figure 2.4: Example of DGV with N=6 .....	31
Figure 2.5: Coordinate systems of the scanner and nerve .....	35
Figure 2.6: Phantom description.....	53
Figure 2.7: Data sets extraction for the inputs of FA derivation in MATLAB program	55
Figure 3.1: Result of the simulation for DGV with N=6.....	57
Figure 3.2: Result of the simulation for DGV with N=10.....	58
Figure 3.3: Result of the simulation for DGV with N=20.....	59
Figure 3.4: Result of the simulation for DGV with N=30.....	60
Figure 3.5: Condition Number CN as function of $\Theta_{\max}$ and N .....	61
Figure 3.6: FA determined from the phantom experiments for different N and $\Theta_{\max}$ ....	62
Figure 3.7: Comparison of the optimum Directional Gradient Vector schemes .....	64
Figure 3.8: Simulation results of Fractional Anisotropy (FA) for N=6 and N=30 .....	66
Figure 3.9: Efficacy of different noise correction methods: the simulation .....	68
Figure 3.10: Efficacy of different noise correction methods: the phantom measurements results with coil combination by Sum-Of-Squares (SOS).....	69
Figure 3.11: Phantom measurement with coil combination by Sum-Of-Squares (SOS). (a): histograms of noise and signal intensity .....	70
Figure 3.12: Efficacy of different noise correction methods: the phantom measurements results with coil combination by Adaptive Combine (AC) .....	71
Figure 3.13: Phantom measurement with coil combination by Adaptive Combine (AC). (a): histograms of noise and signal intensity .....	72
Figure 3.14: Efficacy of different noise correction methods: the simulation study results with N=30 .....	73
Figure 3.15: Efficacy of different noise correction methods: the phantom measurements results with N=30.....	74
Figure 3.16: Histograms of noise distribution for N=30 resulting from simulation and phantom experiment .....	75

## LIST OF SYMBOLS and ABBREVIATIONS

$\lambda_1$ :	.....	maximum eigenvalue in Z direction.
$\lambda_2$ :	.....	symmetry eigenvalue either in X or Y direction.
$\lambda_3$ :	.....	symmetry eigenvalue either in X or Y direction.
<b>3D</b> :	.....	three Dimensions.
<b>A</b> :	.....	true signal intensity.
<b>AC</b> :	.....	Adaptive Combine.
<b>AD</b> :	.....	Axial Diffusivity.
<b>ADC</b> :	.....	Apparent Diffusion Coefficient.
<b>b</b> :	.....	b-value.
<b>b<sub>0</sub></b> :	.....	b value is 0.
<b>CN</b> :	.....	Condition Number.
<b>CNS</b> :	.....	Central Nervous System.
<b>D</b> :	.....	Diffusion coefficient.
<b>D<sub>0</sub></b> :	.....	true diffusion tensor derived from predefined parameters.
<b>DGV</b> :	.....	Directional Gradient Vector scheme.
<b>D<sub>n</sub></b> :	.....	calculated tensor according to noise contaminated data.
<b>dPNP</b> :	.....	diabetic polyneuropathy.
<b>DSM</b> :	.....	Downhill Simplex Minimization.
<b>DTI</b> :	.....	Diffusion Tensor Imaging.
<b>DW MRI</b> :	.....	Diffusion-Weighted Magnetic Resonance Imaging.
<b>DWI</b> :	.....	Diffusion Weighted Imaging.
<b>E</b> :	.....	transformation matrix composed by eigenvectors.
<b>EPI</b> :	.....	Echo-Planar Imaging.
<b>FA</b> :	.....	Fractional Anisotropy.
<b>FA<sub>median</sub></b> :	.....	median FA value.
<b>FWHM</b> :	.....	Full Width at Half Maximum.
<b>G</b> :	.....	amplitude of diffusion gradient pulse.
<b>g<sub>k</sub></b> :	.....	gradient vector.
<b>LS</b> :	.....	Least-Squares.
<b>M</b> :	.....	sum of magnetic moments or measured signal intensity.
<b>M<sub>0</sub></b> :	.....	Noise only signal intensity.
<b>MATLAB</b> :	.....	MATrix LABoratory developed by MathWorks.
<b>MD</b> :	.....	Mean Diffusivity.
<b>MDDW</b> :	.....	Multi-Directional Diffusion Weighting.
<b>MR</b> :	.....	Magnetic Resonance.
<b>MSD</b> :	.....	Mean Square Displacement.
<b>n</b> :	.....	Gaussian noise.
<b>N</b> :	.....	Number of diffusion gradient sampling directions.
<b>N<sub>A</sub></b> :	.....	repeating observation times.
<b>n<sub>i</sub></b> :	.....	imaginary part of Gaussian noise.
<b>n<sub>r</sub></b> :	.....	real part of Gaussian noise.
<b>PDF</b> :	.....	Probability Density Function.
<b>PNS</b> :	.....	Peripheral Nervous System.
<b>RD</b> :	.....	Radial Diffusivity.
<b>RF</b> :	.....	Radio Frequency.



## LIST OF SYMBOLS and ABBREVIATIONS

<b>ROI:</b>	.....	<i>Region of Interest.</i>
<b>S<sub>0</sub>:</b>	.....	<i>signal intensity without diffusion weight.</i>
<b>S<sub>k</sub>:</b>	.....	<i>signal intensity with certain diffusion gradient pulse g<sub>k</sub>.</i>
<b>SNR:</b>	.....	<i>Signal-to-Noise Ratio.</i>
<b>SOS:</b>	.....	<i>Sum-Of-Squares.</i>
<b>T<sub>1</sub>:</b>	.....	<i>spin-lattice relaxation time.</i>
<b>T<sub>2</sub>:</b>	.....	<i>spin-spin relaxation.</i>
<b>TE:</b>	.....	<i>echo time.</i>
<b>t<sub>Δ</sub> :</b>	.....	<i>a given time period.</i>
<b>x :</b>	.....	<i>distance over a given time period.</i>
<b>x<sub>0</sub>:</b>	.....	<i>initial position of a random moving particle.</i>
<b>γ :</b>	.....	<i>gyromagnetic ratio which is 42 MHz/Tesla for water proton spin.</i>
<b>δ :</b>	.....	<i>diffusion gradient pulse duration.</i>
<b>Δ :</b>	.....	<i>the time interval of diffusion gradients.</i>
<b>θ :</b>	.....	<i>angle between gradient vector and Z axis.</i>
<b>Θ:</b>	.....	<i>fiber orientation angle.</i>
<b>Θ<sub>max</sub>:</b>	.....	<i>the angle which defines the cone opening.</i>
<b>μ :</b>	.....	<i>mean of Gaussian distribution.</i>
<b>ρ :</b>	.....	<i>proton density.</i>
<b>σ :</b>	.....	<i>variance of Gaussian distribution.</i>
<b>Σ :</b>	.....	<i>covariance matrix.</i>
<b>φ :</b>	.....	<i>angle between the projection of the gradient vector on X-Y plane and X axis.</i>

# 1 INTRODUCTION

Diffusion Weighted Magnetic Resonance Imaging (DW MRI) is a magnetic resonance imaging technique which uses specifically designed sequences to detect the characteristics of the Brownian Motion phenomena of water molecules contained in biological tissues. As a novel sequence technique around the middle of 1980s (Le Bihan *et al.*, 1986), Diffusion Weighted Imaging (DWI) indeed led to many exciting applications in MRI clinical routine (Baliyan *et al.*, 2016). With decades of constant developments, more advanced technologies such as Diffusion Tensor Imaging (DTI) became an irreplaceable diagnosis method in current MR neuroimaging (Tae *et al.*, 2018). Compared with earlier DWI, the sequence optimization led to a reduced acquisition time (Baete *et al.*, 2013), less susceptibility to motion (Taylor *et al.*, 2016) and higher reliability of the derived parameters (Wang *et al.*, 2012) which in turn increased the interest of clinicians and researchers in this technique.

Several quantitative parameters can be determined from DTI: Fractional Anisotropy (FA), Mean Diffusivity (MD), Axial Diffusivity (AD), and Radial Diffusivity (RD) (Tae *et al.*, 2018). These parameters have been used frequently in the pathologies evaluation for central nervous system tumors, demyelinating and infectious diseases, as well as in vascular system disease (Alves *et al.*, 2012). DWI can provide a reliable detection of ischemia because it can detect subtle changes in water compartmentalization even before the net brain water content increases during the subacute phase of the infarct (Alexander *et al.*, 2001; Assaf and Basser, 2005). Compared with conventional Magnetic Resonance (MR) sequences, DTI provides diagnostic parameters. The Apparent Diffusion Coefficient (ADC), for example, serves as a biomarker in grading of gliomas (Server *et al.*, 2014). Post processing of nerve tracking based on DTI data can also be supportive in surgical planning for brain or spinal cord tumors and provide boundary information as reference for resection in surgery.

In addition to the variety of applications of DTI in the Central Nervous System (CNS) the technique has recently also been applied in the Peripheral Nervous System (PNS). Neuropathies are characterized by microstructural alternations in the nerves and this may lead to decreased anisotropy indices such FA and increased ADC values. The loss of diffusion directionality causes decreased FA, and the loss of myelin and axonal membranes causes increased ADC (Neetu *et al.*, 2016). With aid of such indices, DTI can be used to detect the

complex morphologic and spatial changes of the peripheral nerve anatomy both in trauma and soft tissue tumors, which can be difficult to achieve with conventional MR imaging (Jeon *et al.*, 2018). Recent developments have led to the application of DTI in polyneuropathies of various origins, e.g. in diabetic polyneuropathy (dPNP) (Vaeggemose *et al.*, 2017). There are, however, several challenges mainly arising from the small caliber of peripheral nerves. Due to the smaller dimensions compared to the structures in CNS, higher spatial resolution is needed which in turn leads to a low signal-to-noise ratio. This problem in part can be overcome by increasing the number of diffusion directions, which in turn leads to long acquisition times.

## **1.1 General Description of Diffusion Tensor Imaging (DTI)**

### **1.1.1 Concept of Self-Diffusion and its Development to DTI**

The term ‘diffusion’ is most commonly used for the particles’ random movement from a high concentration region to a low concentration region. However, even in absence of a concentration gradient there is random motion in gasses and fluids. In 1828, the botanist Robert Brown observed the natural phenomena from the random motion of suspended pollen in water which was then named after him (Brown, 1828). According to kinetic theory, when the temperature is over absolute zero (0 kelvin), the particles composing a given fluid will always keep in constant motion and the higher the temperature, the more violent the Brownian motion. For a single particle, due to the Brownian motion, it will experience a random displacement after a certain period of time which will then expand to a group of particles. Because of the lack of knowledge of atom and molecular motion, it was impossible to explain mechanisms behind the Brownian motion. Not until 1905, Albert Einstein proved that Brownian motion was the result of the water molecules’ kinetic movement (Einstein, 1905).

An illustration of the mathematical image of the Brownian motion in space is shown in Figure 1.1.

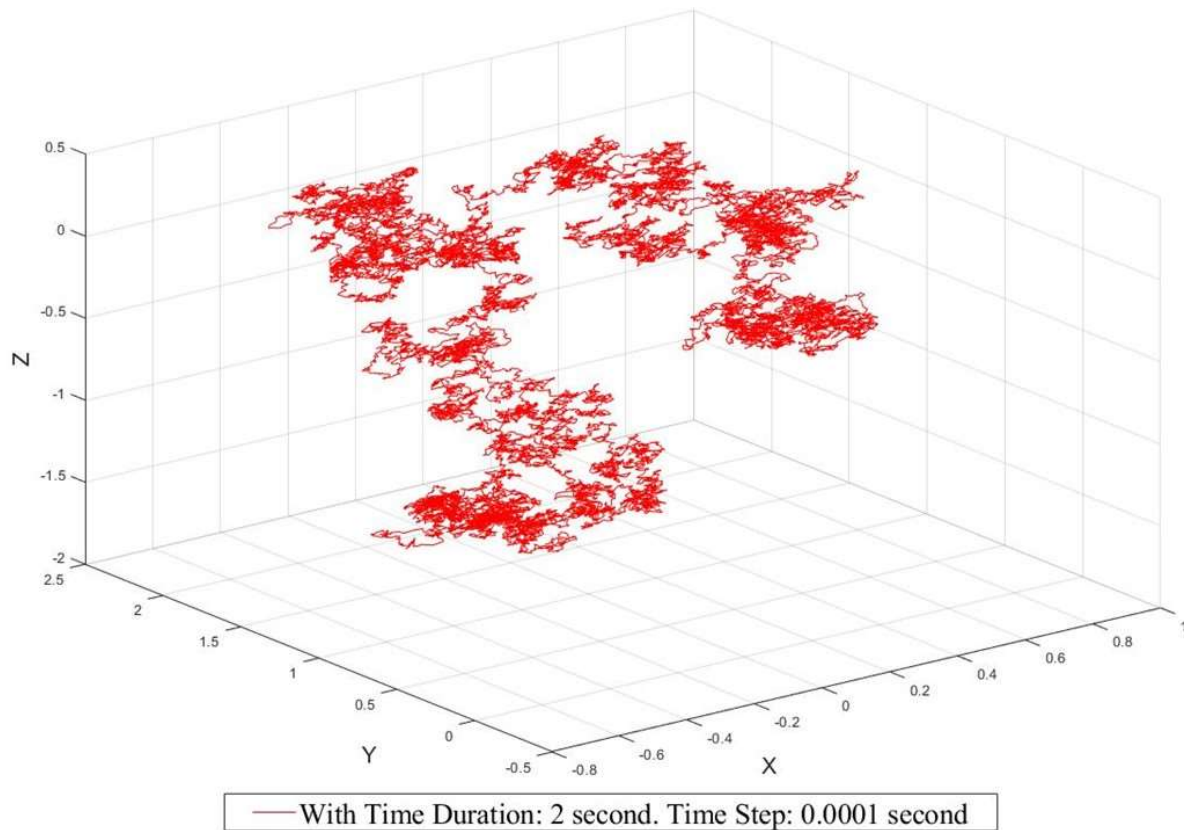


*Figure 1.1: Particle path of a molecule experiencing 3-dimensional Brownian motion (Generate in the MATLAB environment with aid of the build-in function: 'brwnm3').*

The initial development of conventional MR imaging mainly focused on contrast generated through proton density in tissues and the difference of relaxation times. The work of Lauterbur PC, Mansfield P and Ernst R brought clinical MRI application into the field of medicine (Geva, 2006). Initially, the contrasts were based on  $T_1$  (spin-lattice relaxation time) and  $T_2$  (spin-spin relaxation) relaxation properties, but researchers soon began to explore other methods to generate extra contrast between tissues in MR scanning. Taking advantage of the water molecules diffusion in biological tissues, the researchers further explored the method of Diffusion Weighted Imaging. The signal contrast of DWI is based on the differences in Brownian motion. DWI was first developed by Stejskal and Tanner (Stejskal and Tanner, 1965) and applied to human tissue by Le Bihan (Le Bihan, 2014). Based on the work of Stejskal and Tanner in the 1960s, Denis Le Bihan assumed that using specific magnetic gradient pulses can allow for encoding of the diffusion process in real time scanning. But it was challenging to get

satisfying image results by integrating diffusion encoding gradients into the conventional sequences. Firstly, due to additional long period gradient pulses, the acquisition process was very slow and it was very sensitive to motion artifacts due to respiration and other physiological involuntary movements. Not until the invention of the Echo-Planar Imaging (EPI) technique in the early 1990s, DWI found its way into practical application in clinical imaging (Le Bihan, 2014; Turner *et al.*, 1990). The diffusion sequences based on EPI are faster and successfully avoid motion artifacts.

In the standard DWI sequence, diffusion encoding gradients are introduced on either side of the 180° RF (Radio Frequency) refocusing pulse. The diffusion weighting is described by the parameter “b value” which depends on the duration and the strength of the diffusion gradient and on the time between dephasing and rephasing gradients. Diffusion can be measured and evaluated by the so-called apparent diffusion coefficient. Tissues with restricted diffusion are bright on the diffusion-weighted images and are displayed as hypo intense on their ADC map.

Mosley and coworkers observed that the diffusion coefficient of white matter changes depending on the orientation of the diffusion gradient with regard to the fiber direction (Moseley *et al.*, 1990). This effect was explained by Douek, who hypothesized that the Brownian motion of the water molecules was less restricted along the fibers than perpendicular to them, because the myelin sheath acts as a diffusion restriction (Douek *et al.*, 1991). This phenomenon is called anisotropic property. The initial attempts of using an ADC map from diffusion measurements in perpendicular directions to judge anisotropy were not very impressive. The ability to depict fiber bundles in three dimensions (3D) resulted in a new concept: the diffusion tensor. With the use of a tensor formalism by Basser (Basser *et al.*, 1994), modern diffusion tensor imaging became highly interesting to researchers in MR Neuroimaging. Peter Basser originally proposed to use DTI in magnetic resonance imaging in 1994. Initial clinical applications of DTI were naturally limited to the central nervous system due to their high anisotropic property. During that time, susceptibility artefacts and the relative lower image resolution for the smaller diameter of peripheral nerves prevented its application in the peripheral nervous system. Yet, with constant development of sequence and hardware technology in MRI, DTI has also currently extended its application to the peripheral nervous system (Naraghi *et al.*, 2015). Nowadays as a noninvasive magnetic resonance imaging technique, its popularity and significance has become widespread in different MRI application routines such as imaging for brain pathologies, and brain aging research, as well as in neuroscience studies and even cardiac scanning. DTI provides quantitative evaluations about

the degree and direction of water molecule diffusion within the nerves or muscles. Additionally DTI data can also be used for fiber tracking, i.e. to visualize for example the orientation of the axons of a nerve, and further to assess their integrity.

### 1.1.2 Derivation of Diffusion Tensor $\mathbf{D}$ and Anisotropy Indices in MRI

To give out the exact expression of a diffusion coefficient, it is reasonable to start the analysis with a one dimensional case and then expand to the 3D situation. Albert Einstein adopted the Probability Density Function (PDF) as statistic method to solve the diffusion equation for one dimensional Brownian motion. Nowadays, the PDF is a common method to describe the probability associated with a random variable or random vector.

To comprehensively understand the solving process of a diffusion equation, it is necessary to first introduce the well accepted concept of mean square displacement (MSD), which is used to describe the position change of the random movement from a particle over given period of time (Michalet, 2010). In a one-dimensional coordinate system, given the initial position of particle is  $x_0$  over the given period  $t_\Delta$ , the possible location of a random moving particle is position  $x$ , then with repeating observation times  $N_A$ , the MSD is defined as follows:

$$MSD = \langle (x - x_0)^2 \rangle = \frac{1}{N_A} \sum_{i=1}^{N_A} [x_i(t_\Delta) - x_i(0)]^2$$

*Equation 1.1*

The one-dimensional PDF used by Einstein for the stochastic analysis of Brownian motion with continuous variable  $x$  is given as:

$$P(x|x_0, t_\Delta) = \frac{1}{\sqrt{4\pi Dt_\Delta}} e^{-\frac{(x-x_0)^2}{4Dt_\Delta}}$$

*Equation 1.2*

Where  $D$  is the diffusion coefficient.

If a random variable  $x$  follows the Gaussian distribution, then equation 1.2 becomes a Gaussian PDF with a mean value of  $\mu=x_0$  and variance  $\sigma^2=2Dt_\Delta$ , in which  $\sigma$  is normally defined as the standard deviation and  $\mu$  represents the mean of distribution.

$$\text{Gaussian PDF } (x; \mu, \sigma^2) = \frac{1}{\sqrt{2\pi\sigma^2}} e^{-\frac{(x-\mu)^2}{2\sigma^2}}$$

*Equation 1.3*

Obviously equation 1.3 is completely governed by parameters  $\mu$  and  $\sigma^2$ . Instead of  $N_\Delta$  discrete observations (equation 1.1), one can use the continuous variable  $x$  to express the first order moment ( $\mu$ ) and second order moment ( $\sigma^2$ ) of the Gaussian PDF:

$$\begin{aligned} \mu = \langle x \rangle &= \int_{-\infty}^{\infty} x \frac{1}{\sqrt{4\pi Dt_\Delta}} e^{-\frac{(x-x_0)^2}{4Dt_\Delta}} dx = x_0 \\ \sigma^2 = \langle (x - \mu)^2 \rangle &= \int_{-\infty}^{\infty} (x - \mu)^2 \frac{1}{\sqrt{4\pi Dt_\Delta}} e^{-\frac{(x-x_0)^2}{4Dt_\Delta}} dx = \langle (x - x_0)^2 \rangle \end{aligned}$$

*Equation 1.4*

Comparing equation 1.2 and equation 1.3, the relationship between the variance of the Gaussian PDF and the diffusion coefficient is:

$$\sigma^2 = \langle (x - x_0)^2 \rangle = 2Dt_\Delta$$

*Equation 1.5*

In the case of the one dimensional Brownian motion, the mean square displacement is proportional to the diffusion coefficient  $D$  and diffusion time  $t_\Delta$ . By a similar deviation process, the Gaussian distribution of the single variable will be expanded to a multi variable environment with  $x, y, z$  in 3 dimension. In the covariance matrix  $\Sigma$ :

$$\Sigma = \begin{bmatrix} \sigma_x^2 & \sigma_x\sigma_y & \sigma_x\sigma_z \\ \sigma_y\sigma_x & \sigma_y^2 & \sigma_y\sigma_z \\ \sigma_z\sigma_x & \sigma_z\sigma_y & \sigma_z^2 \end{bmatrix}$$

*Equation 1.6*

The diagonal elements indicate the variances along the corresponding dimensions of variables and the off-diagonal elements express the correlations between the variables. Therefore, according to the Einstein-Smoluchowsky equation (Doob, 1942), the three dimensional Gaussian distribution will be:

$$\text{Gaussian PDF } (I; \mu, \Sigma) = \frac{1}{(2\pi)^{3/2} |\Sigma|^{1/2}} e^{(-\frac{1}{2}(I-\mu)^T \Sigma (I-\mu)^{-1})}$$

*Equation 1.7*

Where the symbol  $|\Sigma|$  indicates the determinant of the content.

The Brownian motion of particles in three-dimensions will be interpreted as spatial position  $\vec{r}$ . Its initial position will be  $\vec{r}_0 = (x_0, y_0, z_0)$  and the position after  $t_\Delta$  is  $\vec{r}_{t_\Delta} = (x_{t_\Delta}, y_{t_\Delta}, z_{t_\Delta})$ , then the displacement of particle after time period  $t_\Delta$  can be expressed as following:

$$\vec{r}_\Delta = \vec{r}_{t_\Delta} - \vec{r}_0$$

*Equation 1.8*

And PDF in 3 dimension (Jaffe, 2005) will be derived as:

$$P_{3d}(\vec{r}|\vec{r}_0, t_\Delta) = \frac{1}{\sqrt{4\pi D t_\Delta}} e^{-\frac{\vec{r}_\Delta^2}{4D t_\Delta}} = \frac{1}{\sqrt{4\pi D t_\Delta}} e^{-\frac{(x_\Delta^2 + y_\Delta^2 + z_\Delta^2)}{4D t_\Delta}}$$

*Equation 1.9*



Combined with equation 1.7, diffusion coefficient  $D$  in three-dimensions (which is also called diffusion tensor) will be derived as:

$$D = \Sigma/2 = \frac{1}{2} \begin{bmatrix} \sigma_x^2 & \sigma_x\sigma_y & \sigma_x\sigma_z \\ \sigma_y\sigma_x & \sigma_y^2 & \sigma_y\sigma_z \\ \sigma_z\sigma_x & \sigma_z\sigma_y & \sigma_z^2 \end{bmatrix} = \begin{bmatrix} D_{xx} & D_{xy} & D_{xz} \\ D_{xy} & D_{yy} & D_{yz} \\ D_{xz} & D_{yz} & D_{zz} \end{bmatrix}$$

*Equation 1.10*

Which means  $D$  is proportional to  $\Sigma$  and the diffusion tensor elements  $D_{ij} \sim \Sigma_{ij}$  ( $i, j=1,2,3$ ).

The covariance matrix  $D$  is positive definite and symmetric.

When analyzing a phantom filled with a homogeneous substance, for example agarose or fluids such as water, the diffusing performances of particles are same in all directions. Thus, such substances are called isotropic media and are characterized by a diffusion coefficient ( $D$ ) with identical diagonal elements and all off-diagonal elements being zero (Gullmar *et al.*, 2002). That also means the eigenvalues are equal and independent in each eigenvector direction in isotropic materials.

$$D_{isotropic} = \begin{bmatrix} D & 0 & 0 \\ 0 & D & 0 \\ 0 & 0 & D \end{bmatrix}$$

*Equation 1.11*

MRI uses the signal of the hydrogen nucleus of a water molecule. In biological tissues like nerves, which are highly and anisotropically structured due to cell wall and nerve sheath, the diffusion coefficients vary along different directions. In other words, all biological tissues demonstrate a certain degree of anisotropy. This is most obvious in nerve and muscle tissues: here, the cell membrane or myelin sheath is tightly structured and coherently aligned along the axons, allowing for the water molecules' diffusion in the direction perpendicular to the fibrillary structure (radial diffusion). Radial diffusion is much slower than axial diffusion along the axis direction. The phenomenon is more prominent for white matter because of its dense parallel arranged fiber bundles compared to other antistrophic tissues such as muscle and tendons even though they also demonstrate significant anisotropic property.

For quantitative analysis and evaluation of anisotropy in biological tissues, the diffusion tensor given in equation 1.10 is used to describe the water molecule's diffusion phenomenon. The three diagonal elements ( $D_{xx}$ ,  $D_{yy}$ ,  $D_{zz}$ ) of the tensor  $D$  represent diffusion coefficients measured in the laboratory coordinate correspondingly along the three principal axis (X-, Y- and Z-). Other six off-diagonal terms ( $D_{xy}$ ,  $D_{yx}$ ,  $D_{xz}$ ,  $D_{zx}$ ,  $D_{yz}$ ,  $D_{zy}$ ) reflect the correlation between each pair of principal axis as marked by the footnote.

In diffusion MR imaging, the diffusion tensor cannot be directly obtained from practical measurements, but its individual elements can be estimated through the comparison between images with and without diffusion weight. The proton's phase dispersion after a diffusion gradient pulse can cause the signal loss which will indicate the extent of diffusion in various directions. With these methods, however, the measured signal loss is not coming only from diffusion, there are several processes responsible, for example: blood and lymphatic flow, involuntary motions caused by cardiac pulsations or respiration. All of these processes could contribute to the final signal loss, and furthermore the inevitable phase dispersion due to susceptibility (caused by both the magnetic field and the tissues' inner microenvironment) which will impede the accuracy of the calculation of tensor elements. Signal loss and the estimations of tensor elements based on that also vary according to different types of pulse sequences and applied detail parameters during acquisition.

Because of these limitations, the term 'apparent diffusion coefficient' is adopted to refer to estimated diffusion extents in DTI research work. 'Apparent' is used because it is not a direct measure of the "intrinsic" diffusion, but rather the parameter which indirectly reflects the interactions between the water molecules' diffusion process and the micro-structures of studied object in voxel size level.

To accomplish this, the well accepted Stejskal-Tanner imaging sequence (Stejskal and Tanner, 1965) is typically used. The Stejskal-Tanner sequence uses two relative strong gradient pulses (compared to normal imaging gradient pulses for encoding), their amplitudes, time duration and interval can be used for controlling diffusion weighting. The diffusion gradient pulses are symmetrically positioned on both sides of the  $180^\circ$  RF refocusing pulse, (figure 1.2).

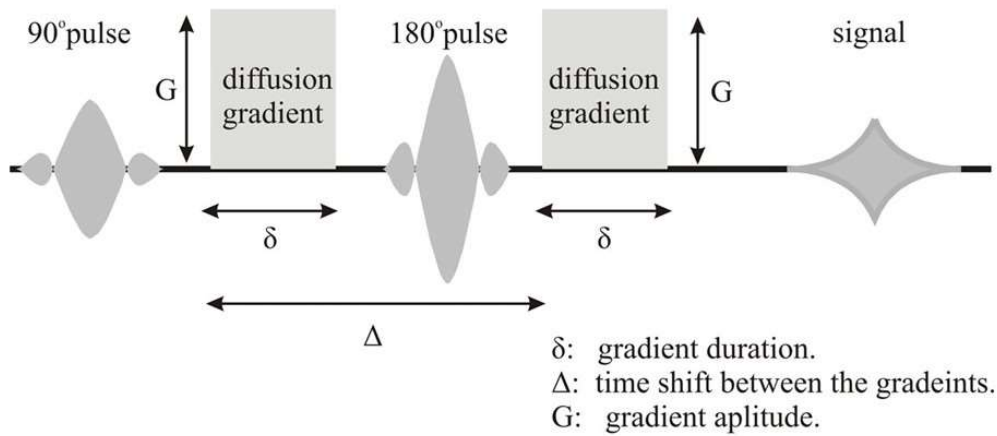


Figure 1.2: Diagram example of the Stejskal-Tanner diffusion gradients applied in spin echo sequence (Stejskal and Tanner, 1965).

The first diffusion gradient is applied between the  $90^\circ$  excitation RF pulse and the  $180^\circ$  refocusing RF pulse and induces a de-phase processing for all targeted spins. The second diffusion gradient pulse is applied symmetrically after the  $180^\circ$  refocusing RF pulse with identical amplitude and pulse duration. Due to the reversal effect of the  $180^\circ$  refocusing RF pulse, in principle, the previous phase shift of the targeted spins will be cancelled by the reversal phase changing from the second diffusion gradient pulse. In fact, as figure 1.3 shows, this only happens on static spins which experience de-phase and re-phase operations at same location. But for those spins that have diffused in one or multi directions during the time interval of diffusion gradients:  $\Delta$ , their final phase status will be disordered due to the location change from Brownian. Therefore, the sum of magnetic moments in such a voxel with those diffused spins will be lower than the voxel with static spins. The introduced signal loss can be used for comparison with signal intensity without diffusion weight to derivate ADC map.

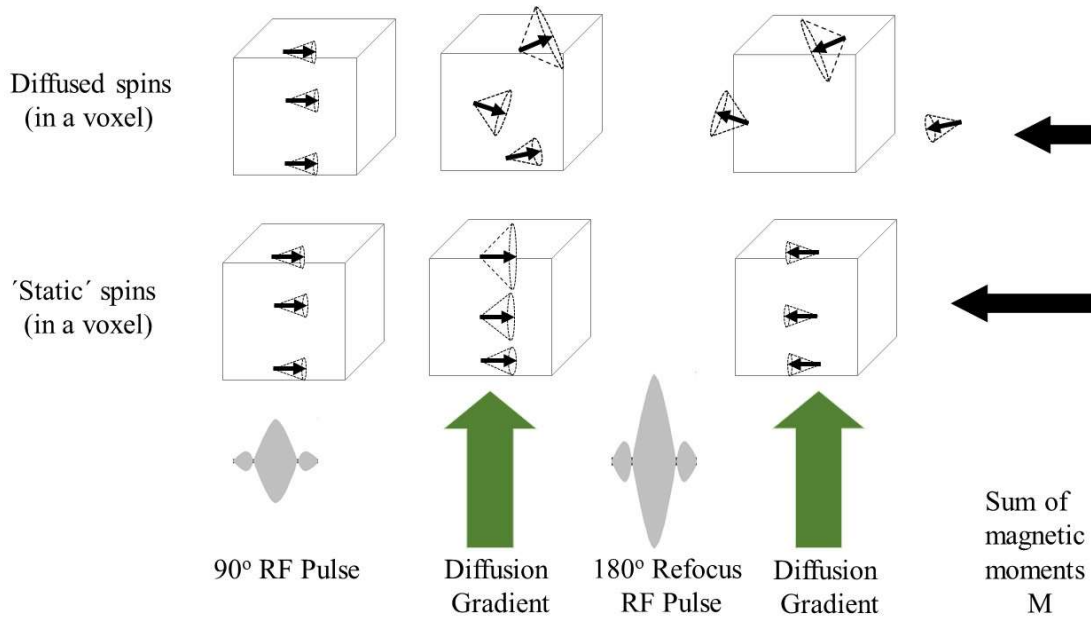


Figure 1.3: The comparison of phase changes between 'static' spins and diffused spins after diffusion gradients application (the gradient direction as arrows shown). The sum of magnetic moments  $M$  from diffused spins in a certain voxel will be weaker than the sum of magnetic moments from 'static' spins with the same size of voxel because of the diffusion process.

The signal loss due to the diffusion process can be expressed with aid of signal intensity which is denoted as  $S_0$  without diffusion weight (Le Bihan *et al.*, 1986).

$$S_k = S_0 * e^{-(bD)} = \rho * e^{-(TE/T_2)} * e^{-(\gamma^2 G^2 \delta^2 (\Delta - \delta/3) D)}$$

Equation 1.12

Where  $S_k$  is the signal intensity with a certain diffusion gradient weight produced by  $g_k$ ;  $S_0$  is the signal intensity without diffusion weight;  $\rho$  is the proton density function of the measured object;  $TE$  is the echo time;  $T_2$  is the spin-spin relaxation time;  $\gamma$  is the gyromagnetic ratio (42 MHz/Tesla for water proton spin); as shown in figure 1.2,  $G$  is the amplitude of diffusion gradient pulses;  $\delta$  is the diffusion gradient pulse duration ;  $\Delta$  is the time interval of the diffusion gradients ; and  $D$  is the diffusion coefficient.

Equation 1.12 shows that within the same voxel, the diffusion signal attenuation compared with  $S_0$  is determined by the parameters of gradient amplitude, diffusion pulse duration, the time interval between the two diffusion gradients and the local diffusion coefficient. Here, in order

to separate the tissue's intrinsic factor and external factor, the combined parameter called b-value is introduced as the expression:

$$b = \gamma^2 \delta^2 (\Delta - \delta/3) |G|^2$$

*Equation 1.13*

Generally with known values of the parameters  $\gamma$ ,  $\delta$ , and  $\Delta$ , one measurement without diffusion weighting  $S_0$  and at least six measurements with diffusion weighting  $S_k$  using different non-collinear diffusion gradients are typically required to estimate the symmetric  $3 \times 3$  diffusion tensor  $D$ . By inserting normalized gradient vectors:  $\hat{g} = \frac{g}{|g|}$  and with help of logarithm operation on both sides, equation 1.12 can be transferred to:

$$\ln \frac{S_0}{S_k} = \frac{1}{\ln e^{-\gamma^2 \delta^2 \Delta \hat{g}_k^T D \hat{g}_k}} = \ln(S_0) - \ln(S_k) = b \hat{g}_k^T D \hat{g}_k;$$

*Equation 1.14*

Making reference of the interpretation method from Ketil Oppedal (Oppedal, 2005), the practical scanning with the six directions scheme of multi-directional diffusion weighting (MDDW) from vendor was performed on an anonymous volunteer. The images of sciatic nerve are used as representation of signal intensities in figure 1.4:

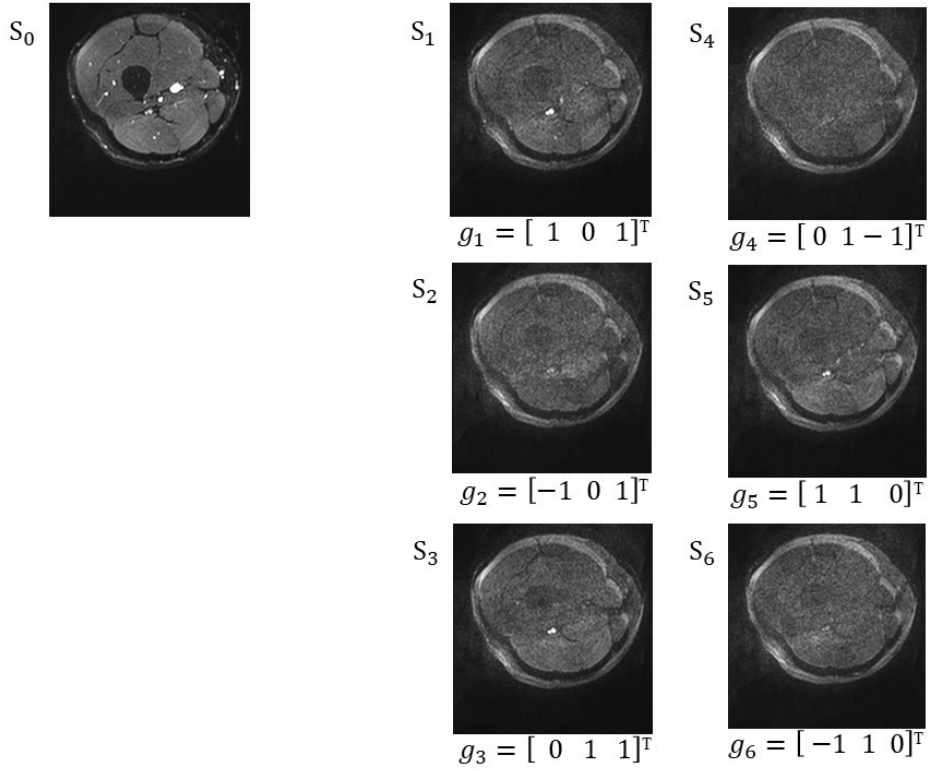


Figure 1.4: Diffusion measurements example,  $S_0$ : signal intensity of an image without diffusion weight;  $S_k$ : ( $i = 1 \dots 6$ ) signal intensity of an image with diffusion weight;  $g_k$ : ( $i = 1 \dots 6$ ): diffusion gradient vectors from SIEMENS multi-directional diffusion weighting with six directions.

Combining measurement data  $S_0$ ,  $S_k$  and the known parameters  $b$ ,  $\hat{g}_k$ , the diffusion tensor elements  $D_{ij}$  ( $i,j=1,2,3$ ) can be resolved through following linear equation system:

$$\begin{aligned}
 \ln(S_0) - \ln(S_1) &= b \hat{g}_1^T D \hat{g}_1; \\
 \ln(S_0) - \ln(S_2) &= b \hat{g}_2^T D \hat{g}_2; \\
 \ln(S_0) - \ln(S_3) &= b \hat{g}_3^T D \hat{g}_3; \\
 \ln(S_0) - \ln(S_4) &= b \hat{g}_4^T D \hat{g}_4; \\
 \ln(S_0) - \ln(S_5) &= b \hat{g}_5^T D \hat{g}_5; \\
 \ln(S_0) - \ln(S_6) &= b \hat{g}_6^T D \hat{g}_6;
 \end{aligned}$$

Equation 1.15

For more than six diffusion gradient directions:  $g_1 \dots g_k \dots g_K$  as  $K > 6$ , the Least-Squares (LS) estimation method for obtaining the diffusion tensor  $D$  is the obvious choice. Assigning the diffusion weighted measurements results still as  $S_k$  for  $k = 1 \dots K$ ;  $K \geq 6$ , equation 1.15 can be expressed as:

$$\frac{\ln(S_0) - \ln(S_k)}{b} = \hat{g}_k^T D \hat{g}_k = \sum_{i=1}^3 \sum_{j=1}^3 g_k^i D_{ij} g_k^j = Y_k^T \Lambda; \quad k = 1 \dots K$$

Equation 1.16

When  $\frac{\ln(S_0) - \ln(S_k)}{b}$  is denoted by vector  $Y_k$ ; the matrix of diffusion gradients  $\sum_{i=1}^3 \sum_{j=1}^3 g_k^i g_k^j$  is represented by  $Y_k^T$  with a size of  $9 \times K$  and the vector which is composed by diffusion tensor elements is denoted as  $\Lambda = (D_{11} \dots D_{33})^T$ . Then the square sum  $Q$  with respect to  $\Lambda$  will be:

$$Q = \sum_{k=1}^K (Y_k - Y_k^T \Lambda)^2 = (Y - Y \Lambda)^T (Y - Y \Lambda) = Y^T Y - 2 \Lambda^T Y^T Y + \Lambda^T Y^T Y \Lambda$$

Equation 1.17

Minimizing  $Q$  with respect to  $\Lambda$  by differentiating  $Q$  with respect to  $\Lambda$ .

$$\frac{dQ}{d\Lambda} = 0$$

Equation 1.18

With known diffusion gradient scheme information of  $Y$  and measurement data  $Y$ , the solution of equation 1.18 will be:

$$\hat{\Lambda} = (Y^T Y)^{-1} Y^T Y$$

Equation 1.19

In order to estimate the FA values in the simulation section of this study, the above operations for resolving diffusion tensor  $D$  have been implemented in the MATLAB program with the corresponding build-in functions

Furthermore, in order to describe the intrinsic diffusion properties of a scanned object independent from the coordinate system of the scanner, the concept of eigenvectors and eigenvalues which are derived from the tensor was introduced (Pierpaoli *et al.*, 1996). In 3D, 3 eigenvalues with respective notations  $\lambda_1$ ,  $\lambda_2$  and  $\lambda_3$  are defined in conjunction with 3 orthogonal eigenvectors  $\vec{\varepsilon}_1, \vec{\varepsilon}_2, \vec{\varepsilon}_3$  (which are perpendicular to each other within the studied fiber frame) as shown in figure 1.5.

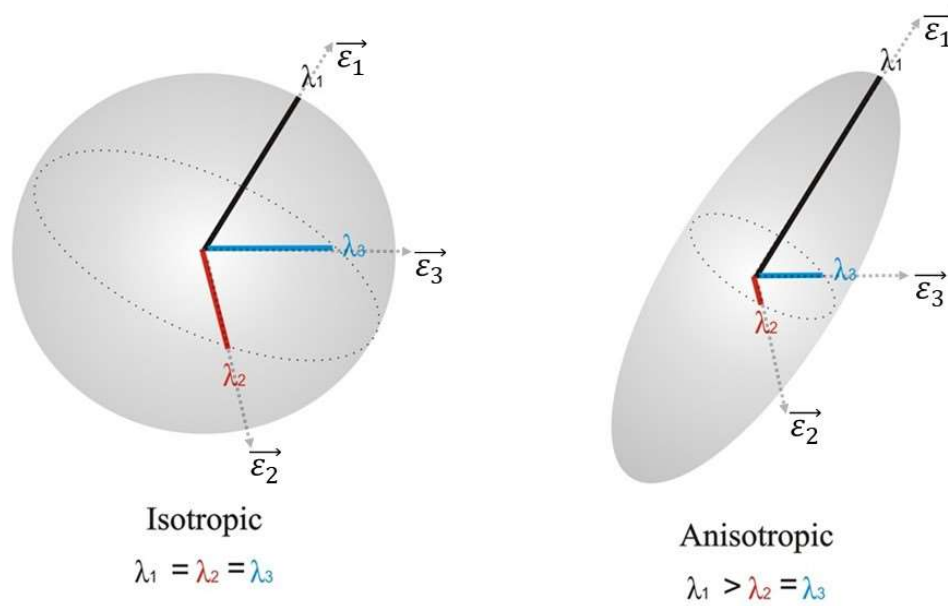


Figure 1.5: Eigenvalues  $\lambda_1$ ,  $\lambda_2$  and  $\lambda_3$  along corresponding eigenvectors  $\vec{\varepsilon}_1, \vec{\varepsilon}_2, \vec{\varepsilon}_3$  in Isotropic and Anisotropic situations.

Unlike tensor notation  $D$ , a matrix whose diagonal elements are composed by three eigenvalues and off-diagonal elements equal to zero could be considered another tensor denoted by  $D'$ . Since  $D$  is symmetric and positive definite, the relationship between  $D$  and  $D'$  will be expressed by diagonalization of  $D$  with matrix  $E$ :



$$D = ED'E^T$$

*Equation 1.20*

Here E is the transformed matrix which could be composed by vectors  $[\vec{\varepsilon}_1 \vec{\varepsilon}_2 \vec{\varepsilon}_3]$ , and correspondingly  $D'$  as the transforming result will be:

$$D' = E^T D E = \begin{bmatrix} \lambda_1 & 0 & 0 \\ 0 & \lambda_2 & 0 \\ 0 & 0 & \lambda_3 \end{bmatrix}$$

*Equation 1.21*

The orthogonal vectors  $\vec{\varepsilon}_1 \vec{\varepsilon}_2 \vec{\varepsilon}_3$  (figure 1.5) are the three eigenvectors from tensor D, they indicate three uncorrelated directions within the fiber frame along which the water molecule diffused. In the coordinate system of the eigenvectors  $\vec{\varepsilon}_1 \vec{\varepsilon}_2 \vec{\varepsilon}_3$ , the largest eigenvalue is  $\lambda_1$  along  $\vec{\varepsilon}_1$ , reflecting the highest diffusivity (that is normally along the fiber orientation) and the smallest eigenvalue is  $\lambda_3$  corresponding to  $\vec{\varepsilon}_3$ , indicating the smallest diffusivity (that is usually perpendicular to fiber orientation) (Basser *et al.*, 1994).

Based on the eigenvalues, several further useful indices can be calculated and they are also independent from the coordinate system of the diffusion gradients: Fractional Anisotropy, Mean Diffusivity, Axial Diffusivity and Radial Diffusivity.

Axial Diffusivity =  $\lambda_1$ ;

*Equation 1.22*

Radial Diffusivity =  $(\lambda_2 + \lambda_3)/2$ ;

*Equation 1.23*

Mean Diffusivity =  $(\lambda_1 + \lambda_2 + \lambda_3)/3$ ;

*Equation 1.24*

$$\text{Fractional Anisotropy} = \sqrt{\frac{3}{2} \frac{\sum_{i=1,2,3} (\lambda_i - \bar{\lambda})^2}{\sum_{i=1,2,3} \lambda_i^2}};$$

*Equation 1.25*

### 1.1.3 DTI in Peripheral Nerves

With more meaningful parameters, diffusion tensor imaging has become widely used to assess and visualize the white matter tracts in the central nervous system. Because of the diffusion sequence's inherent susceptibility to motion, magnetic field inhomogeneity, and strong T2-weighting (Jeon *et al.*, 2018), the application of DTI in peripheral nerves became feasible only after several significant developments in MR hardware such as high performance gradient coil systems, better magnet homogeneity, and multi-channel coils enabling parallel imaging techniques to shorten acquisition time, occurred (Chianca *et al.*, 2017; Naraghi *et al.*, 2015; Schmid *et al.*, 2018).

Although anisotropic indices such like ADC and FA are quantitative parameters, they still depend on the scanning environment for example the magnetic field strength, type of coil, type of sequence and corresponding adopted b-value range. Previous studies showed that the normal FA of peripheral nerves ranges between 0.3 and 0.7 (Chhabra *et al.*, 2013) and by means of their FA, peripheral nerves can be clearly distinguished from the surrounding tissues. However, there are also limitations to assessing the intrinsic properties of the PNS, since the FA values of peripheral nerves are strongly correlated with axon density and axon diameter, rather than myelin-related parameters (Khalil *et al.*, 2010). This is based on the theory that anisotropy is decisively influenced by the membranes of an axon and only slightly by the myelin sheaths (Takagi *et al.*, 2009).

To assess peripheral nerves in clinical practice, establishing normative DTI indices is crucial for reliably detecting pathology, particularly in milder forms of peripheral neuropathy that may only result in subtle changes in DTI indices. However, so far multiple studies have only demonstrated a rather wide range in DTI values of the upper extremity peripheral nerves in healthy volunteers (Jeon *et al.*, 2018). The results of these studies examining DTI metrics also vary widely from study to study due to factors such as hardware differences from vendors or the type of diffusion sequences and their specified parameters. Additionally, the DTI indices

such as FA and ADC showed significant variation along the nerve: FAs shows a proximodistal increase, whereas ADC shows a proximodistal decrease (Paniandi *et al.*, 2018; Stein *et al.*, 2009). There are differences in FA and mean diffusivity between different nerves, which in part may be explained by an insufficient spatial resolution or low Signal-to-Noise Ratio (SNR) (Naraghi *et al.*, 2015). Due to the small caliber of the nerves, DTI in peripheral nerve requires high in-plane spatial resolution. However, there is a trade-off between spatial resolution, SNR and acquisition time. There are several approaches to overcome the limitations of DTI in the PNS including advanced RF coils that are optimized for the extremities, optimized pulse sequences and dedicated post processing software. Although facing various challenges, DTI has meanwhile gained importance in DTI of the PNS. DTI provides additional and complementary information compared to conventional MR Neurography. The parameters "axial diffusivity" and "radial diffusivity", which one can derive from the diffusion tensor, are markers of axon integrity and myelin sheath integrity, respectively. "Axial diffusivity" characterizes the water movement parallel to the axonal tracts. Changes in intracellular water due to impaired axonal transport leads to reduced axial diffusivity which can be used to characterize axonal damage in the acute phase (Aung *et al.*, 2013). Demyelination (or myelin pathology) is associated with an increase in "radial diffusivity" which characterizes the water movement perpendicular to the axonal tracts. (Budde *et al.*, 2008). Compared to conventional structural MRI, the ability of distinguishing pathologic changes in axons and myelin by DTI can offer the information for potential pathologies well before the apparent structural changes or functional symptoms appear (Aung *et al.*, 2013). This is particularly relevant for the diagnosis and treatment in the early stages of a disease.

## 1.2 DTI Limitations on PNS

Although a quantitative noninvasive imaging method, DTI has provided insight into the microstructure of the brain and its usage in fiber tracking also presented the anatomical connectivity of white matter, its applications in the PNS still faces a certain number of challenges because of nerve size, long acquisition time, artifacts and the lack of standardized post processing. On the other hand, there are also certain advantages of the PNS when performing DTI, e.g. the well-known and uniform direction of the nerves within the extremities.

In this thesis two ways are investigated to increase SNR: Using a diffusion gradient scheme adapted to the characteristics of the PNS, and post-hoc correction for low SNR.

### 1.2.1 Selection of Gradient Vectors Scheme

For DTI, a minimum of six non collinear gradients are required. The higher the number of gradients, the better the accuracy of the parameters calculated from DTI. There is, however, a trade-off between accuracy and acquisition time. DTI is most often performed by spreading the gradient directions in space evenly (uniform coverage) (Jones *et al.*, 1999). Several studies have investigated the influence of the number of gradient directions on the accuracy of FA and mean diffusivity (Lagana *et al.*, 2010; Landman *et al.*, 2007). As shown by these studies, at least 20 diffusion gradient directions are necessary to guarantee reliable estimation of FA, while at least 30 directions are needed for robust calculation of the tensor orientation and mean diffusivity (Jones, 2004).

In the peripheral nerve system, however, the anatomical complexity is much lower than in the brain: With only a few exceptions (brachial and lumbar plexus) there is no fiber crossing and much less fiber branching than in the brain. Therefore, a smaller number of gradients is likely to be sufficient for DTI of the PNS. Zhou *et al.* compared the reliability of DTI in the median nerve for 7, 21, and 42 diffusion gradient directions and found that there was a significant underestimation of FA when using only 7 directions (Zhou *et al.*, 2014). This suggests, that also in the PNS it is not sufficient to use the lowest number of diffusion gradients that is theoretically possible.

In all diffusion tensor acquisition schemes mentioned by previous studies, Jones' optimal schemes (Jones *et al.*, 1999) and the schemes developed by Downhill Simplex Minimization (DSM) are considered optimal in terms of lowering noise and bias (Skare *et al.*, 2000a). A parameter characterizing the noise performance of a DTI acquisition scheme is the condition number (CN) (Skare *et al.*, 2000a). Referring to equation 2.12, the matrix  $C$  with size of  $6 \times N$  ( $N$  is the number of gradient directions), also referred to as transformation matrix between tensor and measurement data, is measurement data, only depends on the orientation of the diffusion-weighting gradients (or diffusion gradient scheme). The condition number of the

transformation matrix defines the lower and upper bounds of the error propagation from the practical measurements data to the estimated diffusion tensor. Due to CN's objectiveness and quantitative property, the numerical algorithms based on the minimization of the condition number can naturally be used for searching new DTI schemes (Skare *et al.*, 2000a).

### 1.2.2 Noise Impact on Anisotropy Indices

As both the diffusion gradients and a relatively long TE lead to signal attenuation in DTI, noise and its correction become an important topic in DTI, particularly if high spatial resolution is needed. Several authors have studied the effect of low SNR on the parameters derived from DTI (Farrell *et al.*, 2007; Landman *et al.*, 2008; Polzehl and Tabelow, 2016). Depending on the selection of the b-value, the noise in the DW images will propagate through a least-squares model into variances in the diffusion tensor elements, and then such variances in diffusion tensor elements further propagate to the errors in anisotropy indices, such as FA (Poonawalla and Zhou, 2004).

Due to the low SNR in vivo diffusion weighted images, the simple operation of magnitude averaging against phase instabilities induced by the diffusion sensitizing gradients are commonly used for stable calculation of the diffusion tensor. However, averaged magnitude images reduce the uncertainty but have no effect on the bias of the diffusion signal, the so-called noise floor (Gudbjartsson and Patz, 1995; Henkelman, 1985). This becomes increasingly prominent at high resolutions, high b values or pathological high ADCs. In these cases, the acquired signal probably already is lower than the floor of background noise, since it decays rapidly with high diffusion gradients, especially when the gradient pulse is applied parallel or along principal diffusion direction of the studied object (Laun *et al.*, 2009). Jones *et al.* have shown that this results in a significant underestimation of FA and ADC (Jones and Basser, 2004).

Besides sequence optimization and hardware improvement, the post-hoc noise correction is an important method to lower the impact of noise on the parameters calculated from DTI.

Previously introduced noise correction ideas such as 'power images' correction (Miller and Joseph, 1993) and Rician distribution correction (Gudbjartsson and Patz, 1995) mainly focused

on conventional magnitude MR imaging and are still in a theoretical analysis phase or not yet considered in diffusion application.

### 1.2.2.1 Noise Correction Method: Power Image

The abovementioned usage of power images for correcting noised MRI data was introduced by Miller and Joseph (Miller and Joseph, 1993). Their proposal was based on the zero mean of Gaussian noise induced from each quadrature detection channel (imaginary and real) during signal acquisition. The mean of powered measurement signal:  $M$  can be expressed by the addition of the powered true signal:  $A$  and two times of the powered noise standard deviation:  $\sigma$  which can be acquired by the average value of Region of Interest (ROI) over any region that is known to have no object signal, e.g. the corners of an image. The true signal can be estimated by the square root of the subtraction between  $\langle M^2 \rangle$  and  $\sigma^2$ . Without further simulation and practical investigation, Miller and Joseph also mentioned the potential of this method in the application of diffusion coefficients.

### 1.2.2.2 Noise Correction Method: Rician distribution correction

Ultimately, Gudbjartsson and Patz presented an approximation method with two different factors for noise correction (Gudbjartsson and Patz, 1995) based on Raleigh noise distribution which lead to the Rician distribution of an magnitude signal. The target of this approximation method is the true power of noise standard deviation:  $\sigma^2$  which can be estimated according to the probability distribution equation of Rayleigh either from the approximated mean of measured noise by an approximate factor  $\sqrt{\frac{2}{\pi}}$  or the approximated standard deviation of measured noise by an approximate factor  $\sqrt{\frac{2}{4-\pi}}$ . They postulated the square root of the absolute subtracted result between:  $\bar{M}^2$  (power of the mean measured signal) and  $\sigma^2$  being close to the true signal:  $A$ . However, the mathematical model had not been verified in DTI application yet. Fairly recent research in noise correction from Dietrich O (Dietrich *et al.*, 2001) provided an analysis of two situations: Gaussian noise and Non-Gaussian noise. The correction of the Gaussian noise case was very similar to the approximation method as described by

Gudbjartsson and Patz (Miller and Joseph, 1993). For the arbitrary non-Gaussian noise, the correction has to be assessed in relation to the true signal and measured noise. In identifying this relation, both, the iteration process and water phantom reference imaging from Dietrich O seemed quite time consuming with respect to practical application, especially regarding the relative long acquisition time in diffusion measurements. Additionally, the noise pattern changed according to complicated factors from both, scanner hardware and physiological status of the scanned object, thus the repeating reference imaging obviously increased the acquisition burden. Therefore, the arbitrary noise correction will not be focused in this project.

### **1.3 Aim of the Project**

The aim of this project is to increase the accuracy and reliability of DTI in PNS by reducing the noise bias. This project will follow two approaches in order to achieve this goal:

- (1) Choice of the diffusion gradient scheme: As shown above, high angular resolved diffusion imaging is a powerful approach to reduce the bias of noise. On the other hand, this approach leads to long acquisition times which in turn increases the susceptibility of DTI to motion artifacts. Therefore, a gradient scheme that takes into account the orientation and geometry of the peripheral nerve system is proposed.
- (2) Post-hoc noise correction does not require additional acquisition time. Therefore, focusing on the effect of different noise correction schemes on the reliability of the parameters calculated from DTI, two correction schemes (power image method and approximation method) will be compared in a simulation study and in measurements in a dedicated PNS phantom.

## 2 MATERIAL UND METHOD

In this chapter, the development of a non-uniform gradient scheme is described. The performance of the developed gradient schemes with a relatively dense distribution around the main direction of the nerve was tested using the Mont Carlo simulation method and was verified in a phantom study as well. Finally the scheme was compared to established, uniform gradient schemes.

In the second part of this chapter, two established noise correction methods are applied for DTI of the PNS. The efficacy of these methods was examined by Monte-Carlo simulation and in a phantom study.

### 2.1 Tailored Diffusion Gradient Scheme for Peripheral Nerves

#### 2.1.1 General Requirements for Gradient Vector Numbers

The number of diffusion gradient directions ( $N$ ) used in the diffusion gradient scheme plays an important role during DTI data acquisition. The influence of  $N$  on anisotropy evaluation has been discussed in several studies and corresponding diffusion gradient schemes have been published and evaluated in the literature (Jones *et al.*, 1999; Papadakis *et al.*, 1999; Skare *et al.*, 2000a). Increasing  $N$  typically improves the precision of DTI tensor elements calculation and the estimation of FA, ADC, RD, or AD and produces more accurate data for fiber tracking and better quality of anisotropy maps (Bernstein *et al.*, 2004). However, when maintaining the same acquisition time, the gain in image quality becomes progressively less when the number of directions exceeds around 25 by trading off the acquisition time (Bernstein *et al.*, 2004; Poonawalla and Zhou, 2004).

To estimate the diffusion tensor, acquisitions must be performed for at least six non collinear spatial orientations of diffusion gradients (Basser *et al.*, 1994). The more uniformly the diffusion directions are distributed in space, the more accurate the estimation in each voxel is (Jones *et al.*, 1999). Furthermore, increasing the number of orientations considerably improves the SNR in the ADC measurement, which is also defined by Xing as the diffusion-to-noise ratio (Xing *et al.*, 1997) and consequently the information about the microscopic tissue



structure is more accurate (Papadakis *et al.*, 1999). Increasing the number of orientations, however, directly leads to an increase in acquisition time.

There is a set of rules that need to be satisfied in designing the gradient vectors scheme. These rules guarantee that the linear equations are nonsingular for the estimation of the diffusion tensor and they require to select at least six valid diffusion gradients and further non collinear gradient directions will help the accuracy of estimation. (Ozcan, 2005).

1. Fundamentally, no any pair of two gradient vectors should point to the same direction.
2. In case of a triplet of vectors belonging to a two dimensional subspace that conform to rule (1), the remaining triplet must be linearly independent.
3. Additionally, no four gradient vectors should belong to the same two dimensional subspace.

## **2.1.2 Tailored Gradient Vector Scheme for Peripheral Nerves**

Satisfying the basic rules for producing non-collinear vectors, and aiming at time efficient scanning, a specified diffusion gradient scheme, the Directional Gradient Vector scheme (DGV), will be introduced. With the prior known range of PNS orientation, this non-uniform gradient scheme has a concentrated distribution around the studied tensor.

### **2.1.2.1 Preparing DGV scheme**

The peripheral nerves exhibit a preferred direction which corresponds approximately with the z-axis of the MR scanner. Therefore, the question arises whether one can exploit the knowledge about the preferred direction and the cylindrical structure of the nerve to simplify the gradient scheme and reduce the number of diffusion gradients. Figure 2.1 shows the different distribution pattern between a conventional scheme and the DGV scheme.

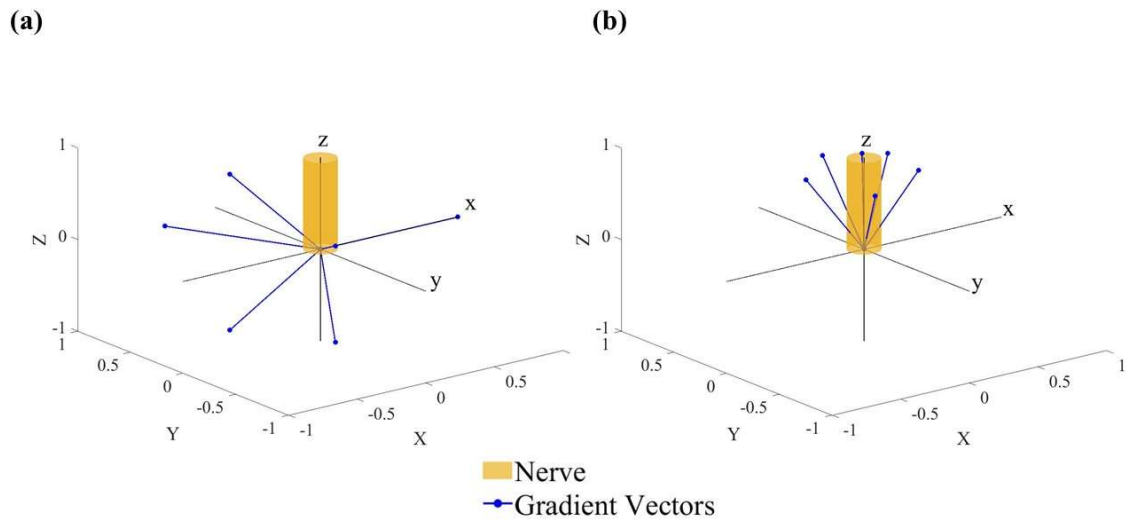
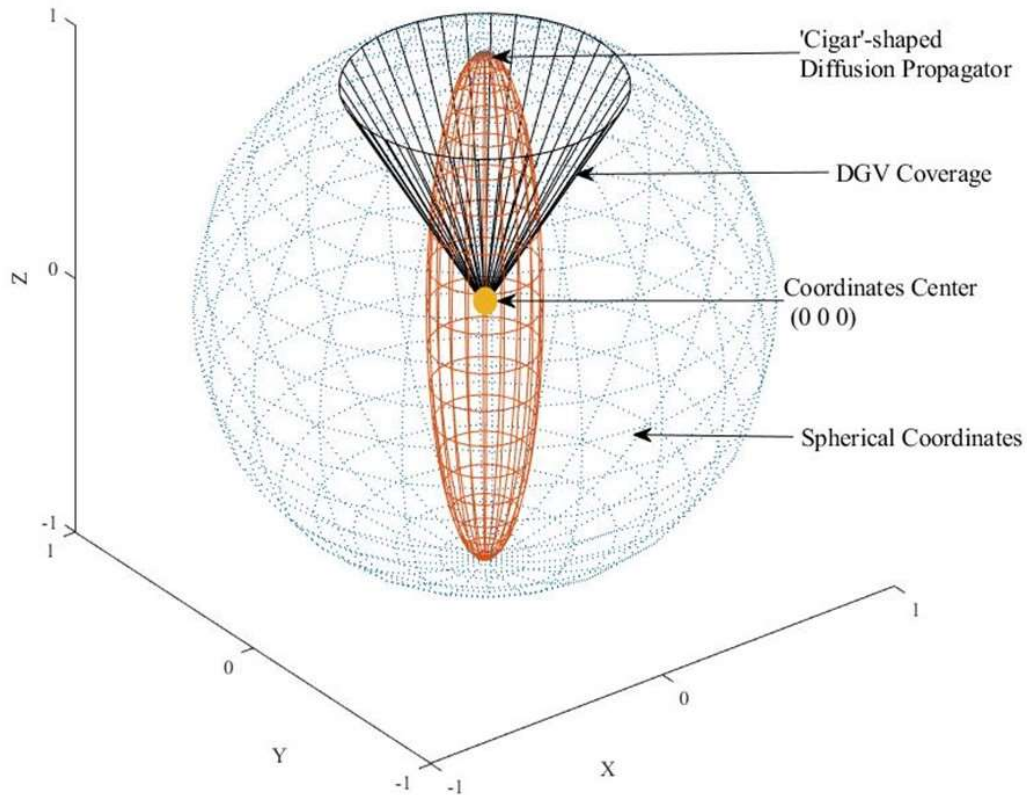


Figure 2.1: Comparison between conventional scheme and DGV scheme. (a) conventional uniformly distributed gradient vectors scheme (blue vectors) around nerve (yellow). (b) non-uniform distributed directional gradient vectors scheme (blue vectors) around nerve (yellow).

To determine the relationship between DTI parameters in the peripheral nerve and the DGV scheme used for DTI, a model is needed that distributes the diffusion directions with prior knowledge of the diffusion propagator (figure 2.2). The diffusion propagator indicates the probability that a water molecule experiences a net displacement in a certain direction.



*Figure 2.2: Diffusion propagator of the nerve tissue (Orientation: Z-direction) and DGV scheme in spherical coordinates (dotted lines). The sphere confines the tip of the gradient vector. The arrows forming a cone indicate the diffusion vectors which should result in the same diffusivity due to the cylindrical shape of the nerve.*

Firstly assuming a ‘cigar’ shaped diffusion propagator to represent directional diffusion in nerve tissue. Secondly, it can be seen in the cross section view of the combined model (figure 2.3), the vectors of the tailored DGV scheme will be inside the cone defined by the angle:  $\Theta_{\max}$ .

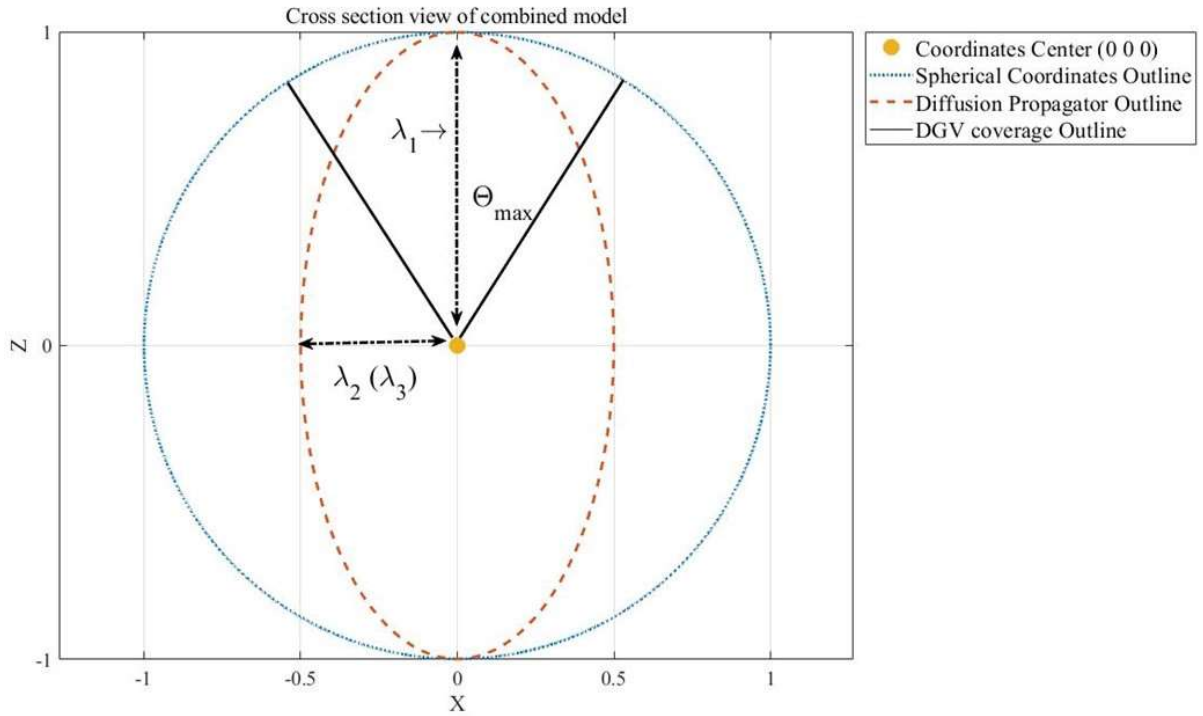


Figure 2.3: Cross section displaying the diffusion propagator (With eigenvalues  $\lambda_1$  and  $\lambda_2=\lambda_3$ ) of the nerve and the cone (defined by  $\Theta_{\max}$ ), in which the diffusion directions are confined.

The eigenvalues are  $\lambda_1$ ,  $\lambda_2$  and  $\lambda_3$ , it is due to the axial symmetry of the ellipsoid,  $\lambda_2$  equals  $\lambda_3$ . The normalized gradient direction vector  $g_k$  is defined by:

$$g_k = (g_{xk} \ g_{yk} \ g_{zk})^T$$

$$g_{xk}^2 + g_{yk}^2 + g_{zk}^2 = 1$$

Equation 2.1

For the sake of simple calculation, the setting of  $\lambda_1=1$  and  $\lambda_2/\lambda_3=1$  is adopted as stated above. In a second step, the gradient distribution within the cone defined by  $\Theta_{\max}$  can be calculated. The number of gradient sampling orientations (N) will be 6, 10, 20 and 30, respectively. The normalized gradient vectors are defined by  $\theta$  (Angle between gradient vector and Z axis) and  $\phi$  (Angle between the projection of the gradient vector on X-Y plane and X axis). The DGV coverage is restrained by  $\Theta_{\max}$ . Within the cone defined by  $\Theta_{\max}$ , the gradient vectors will be distributed uniformly with regards to  $\phi$ .

As stated above, it requires at least six non-collinear spatial orientations of diffusion gradients to determine the diffusion tensor. If the space filled by the gradients exceeds a hemisphere, there could be incompetent gradient vectors combination produced in experiments. Therefore in the simulation, such incompetent gradients vectors will be filtered out.

### **2.1.2.2 Producing the possible combination of homogeneous distributed N gradient vectors**

To calculate the individual gradient vectors for a given total number of gradients  $N$ ,  $\Theta_{\max}$  will be equally divided by  $N$  to produce  $\theta_k$  ( $i=1, 2, 3 \dots N$ ) and the maximum range of  $\phi$  ( $=360^\circ$ ) will also be equally divided by  $N$  to produce  $\phi_k$  ( $i=1, 2, 3 \dots N$ ). By the design criteria introduced in **chapter 2.1.1**, the subset of  $N$  gradient vectors can be selected from the whole set of gradient vectors. In principle, there are  $N!$  different possibilities of combination. If  $N=6$ , there would be  $6! = 720$  different gradient vector combinations. With  $N = 10$ , the number of combinations would be 362,880. For  $N=20$  and  $N=30$ , the number of combinations would be too large to allow for an exhaustive search.

Thus, for the gradient schemes with by  $N=20$  and  $N=30$ , the random sampling method will be used.

For each  $\Theta_{\max}$ , the full set of gradient vectors combinations ( $N=6$  and  $10$ ) and a partial set of gradient vectors combinations ( $N=20$  and  $30$ ) are calculated. The calculation is described below for  $N=6$  and different  $\Theta_{\max}$  ( $15^\circ, 30^\circ, 45^\circ, 60^\circ, 75^\circ, 90^\circ$ ).

Step 1: Calculate the increment of  $\Delta\phi$  and  $\Delta\theta$ :  $\Delta\phi=2\pi/6$  and  $\Delta\theta=\Theta_{\max}/6$ .

Step 2: Prepare the permutations of coefficient vector  $[x_1, x_2, x_3, x_4, x_5, x_6]$  which will multiply the increment of  $\Delta\phi$  and  $\Delta\theta$  for defining the spatial direction of each gradient vector. Assigning  $[x_1, x_2, x_3, x_4, x_5, x_6] = [1, 2, 3, 4, 5, 6]$ , then the full permutation of coefficient vector's elements can be expressed as a matrix denoted as PER with size of  $[720 \times 6]$ :

$$PER = \begin{bmatrix} p_{001.1} & p_{001.2} & p_{001.3} & p_{001.4} & p_{001.5} & p_{001.6} \\ p_{002.1} & p_{002.2} & p_{002.3} & p_{002.4} & p_{002.5} & p_{002.6} \\ p_{003.1} & p_{003.2} & p_{003.3} & p_{003.4} & p_{003.5} & p_{003.6} \\ \vdots & & & & & \\ p_{720.1} & p_{720.2} & p_{720.3} & p_{720.4} & p_{720.5} & p_{720.6} \end{bmatrix} = \begin{bmatrix} x_1 & x_2 & x_3 & x_4 & x_5 & x_6 \\ x_6 & x_5 & x_4 & x_3 & x_2 & x_1 \\ x_5 & x_4 & x_3 & x_2 & x_1 & x_6 \\ \vdots & & & & & \\ x_1 & x_5 & x_4 & x_6 & x_2 & x_3 \end{bmatrix}$$

Equation 2.2

Each row of matrix PER can produce one scheme, all together 720 rows represent 720 possibilities scheme pattern by 6 diffusion gradient directions.

Step 3: Calculate all possible combinations gradient vectors  $[g_1, g_2, g_3, g_4, g_5, g_6]$  to form the schemes. For simple interpretation, the last row from PER is taken out as an example.

The increment coefficients from the last row of PER as following:

$$PER = [p_{720.1} \ p_{720.2} \ p_{720.3} \ p_{720.4} \ p_{720.5} \ p_{720.6}] = [x_1 \ x_5 \ x_4 \ x_6 \ x_2 \ x_3] \\ = [1 \ 5 \ 4 \ 6 \ 2 \ 3]$$

The corresponding gradient vectors for the scheme from the first row of PER is:

$$\begin{aligned}
 g_1 &= \begin{bmatrix} \sin(\Delta\theta * x_1) * \sin(\Delta\phi * x_1) \\ \sin(\Delta\theta * x_1) * \cos(\Delta\phi * x_1) \\ \cos(\Delta\theta * x_1) \end{bmatrix} \\
 g_2 &= \begin{bmatrix} \sin(\Delta\theta * x_5) * \sin(\Delta\phi * x_5) \\ \sin(\Delta\theta * x_5) * \cos(\Delta\phi * x_5) \\ \cos(\Delta\theta * x_5) \end{bmatrix} \\
 g_3 &= \begin{bmatrix} \sin(\Delta\theta * x_4) * \sin(\Delta\phi * x_4) \\ \sin(\Delta\theta * x_4) * \cos(\Delta\phi * x_4) \\ \cos(\Delta\theta * x_4) \end{bmatrix} \\
 g_4 &= \begin{bmatrix} \sin(\Delta\theta * x_6) * \sin(\Delta\phi * x_6) \\ \sin(\Delta\theta * x_6) * \cos(\Delta\phi * x_6) \\ \cos(\Delta\theta * x_6) \end{bmatrix} \\
 g_5 &= \begin{bmatrix} \sin(\Delta\theta * x_2) * \sin(\Delta\phi * x_2) \\ \sin(\Delta\theta * x_2) * \cos(\Delta\phi * x_2) \\ \cos(\Delta\theta * x_2) \end{bmatrix} \\
 g_6 &= \begin{bmatrix} \sin(\Delta\theta * x_3) * \sin(\Delta\phi * x_3) \\ \sin(\Delta\theta * x_3) * \cos(\Delta\phi * x_3) \\ \cos(\Delta\theta * x_3) \end{bmatrix}
 \end{aligned}$$

*Equation 2.3*

It is easier to formulate the vectors in spherical coordinates:  $g_k(r, \theta, \phi)$ . As  $r$  is normalized to 1 (figure 2.4(a)), so the gradient vector can be simplified to  $g_k(\theta, \phi)$ , where  $\theta$  can adopt the following values  $[\frac{\theta_{\max}}{N}, 2 \frac{\theta_{\max}}{N}, 3 \frac{\theta_{\max}}{N}, \dots, N \frac{\theta_{\max}}{N}]$ , while  $\phi$  can adopt the values  $[\frac{2\pi}{N}, 2 \frac{2\pi}{N}, 3 \frac{2\pi}{N}, \dots, N \frac{2\pi}{N}]$  (see figure 2.4(b)).

To guarantee that the vector scheme is non-collinear, each  $\theta$  and each  $\phi$  can only be used one time. Then  $N$  sets  $(\theta_k, \phi_k)$  results in one DGV scheme; changing the combination of  $\theta$  and  $\phi$  results in  $N!$  DGV patterns. Figure 2.4(b) shows one example of a DGV scheme for  $N=6$ . Figure 2.4(c) shows possible diffusion gradient vectors for different  $\theta_{\max}$  ( $15^\circ, 30^\circ, 45^\circ, 60^\circ, 75^\circ, 90^\circ$ ).

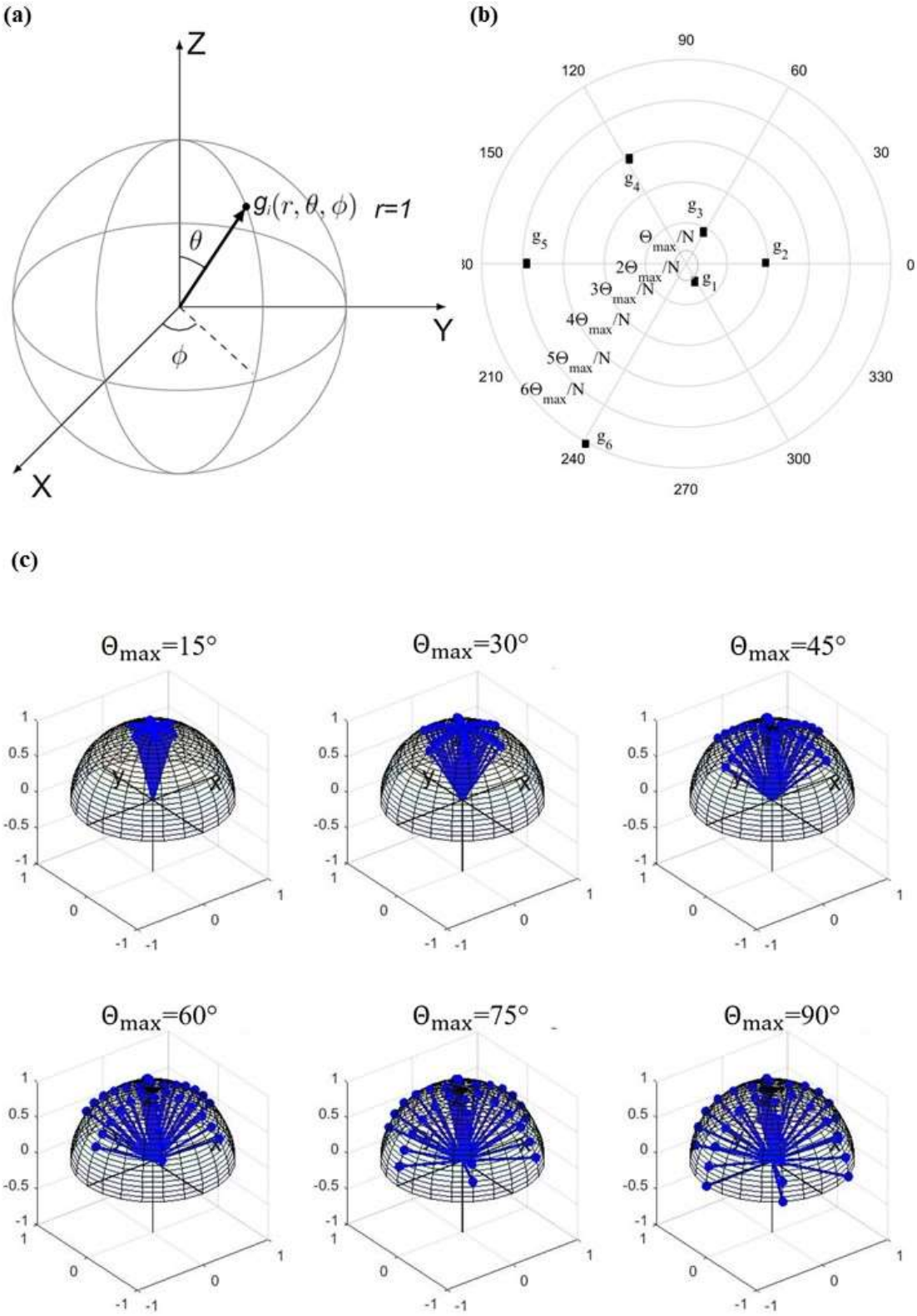


Figure 2.4: Example of DGV with  $N=6$ . (a): Gradient vector  $g(r, \theta, \phi)$  in spherical coordinates. (b): Example of a DGV scheme for  $N=6$ , the projection of the vector tip upon the X-Y plane is displayed. (c): Set of possible diffusion gradient vectors for different  $\theta_{max}$  ( $15^\circ, 30^\circ \dots 90^\circ$ ).



### 2.1.2.3 Monte-Carlo simulation and searching the optimal gradient scheme in different sphere coverages.

To examine the influence of the tailored diffusion gradient scheme upon the parameters calculated from DTI, the well accepted method of Monte Carlo simulation was performed. To keep the simulation as realistic as possible, specified Gaussian noise according to selected SNR was added to the calculated signal intensities. The simulation process consists of the following steps.

1. Selection of a range of typical FAs in peripheral nerves FAs: definition of a diffusion tensor with eigenvalues matching the eigenvalues found in volunteers/patients (Kronlage *et al.*, 2018).
2. Selection of the b values ( $b=0$  and  $b=1000$  s/mm<sup>2</sup>), number of gradients N and gradient sampling scheme.
3. Selection of a signal-to-noise ratio which is similar to the SNR achieved in DTI at 3 Tesla in peripheral nerves (the reference comes from evaluation of practical measurements on the scanner and coil which used for validation in this project).
4. Definition of the fiber direction.
5. Definition of the theoretical  $S_0$  for  $b_0=0$  and calculation of  $S_k$  for each gradient direction  $\hat{g}_k$ .
6. Mixing of noise with noise level defined in step 3 to each defined/calculated  $S_0$  and  $S_i$ .
7. Calculation of the diffusion tensor.
8. Calculation of eigenvalues and FA from the tensor.
9. Repeat steps of 6–8 minimum 10000 times.
10. Repeat steps 4–9 for a set of directions.

The individual steps of the simulation are performed in detail as given below:

1. In a comprehensive study in healthy volunteers of different age, Kronlage et al have found that FA varies between 0.34 and 0.79 (Kronlage *et al.* 2018). As representative values for this physiological range, three FA values: 0.4, 0.6, and 0.8 were selected with  $\lambda_3=\lambda_2<\lambda_1$ , and for  $\lambda_1=1$ , the  $\lambda_3=\lambda_2$  is calculated as follows:

$$\lambda_3 = \lambda_2 = \frac{(FA * \sqrt{3 - 2 * FA^2} - 1)}{(2 * (2 * FA^2 - 1))}$$

Equation 2.4

To guarantee integer ratios of  $\lambda_1$  and  $\lambda_3=\lambda_2$ , the FAs chosen initially were slightly changed. For the range of values of RD, AD, and FA obtained from the study of Kronlage (Kronlage *et al.*, 2018), the tensor was calculated according to table 2.1.

Table 2.1: FA, b value and corresponding derived diagonal tensor  $D_0$  and ratio of the eigenvalues used in simulations.

b value	Principle FA	$D_0$	$\lambda_1:\lambda_2:\lambda_3$
1000	0.408	$\begin{bmatrix} .0011 & 0 & 0 \\ 0 & .0011 & 0 \\ 0 & 0 & .00213 \end{bmatrix}$	2:1:1
1000	0.603	$\begin{bmatrix} .00071 & 0 & 0 \\ 0 & .00071 & 0 \\ 0 & 0 & .00213 \end{bmatrix}$	3:1:1
1000	0.808	$\begin{bmatrix} .00036 & 0 & 0 \\ 0 & .00036 & 0 \\ 0 & 0 & .00065 \end{bmatrix}$	6:1:1

## 2. Selection of a b value and gradient sampling scheme.

To calculate ADC map, it requires measurements with at least two b values. Usually, one is with lower value such as 0 s/mm<sup>2</sup> or similar level with imaging gradients around 1–5 s/mm<sup>2</sup>. The second b value for diffusion weight is typically chosen as about 1,000 s/mm<sup>2</sup>, but this is just the parameter that is often adapted to the structure of interest; b values of 3,000 s/mm<sup>2</sup> or even higher. More than 2 of higher b are rarely used in DTI, as this requires the method of least-squares fit to acquire the ADC in each direction. Furthermore in clinical practice two or more b-values >0 are not feasible as this leads to a significant extension of acquisition time. Therefore, in the present simulation studies two b-values are used with b=0 and 1000 s/mm<sup>2</sup>.

In this simulation, different gradient sampling schemes for N=6, N=10, N=20, and 30 are compared. As shown in **chapter 2.1.2.2**, for N=6 and N=10 all permutation (720 for N=6,

362880 for  $N=10$ ) can be used, while, for  $N=20$  and  $N=30$ , gradient schemes are selected by a random sampling method; this process is repeated 10 times

### 3. Selection of a signal-to-noise ratio.

The SNR of a DTI simulation usually refers to the SNR of the  $b_0$  data. Data with a b-value  $>0$  have lower SNR, depending on the value of b and the diffusivity  $D_i$  in the respective diffusion direction. In DTI studies in peripheral nerves that we have performed in our department, we typically find an SNR value of 15:1 to 30:1. This can be increased by signal averaging. It may be useful to include simulations with high SNR (50:1 or higher) to reveal intrinsic properties and trends. In this study, it is important to consider the Rician statistics bias in low SNR which can introduce artifacts into the data (Farzinfar *et al.*, 2013). Experiments with the fiber phantom at the 3 Tesla scanner (TIM Trio, Siemens Healthineers, Erlangen, Germany) using 15-channel Transmit/Receive knee coil (Quality Electrodynamics 700 Beta Drive, Suite 100 Mayfield Village, OH 44143, USA. distributed by SIEMENS Healthineers, Erlangen, Germany) showed that SNR is about 15:1. Therefore, in this simulation study SNR was set to 15:1.

### 4. Setting up the fiber direction.

Although the large trunks of the peripheral nerves roughly run along the body axis which in turn equals the scanner axis (Z-direction), there are always slight variation from the main direction. This means that the coordinate system of the nerve (X, Y, Z) may be tilted by  $\Theta$  and rotated by  $\Phi$ . Therefore simulations were performed for  $\Theta=0^\circ, 10^\circ, 20^\circ, \text{ and } 30^\circ$ . As the diffusion propagator is rotationally symmetric with respect to its z-axis, results should be independent of  $\Phi$ . Therefore,  $\Phi$  was set to  $=0$  throughout simulations. Within the simulation process, the diffusion tensor is calculated for all gradient schemes defined in step 2 under random noise pollution (SNR as defined in step 3) for each fiber orientation angle  $\Theta$ .

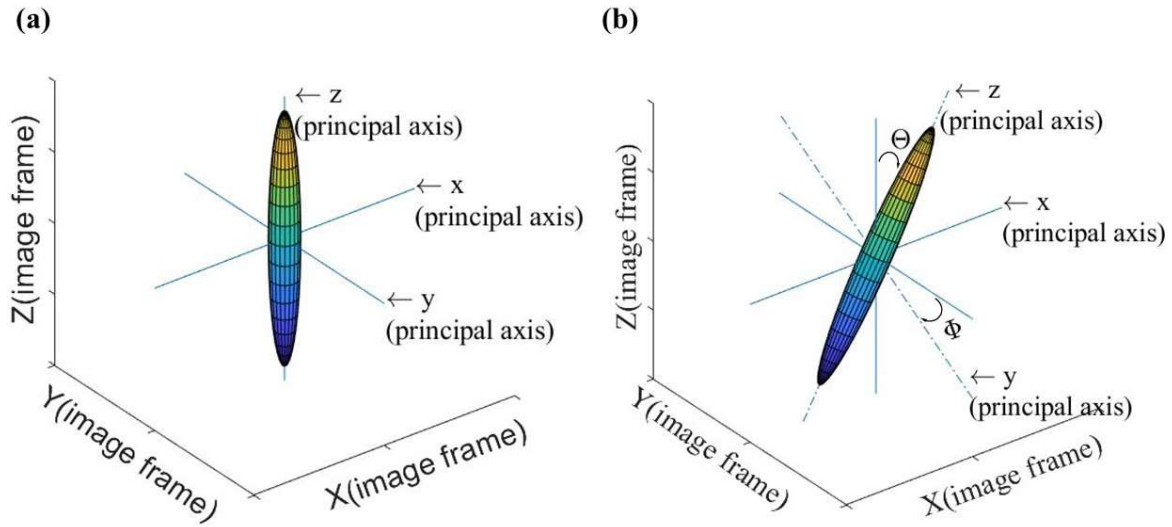


Figure 2.5: Coordinate systems of the scanner and nerve. (a) If the nerve is aligned with the scanner axis, scanner coordinate system (X, Y, Z) corresponds to the nerve coordinate system (x, y, z). (b) Shows the configuration if the nerve is slightly tilted with regards to the scanner coordinate system. In this case the nerve coordinate system is tilted ( $\Theta$ ) and rotated ( $\Phi$ ) with respect to the scanner coordinate system.

The diagonal matrix of the diffusion tensor in figure 2.5(a) will be represented by assigning the eigenvalues  $\lambda_i$  according to equation 1.21

$$D_{diagonal} = D' = \begin{bmatrix} \lambda_1 & 0 & 0 \\ 0 & \lambda_2 & 0 \\ 0 & 0 & \lambda_3 \end{bmatrix}$$

If the nerve is tilted by  $\Theta$  with regards to the scanner coordinate system ( $\Phi=0$ ) the respective representation of the diffusion tensor within the scanner coordinate system can be calculated using the rotation matrix R:

$$R = \begin{bmatrix} \cos\theta & 0 & -\sin\theta \\ 0 & 1 & 0 \\ \sin\theta & 0 & \cos\theta \end{bmatrix}$$

Equation 2.5

Then the diffusion tensor is:

$$D = R^T D_{diagonal} R$$

*Equation 2.6*

5. With  $S_0(b_0) = 1$ , the diffusion weighted signals  $S_k$  for each gradient direction  $\hat{g}_k$  can be calculated using equation 1.12. As gradient vectors number is  $N$ , the signal matrix will be composed as follows:

$$[S_0 \ S_1 \ S_2 \ \dots \ S_N]$$

*Equation 2.7*

6. Mixing noise into the signal  $S_0$  and  $S_k$ : Gaussian distributed noise is added separately to the real part  $n_R$  and the imaginary part  $n_I$ , respectively. With this, the noise magnitude  $n$

$$n = \sqrt{n_r^2 + n_i^2}$$

*Equation 2.8*

exhibits a Rayleigh distribution.

Random noise  $n$  is produced for each signal within the matrix (see equation 2.7):

$$[n_0 \ n_1 \ n_2 \ \dots \ n_N]$$

*Equation 2.9*

In a final step, the noise contaminated signal is obtained by adding matrix (Equation 2.7) and matrix (Equation 2.9).

7. Calculation of the tensor  $D_n$  according to equation 1.12 can be performed analytically if the measurements are performed in six directions. However, it requires a fitting procedure for more than six directions. Therefore, for  $N > 10$  the least squares estimation method is used.

8. From Tensor  $D_n$ , FA calculation is performed by using equation 1.25. Other parameters as MD, AD, RD and eigenvectors, are not the focus in this study, therefore they were not calculated.

9. Monte Carlo simulation with at least 10000 simulations is considered sufficient by industry standards. Therefore, steps 6-8 were repeated with different random noise 10000 times. This resulted in 10000 FAs for each number of diffusion directions, gradient scheme and nerve tilting angle.

10. Mean value and standard deviation were derived from the collected FAs.

11. The entire simulation process was repeated for different FA, SNR, sampling scheme (number of directions, N, gradient orientations, nerve orientation).

The Monte-Carlo computer simulation was implemented as a MATLAB program on the basis of *MathWorks<sup>R</sup> MATLAB<sup>R</sup> R2017a*.

#### **2.1.2.4 Criteria of evaluation.**

For a specified diffusion direction number N, there are infinite possibilities to design the distribution for the N non-collinear gradient directions in 3D space. Finding the optimal distribution currently is an area of research in DTI. So far, the consensus is to distribute the diffusion gradient directions as uniformly as possible within the three dimensions (Bernstein *et al.*, 2004). A common criterion which is already well accepted in evaluating the diffusion gradient scheme is to minimize the condition number of the transformation matrix of the diffusion gradient scheme (Skare *et al.*, 2000a).

The condition number as a quality metrics is used in the evaluation of noise propagation within DTI (Skare *et al.*, 2000a). By numerical analysis, the condition number measures how much the output value of a function will change for a small change in the input. Since the diffusion tensor is correlated with the measured ADC values by the transformation matrix which correlates with diffusion gradient scheme, theoretically the CN of this transformation matrix can be used to measure how sensitive the diffusion tensor is to changes or errors in the acquired ADC. Hence, the CN is a measure for the difference between the measured diffusion tensor  $D_n$  and the true diffusion tensor  $D_0$ . The CN can therefore be regarded as an index of noise sensitivity of the given gradient scheme.

The transformation matrix for a DTI diffusion gradient scheme (Skare *et al.*, 2000a) will be expressed based on the equation 1.10 and equation 1.14, supposing the elements of transformation matrix are  $c_k$ :

$$c_k = \widehat{g}_k^T \cdot \widehat{g}_k = (g_{kx}^2 \ g_{ky}^2 \ g_{kz}^2 \ 2g_{kx}g_{ky} \ 2g_{kx}g_{kz} \ 2g_{ky}g_{kz})^T$$

Where  $k=1,2,3\dots N$

*Equation 2.10*

The tensor elements can be grouped to a vector  $d$ :

$$d = (D_{xx} \ D_{yy} \ D_{zz} \ D_{xy} \ D_{xz} \ D_{yz})^T$$

*Equation 2.11*

For the measurements using a generalized DTI gradient vector scheme with  $N \geq 6$  different gradient directions, a matrix  $C$  with dimension  $N \times 6$  can be defined as:

$$C = (c_1 \ c_2 \ c_3 \ \dots \ c_N)^T$$

*Equation 2.12*

It is referred to as the transformation matrix for the corresponding DTI scheme.

With regard to the vector  $d$ , the Euclidean norm of the vector  $\|d\|$  can be expressed as:

$$\|d\| = \left( \sum_{k=1,2\dots N} d_k^2 \right)^{\frac{1}{2}}$$

*Equation 2.13*

The norm of a matrix  $C$  reflects how much extent by matrix  $C$  can stretch the vector  $d$ :

$$\|C\| = \max \frac{\|Cd\|}{\|d\|}$$

*Equation 2.14*

The scalar quantity  $\|C\| \|C^{-1}\|$  is the CN of matrix  $C$  and is denoted by  $\text{Cond}(C)$  in this study.

In the present study, the CN was calculated using a dedicated MATLAB function.

To find the optimum gradient scheme a two-step process was used. Firstly, for each  $\Theta_{\max}$  the directional distribution was singled out that showed the lowest standard deviation in FA for the 10000 repetitions of step 6 to 8 within the simulation. This results in an optimum gradient scheme for each number of gradients (6, 10, 20, 30).

The results of the simulation study were verified in phantom as described in **chapter 3.1.3**.



### 2.1.3 Conventional Gradient Vector Schemes

In order to check the performance of the final optimal DGV schemes in phantom experiments, these schemes were compared to three different gradient schemes with uniform gradient distribution: the standard gradient scheme of the manufacturer (SIEMENS Healthineers, Erlangen, Germany), Jones' optimal schemes (Jones, 2004) and the schemes developed by Downhill Simplex Minimization (Skare *et al.*, 2000a). In order to do that, schemes with the same number of gradients (6, 12, 20, 30) were calculated for these three gradient distributions:

***Siemens standard gradient scheme:***

The gradient directions with  $N=6$  follows orthogonal distribution which are along  $\pm X$ ,  $\pm Y$  and  $\pm Z$ . For  $N=10$ , 20 and 30 the schemes are calculated according to certain geometric shapes (e.g.: platonic solids and their variants).

***Jones' optimal schemes:***

Based on the uniformly distributed gradient vectors, this scheme is optimized by the minimization of error propagation for the estimation of the tensor trace (Jones, 2004).

***Downhill Simplex Minimization:***

This scheme is based on the electrostatic repulsion phenomenon: The tips of the gradients represent positive charged particles which are arranged on a spherical surface according to the laws of electrostatic repulsion. In order to do this, the sum of electronic repulsive force between those particles is calculated and minimized by DSM.

The conventional gradient schemes are listed in table 2.2-2.4

Table 2.2: SIEMENS gradient Schemes

N=6			N=20			N=30		
g <sub>x</sub>	g <sub>y</sub>	g <sub>z</sub>	g <sub>x</sub>	g <sub>y</sub>	g <sub>z</sub>	g <sub>x</sub>	g <sub>y</sub>	g <sub>z</sub>
1.0000	0.0000	1.0000	1.0000	0.0000	0.0000	-0.2081	0.5255	0.8500
-1.0000	0.0000	1.0000	0.0000	1.0000	0.0000	0.2024	0.5261	0.8510
0.0000	1.0000	1.0000	-0.0320	0.7996	0.5997	0.4100	0.1753	0.9183
0.0000	1.0000	-1.0000	0.8567	0.4938	-0.1489	-0.4126	0.7426	0.5659
1.0000	1.0000	0.0000	0.8344	0.3092	0.4562	-0.2071	0.9595	0.2801
-1.0000	1.0000	0.0000	0.8344	-0.3092	0.4562	-0.8727	0.5255	0.0648
N=10			0.8567	-0.4938	-0.1489	-0.7468	0.5261	0.4554
			0.8222	0.0000	-0.5692	-0.4152	0.1755	0.9158
			0.5508	0.4259	-0.7178	-0.7466	0.1753	0.6736
			0.4682	0.8343	-0.2911	-0.6657	0.7426	-0.2176
			0.5159	0.8089	0.2820	-0.3304	0.9595	-0.1105
g <sub>x</sub>	g <sub>y</sub>	g <sub>z</sub>	0.3919	0.5159	0.7618	-0.3313	0.5255	-0.8100
0.0000	0.8090	0.6180	0.4782	0.0000	0.8783	-0.6639	0.5261	-0.5695
0.0000	0.1910	1.0000	0.3919	-0.5159	0.7618	-0.9993	0.1755	-0.1119
-0.5878	0.8090	0.1910	0.5159	-0.8089	0.2820	-0.8714	0.1753	-0.5019
-0.9511	0.1910	0.3090	0.4682	-0.8343	-0.2911	0.0012	0.7426	-0.7004
-0.3633	0.8090	-0.5000	0.5508	-0.4259	-0.7178	0.0029	0.9595	-0.3484
-0.5878	0.1910	-0.8090	0.1110	-0.2640	-0.9581	0.6680	0.5255	-0.5654
0.3633	0.8090	-0.5000	0.1110	0.2640	-0.9581	0.3365	0.5261	-0.8074
0.5878	0.1910	-0.8090	0.0320	0.7996	-0.5997	0.2024	-0.1755	0.9850
0.5878	0.8090	0.1910				0.2081	0.1753	-0.9838
0.9511	0.1910	0.3090				0.6665	0.7426	-0.2153
						0.3322	0.9595	-0.1049
						0.2051	0.9584	0.2854
						0.4126	0.7426	0.5659
						0.7461	0.1753	0.6742
						0.7441	0.5255	0.4606
						0.8719	0.5261	0.0705
						0.8743	0.1755	-0.4968
						1.0000	0.1753	-0.1061

Table 2.3: Jones gradient schemes

N=6			N=20			N=30		
$g_x$	$g_y$	$g_z$	$g_x$	$g_y$	$g_z$	$g_x$	$g_y$	$g_z$
1.0000	0.0000	0.0000	1.0000	0.0000	0.0000	1.0000	0.0000	0.0000
0.4460	0.8950	0.0000	0.3360	0.9420	0.0000	0.1660	0.9860	0.0000
0.4470	0.2750	0.8510	-0.4050	0.6060	0.6850	-0.1100	0.6640	0.7400
0.4480	-0.7230	-0.5250	0.8250	-0.5130	-0.2360	0.9010	-0.4190	-0.1100
0.4470	-0.7240	0.5260	0.0060	-0.3630	0.9320	-0.1690	-0.6010	0.7810
-0.4490	-0.2770	0.8500	-0.8110	-0.2870	0.5100	-0.8150	-0.3860	0.4330
N=10			0.8520	-0.3200	0.4140	0.6560	0.3660	0.6600
$g_x$ $g_y$ $g_z$			-0.2400	0.9590	0.1490	0.5820	0.8000	0.1430
1.0000	0.0000	0.0000	0.8350	0.2720	0.4780	0.9000	0.2590	0.3500
0.6780	0.7350	0.0000	0.0090	-0.9040	0.4270	0.6930	-0.6980	0.1780
-0.5560	0.5040	0.6610	-0.0630	-0.8120	-0.5800	0.3570	-0.9240	-0.1400
0.6720	-0.7330	0.1060	-0.2690	-0.3900	-0.8810	0.5430	-0.4880	-0.6830
-0.0120	-0.8010	0.5980	-0.4220	-0.6240	0.6580	-0.5250	-0.3960	0.7530
-0.6800	-0.3100	0.6440	-0.6010	0.7790	-0.1770	-0.6390	0.6890	0.3410
-0.0450	-0.0110	0.9990	-0.5160	0.0860	-0.8520	-0.3300	-0.0130	-0.9440
-0.0240	0.9660	0.2570	-0.7900	-0.6070	0.0870	-0.5240	-0.7830	0.3350
0.4580	0.5210	0.7210	0.7290	-0.1810	-0.6610	0.6090	-0.0650	-0.7910
0.6580	-0.2500	0.7100	0.2650	-0.0960	-0.9600	0.2200	-0.2330	-0.9470
			-0.5610	-0.7010	-0.4400	-0.0040	-0.9100	-0.4150
			-0.4050	0.6310	-0.6620	-0.5110	0.6270	-0.5890
						0.4140	0.7370	0.5350
						-0.6790	0.1390	-0.7210
						0.8840	-0.2960	0.3620
						0.2620	0.4320	0.8630
						0.0880	0.1850	-0.9790
						0.2940	-0.9070	0.3020
						0.8870	-0.0890	-0.4530
						0.2570	-0.4430	0.8590
						0.0860	0.8670	-0.4910
						0.8630	0.5040	-0.0250

Table 2.4: DSM Schemes

N=6			N=20			N=30		
$g_x$	$g_y$	$g_z$	$g_x$	$g_y$	$g_z$	$g_x$	$g_y$	$g_z$
0.9100	0.4160	0.0000	0.9990	-0.0130	0.0440	0.9950	0.0790	0.0680
0.0000	0.9100	0.4160	0.1390	0.9890	0.0480	0.0290	0.9950	0.0970
0.4160	0.0000	0.9100	-0.2730	0.2920	0.9170	-0.1280	0.5330	0.8360
0.9100	-0.4160	0.0000	0.9050	-0.4210	-0.0490	0.9780	-0.1960	0.0680
0.0000	0.9100	-0.4160	0.0630	-0.2010	0.9770	-0.0850	-0.6320	0.7700
-0.4160	0.0000	0.9100	-0.8530	-0.2680	0.4490	-0.8870	-0.2550	0.3850
N=10			0.9590	-0.0540	0.2770	0.5410	0.4860	0.6870
$g_x$			-0.2410	0.9610	0.1370	0.4430	0.8890	0.1210
$g_y$			0.8750	0.2170	0.4330	0.9710	0.2030	0.1250
$g_z$			-0.0430	-0.9230	0.3820	0.4590	-0.8870	0.0510
0.9970	0.0470	-0.0630	-0.0250	-0.8970	-0.4420	0.3890	-0.9120	-0.1320
0.4790	0.8420	0.2480	-0.2240	-0.3320	-0.9160	0.6020	-0.5100	-0.6140
-0.2990	0.5490	0.7800	-0.2820	-0.6390	0.7160	-0.2870	-0.4170	0.8630
0.7160	-0.6980	0.0280	-0.5890	0.8070	-0.0430	-0.8070	0.5660	0.1660
0.0010	-0.8640	0.5040	-0.3420	-0.0470	-0.9380	-0.1620	-0.2090	-0.9640
-0.8050	-0.2300	0.5470	-0.8580	-0.5120	0.0490	-0.3280	-0.9170	0.2260
-0.0260	-0.1910	0.9810	0.7960	-0.2050	-0.5690	0.5520	0.0190	-0.8340
-0.0030	0.9970	0.0710	0.2260	-0.0600	-0.9720	0.3200	-0.0460	-0.9640
0.2350	0.0580	0.9700	-0.3420	-0.9280	-0.1510	-0.0370	-0.9820	-0.1850
0.8970	0.0140	0.4410	-0.3830	0.5860	-0.7140	-0.6570	0.2930	-0.6950
						0.3620	0.8200	0.4430
						-0.6860	0.1640	-0.7090
						0.9770	-0.1710	0.1290
						-0.0140	0.2290	0.9730
						-0.1100	0.2600	-0.9590
						0.1920	-0.9210	0.3400
						0.9880	0.0530	-0.1460
						0.1930	-0.0770	0.9780
						0.0050	0.9610	-0.2750
						0.8730	0.4590	-0.1660

## 2.2 Noise Correction

In order to obtain an effective noise correction in DTI images, it is necessary to understand firstly the general noise propagation process in multi order function and to figure out its actual situation in DTI.

### 2.2.1 Noise propagation in DTI

Noise is the deviation of a measured variable, such as electronic current, voltage of signal, from the true value. In MRI, noise can occur from various sources and normally has no particular pattern. The parameters, e.g. in DTI derived from noisy signal intensities exhibit noise. Noise can introduce a bias (systematic deviation) as well as scatter (random deviation) in the data. In principle, noise introduced during MRI measurements is supposed to have a mean of zero, which means, there are equal probabilities of negative and positive deviations from the true signal intensity value. It is considered to have a Gaussian distribution with mean values denoted as  $\mu$  and standard deviation denoted as  $\sigma$ . In addition to noise, the digitalization process from analog signal to digital data which can be used in computing can arouse another type of error mixed in noise, it is call Rounding Error (or Round-off Error), however in MRI, with advanced sampling hardware, such error is usually much smaller than the noise level, and is commonly ignored in consideration and simulations.

When noisy data are used for the calculation of other parameters, the noise in the data propagates into the other parameters in predictable ways (Bevington and Robinson, 2003). The commonly used propagation-of-error formulas assume a first-order linear approximation of a function. The noise in a calculated parameter can be estimated from the noise in the original data by standard propagation-of-error formulas (Farrance and Frenkel, 2012), here the examples are based on a function  $f$  with the variable:  $u$ , and  $u$  is a function of the variables  $r, i$ . The variance of function  $f$  can be expressed as:

$$\sigma^2[f(u)] = \sigma_u^2 \left(\frac{\partial f}{\partial u}\right)^2$$

$$\sigma_u^2 = \sigma_r^2 \left(\frac{\partial u}{\partial r}\right)^2 + \sigma_i^2 \left(\frac{\partial u}{\partial i}\right)^2$$

*Equation 2.15*

Propagation of errors from r and i into function f yields:

$$\sigma_f^2 = \sigma_u^2 \left(\frac{\partial f}{\partial u}\right)^2 = \sigma_r^2 \left(\frac{\partial f}{\partial u}\right)^2 \left(\frac{\partial u}{\partial r}\right)^2 + \sigma_i^2 \left(\frac{\partial f}{\partial u}\right)^2 \left(\frac{\partial u}{\partial i}\right)^2$$

*Equation 2.16*

Applying the above mentioned formulas to noise propagation in DTI, the final variance on tensor elements can be derived from original Gaussian variances step by step.

The signal magnitude is derived as square root of the sum of real part and imaginary part of the signal. This signal in turn is a result of the Fourier Transformation of the measured signal. On the other hand, the signal magnitude is further processed for derivation of the diffusion tensor. Thus, there are three stages that determine the error propagation: the first stage is the Fourier transformation which produces the variables r, i as real and imaginary parts respectively and the second stage is assuming function u as the square root operation for r and i :  $u(r, i) = (r^2 + i^2)^{1/2}$ ; the third consideration will be made for DTI derivation: according to equation 1.16, the magnitude signal will go through the logarithm operation for linear calculation of the tensor elements, thus, it is reasonable to assume the function f as logarithm process for the obtained magnitude signal intensity:  $f(u) = \ln(u)$ .

Furthermore, due to the linear and orthogonal characteristics of the Fourier transform, the real and imaginary part are successfully inherit the Gaussian characteristics of the original quadrature detected data, then the variances  $\sigma_r^2 = \sigma_i^2$  follow the  $\sigma^2$  from the Gaussian distribution. For the second stage of square root operation (which is non-linear mapping), even though the variance of u will follow its actual probability distribution according to SNR (Rayleigh distribution with SNR lower than 1 and gradually approximate to Gaussian distribution with SNR larger than 3) (Gudbjartsson and Patz, 1995), this will not affect the final variance' derivation for f(u) in third stage.

According to the equation 2.16:

$$\sigma_f^2 = \sigma_r^2 \left(\frac{1}{u}\right)^2 (r)^2 + \sigma_i^2 \left(\frac{1}{u}\right)^2 (i)^2 = \frac{\sigma_r^2 (r)^2 + \sigma_i^2 (i)^2}{(r)^2 + (i)^2} = \sigma^2$$

*Equation 2.17*

For the sake of a simple interpretation, the tensor elements vector  $d$  was expressed according to the six directions gradient scheme  $G$ :

$$d = [D_{xx}, D_{yy}, D_{zz}, D_{xy}, D_{xz}, D_{yz}]^T$$

*Equation 2.18*

$$G_k = [g_{xk}^2, g_{yk}^2, g_{zk}^2, 2g_{xk}g_{yk}, 2g_{xk}g_{zk}, 2g_{yk}g_{zk}]$$

$$G = [G_1 G_2 G_3 G_4 G_5 G_6]^T$$

*Equation 2.19*

The ADC can be derived from equation 1.16

$$f_k(u) = D_k = -\ln(S_k/S_0) / b$$

$$F = [f_1, f_2, f_3, f_4, f_5, f_6]^T = [D_1, D_2, D_3, D_4, D_5, D_6]^T$$

*Equation 2.20*

In the presence of noise, equation 1.16 can be expressed as another form:

$$F = Gd$$

*Equation 2.21*

With known diffusion, the gradient scheme's information G and obtained measurement data F, the solution from the following equation system will be the expression of tensor elements.

$$\begin{aligned}
 f_1 &= g_{x1}^2 D_{xx} + g_{y1}^2 D_{yy} + g_{z1}^2 D_{zz} + 2g_{x1}g_{y1}D_{xy} + 2g_{x1}g_{z1}D_{xz} + 2g_{y1}g_{z1}D_{yz} \\
 &\vdots \\
 f_6 &= g_{x6}^2 D_{xx} + g_{y6}^2 D_{yy} + g_{z6}^2 D_{zz} + 2g_{x6}g_{y6}D_{xy} + 2g_{x6}g_{z6}D_{xz} + 2g_{y6}g_{z6}D_{yz}
 \end{aligned}$$

*Equation 2.22*

Equation 2.22 can be resolved through an inverse function which is a commonly build-in function in MATLAB. The solution indicates that each diffusion tensor element could be expressed by one order linear function of  $[f_1, f_2, f_3, f_4, f_5, f_6]$ :

$$\begin{aligned}
 D_{xx} &= a_{11}f_1 + a_{12}f_2 + a_{13}f_3 + a_{14}f_4 + a_{15}f_5 + a_{16}f_6 + b_1 \\
 D_{yy} &= a_{21}f_1 + a_{22}f_2 + a_{23}f_3 + a_{24}f_4 + a_{25}f_5 + a_{26}f_6 + b_2 \\
 D_{zz} &= a_{31}f_1 + a_{32}f_2 + a_{33}f_3 + a_{34}f_4 + a_{35}f_5 + a_{36}f_6 + b_3 \\
 D_{xy} &= a_{41}f_1 + a_{42}f_2 + a_{43}f_3 + a_{44}f_4 + a_{45}f_5 + a_{46}f_6 + b_4 \\
 D_{xz} &= a_{51}f_1 + a_{52}f_2 + a_{53}f_3 + a_{54}f_4 + a_{55}f_5 + a_{56}f_6 + b_5 \\
 D_{yz} &= a_{61}f_1 + a_{62}f_2 + a_{63}f_3 + a_{64}f_4 + a_{65}f_5 + a_{66}f_6 + b_6
 \end{aligned}$$

*Equation 2.23*

The constant matrix  $[a_{kl}]$   $k,l=1,2,3,4,5,6$ ; and constant vector  $[b_k]$   $k=1,2,3,4,5,6$ , are correlated with and derived from the diffusion gradient scheme G.

According to equation 2.23, the final error propagation on each tensor element is correlated with the Gaussian variant by the constant coefficients which are determined by the diffusion gradient scheme.



### 2.2.2 Noise correction methods

Several studies have shown, that diffusivity is underestimated in the presence of noise, as there is a “noise floor” due to the Rician noise in diffusion-weighted images (Wirestam *et al.*, 2006). With other indices such as FA or RD and AD, things are even more complicated. Jones and Basser have shown, that in the presence of noise, FA will be overestimated for low to mid-range b-values, but will be underestimated for high b-values (Jones and Basser, 2004). They also showed that within the diffusion propagator, noise mainly affects the axial diffusion.

As stated above, diffusion weighted imaging is more sensitive to noise than standard morphologic imaging techniques. This affects the parameters calculated from DTI as well. Therefore, noise correction in DTI post processing plays an important role. Noise in magnitude images is originating from RF detection and governed by Rician distribution (Basu *et al.*, 2006; Gudbjartsson and Patz, 1995). In this thesis two noise correction methods which are well accepted in routine MR magnitude imaging are compared: the power images method (Miller and Joseph, 1993) and the correction factor method (Gudbjartsson and Patz, 1995).

Table 2.5 lists the parameters that play a role in noise correction.

*Table 2.5:* Table of variables used in the noise correction.

---

A:	Signal intensity without noise.
M:	Noisy signal intensity.
$M_0$ :	Noise only signal intensity.
$\sigma$ :	Standard deviation of true noise.
$\langle \rangle$ :	Average over fluctuations.
n:	Noise.
$n_R$ :	Gaussian noise in real part.
$n_I$ :	Gaussian noise in imaginary part.

---

### 2.2.2.1 Power images method

The correction method using power images (Miller and Joseph, 1993) assumes that the MR signal is measured by quadrature coils. In this case, signal A is composed of a real part  $A_R$  and an imaginary part  $A_I$  as well as the complex noise n from quadrature detectors  $n_R$  and  $n_I$ :

$$M^2 = (A_R + n_R)^2 + (A_I + n_I)^2 = A_R^2 + A_I^2 + 2A_R n_R + 2A_I n_I + n_R^2 + n_I^2$$

*Equation 2.24*

The average power of M can be expressed as:

$$\langle M^2 \rangle = A_R^2 + A_I^2 + 2A_R \langle n_R \rangle + 2A_I \langle n_I \rangle + \langle n_R^2 \rangle + \langle n_I^2 \rangle$$

*Equation 2.25*

Assuming that the noise from the real and imaginary parts have an independent Gaussian distribution with zero mean and standard deviation  $\sigma$ , then equation 2.25 will be simplified as follows:

$$\langle M^2 \rangle = A^2 + 2 * \sigma^2$$

*Equation 2.26*

If  $A=0$ , the average of the noise power  $M_0$  will be  $\langle M_0^2 \rangle = 2 * \sigma^2$ . Then the true signal A can be estimated as:

$$A^2 = \langle M^2 \rangle - \langle M_0^2 \rangle$$

*Equation 2.27*

One can use this to calculate the diffusivity D from the signal of a diffusion-weighted sequence with diffusion weighting b:

$$A^2(b) = S_0^2 e^{-b(2D)}$$

*Equation 2.28*

### 2.2.2.2 Correction factor method

Gudbjartsson and Patz used a different method to correct for noise. They assumed that the noise intensity  $M_0$  is described by a Rayleigh distribution with known mean and variance. This noise distribution can be measured in regions where no signal of the object and no artifact-related signal (ghosts or wrap-around artifacts) is presented (Gudbjartsson and Patz, 1995). In this case:

$$\bar{M}_0 = \sigma * \sqrt{\frac{\pi}{2}} \quad \text{or} \quad \sigma_{M_0}^2 = \left(2 - \frac{\pi}{2}\right) * \sigma^2$$

*Equation 2.29*

The true noise power  $\sigma^2$  according to equation 2.29 can be used together with the measured signal intensity  $M$ , to estimate the correct signal  $A$  which can be derived as follows:

$$A = \sqrt{|\bar{M}^2 - \sigma^2|}$$

*Equation 2.30*

This in turn can be applied in the diffusion equation for tensor matrix derivation:

$$A(b) = S_0 e^{[-b(D)]}$$

*Equation 2.31*

### 2.2.2.3 Simulation

Instead of single pixel simulation for optimization of the gradient scheme (**chapter 2.1.2.3**), the simulation for correction methods is based on image matrix.

1. Simulated image was composed by matrix size of 10x10 pixels.
2. The anisotropy in noise correction simulation only focus on FA=0.6.
3. Selection of the  $b$  values ( $b=0$  and  $b=1000$  s/mm<sup>2</sup>). While all gradient schemes (Siemens, Jones, DSM, and tailored diffusion gradient schemes) were used for

simulation to retrieve the optimum gradient scheme, simulation for noise correction was performed using the Siemens gradient scheme with  $N=6, 10, 20$  and  $30$ .

4. In order to put stress on the error propagation through noise, SNR was set to 6 to match the SNR obtained in the DTI measurements of phantom (**chapter 2.3.2**).
5. Fiber direction fixed on  $(\Theta=0, \Phi=0)$ .
6. Preparing the theoretical  $S_0$   $10 \times 10$  matrix for  $b_0$  and calculating  $S_k$   $10 \times 10$  matrix for each gradient direction  $\hat{g}_k$ . Producing the corresponding noise matrixes  $n_0$  and  $n_k$ , mixing them to  $S_0$  matrix and  $S_k$  matrix respectively.

The operation on matrix followed the steps of 7-10 as described in **chapter 2.1.2.3**.

To simulate noise correction, the uncorrected FA was determined as mean value of the FA map derived from the simulations. Corrected FAs were determined by using of the powered noise (**chapter 2.2.3.1**) for the power image method; for the correction factor method the results of

two approximations to noise variance  $\sigma$  were compared:  $\sqrt{\frac{2}{\pi}} \langle n \rangle$  and  $\sqrt{\frac{2}{4-\pi}} \sigma_n^2$ . To

assess the effectiveness of noise correction, the Full Width at Half Maximum (FWHM) and the median of the FA histogram were adopted.

### 2.2.3 Options of Signal Combination in Practice

The signals received in multichannel phase array coils must be combined before image reconstruction. The most commonly used method is the so-called sum-of-squares (SOS) method, which computes the pixel magnitude by the root-mean square average of the corresponding pixel values from each coil element. The advantage of this method is that the detailed coil element's sensitivity profiles are not required which in turn provides an easy and practical way of calculation and makes the reconstruction independent from the pulse sequence. With respect to SNR only, the SOS algorithm works best for high SNR. Furthermore, as no coil sensitivity profiles are used, artifacts arising from individual coil elements result in the same artifact in the final magnitude image (Larsson *et al.*, 2003).

Another option of signal combination is so called Adaptive Combine (AC) method. In this algorithm, the individual signals are combined using the pre-determined coil element sensitivity profile as coefficients. The advantage of this method is that it suppresses the noise floor and reduces the artifacts (e.g.: flow and motion artifacts in Cardiac MRI) (Walsh *et al.*,

2000). As there is no clear consensus, whether it is more important to keep a high SNR or to reduce the bias from possible artifacts, both signal combination methods have been examined in this study.

## 2.3 Phantom Experiments

In order to evaluate quantitatively measured diffusion parameters based on the DGV scheme in terms of anisotropy and fiber orientation and also verifying the actual effects of noise correction methods on clinical MR scanner, a dedicated synthetic phantoms with a well-structured and tight enough fiber bundle is preferable while confirming the simulation results with practical measurements.

### 2.3.1 Peripheral Nerve Phantom

Comparing the gradient schemes as demonstrated in **chapter 2.1.2.3** is not feasible in patients or volunteers, since the total acquisition time is too long. Therefore, a peripheral nerve phantom was used. This phantom was custom-made by HQ Imaging (HQ Imaging, Heidelberg, Germany) taking into account the tissue properties and morphology of human peripheral nerves. In this phantom, a straight bundle of parallel unwounded fiber filaments represents the peripheral nerve; this fiber bundle is immersed in water. Requirements to the fiber material were: high strength, light weight, ultra-hydrophobicity, and chemical inertness and impermeability to water. This would guarantee for reproducible measurements and low susceptibility differences to the surrounding water. Figure 2.6 shows the configuration of the phantom. The fiber strand in the center of the cylindrical phantom (rectangle, size approximately 15 mm x 20 mm,  $T_2=450\text{ms}$ ) is surrounded by a cylinder of silicone (diameter: 60mm) providing insulation and separation from the bright signal of the surrounding water, which fills the volume outside the silicone cylinder (diameter: 120mm, length: 200mm). Due to a high packing density of the polyester fibers (diameter 15 $\mu\text{m}$ ) a high FA (approximately 0.65) is reached.

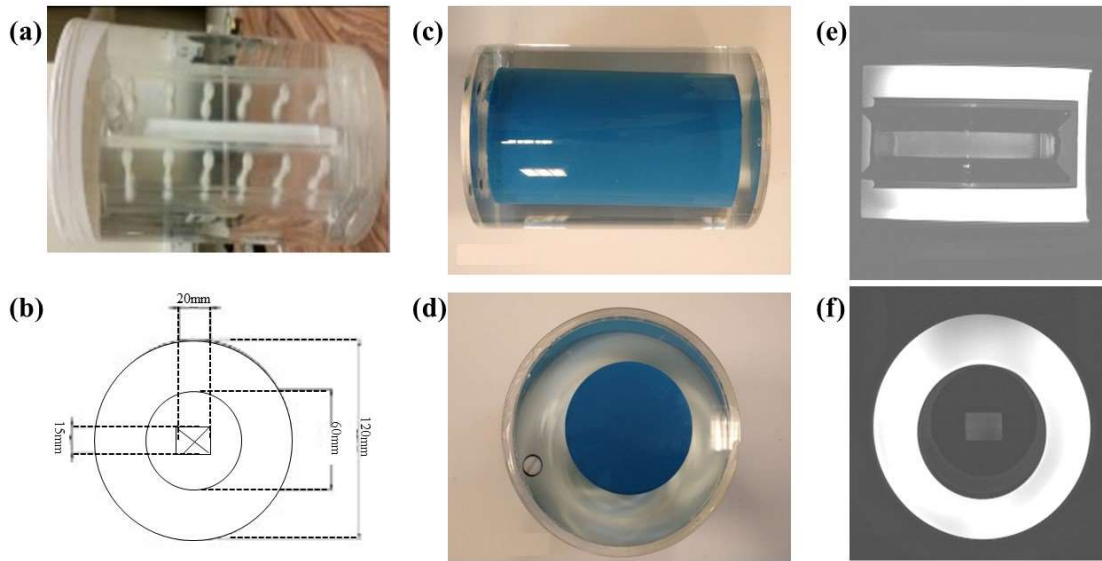


Figure 2.6: Phantom description: (a): Phantom without silicon surrounding. (b): Construction sketch. (c): finished phantom long axis view. (d): finished phantom crossing section view. (e): MRI of phantom in sagittal. (f): MRI of phantom in axial.

### 2.3.2 MR System and Protocol

Phantom measurements were performed at a 3T MRI system (TIM TRIO, Siemens Healthineers, Erlangen, Germany) with SYNGO software version VB19, using a 15-channel Transmit/Receive knee coil (Quality Electrodynamics 700 Beta Drive, Suite 100 Mayfield Village, OH 44143, USA. Distributed by SIEMENS).

After acquisition of scout sequences, DTI was performed as follows:

Diffusion sequence description:

- (1) For the SNR reference data (simulation of DGV), a diffusion-weighted spin-echo echo planar imaging (EPI) sequence was used with the sequence parameters: TR=4000ms; TE=100ms; slice thickness=5mm; orientation: transversal; slice number=1; matrix=128x128 with interpolation; Bandwidth (BW)=1502Hz/Pixel;  $b_0=0$  and  $b=1000 \text{ s/mm}^2$ ; no fat saturation; no parallel imaging; diffusion mode: multi-directional diffusion weighting (MDDW); diffusion directions: 6. For validation of the CN criteria on the selected DGV schemes, the diffusion mode was changed to 'free', which allows to use the respective DGV scheme.

- (2) To test the methods for noise correction, SNR was further decreased by changing the sequence protocol given above by reducing the slice thickness to 2mm and lowering the BW to 758Hz/Pixel. Diffusion mode was set to MDDW. The measurement was performed for different numbers of diffusion directions (N=6, 10, 20, 30); all measurements were repeated 100 times. The experiment was repeated 100 times.

### 2.3.3 Post-processing of Acquired MRI Data

- (1) To determine FA based on the phantom measurement the FA map was calculated using the evaluation tool of the SYNGO software (Siemens Healthineers, Erlangen, Germany). A region of interest comprised of 100 pixels was defined within the fiber strand of the phantom and copied to each FA map to ensure that FA was calculated at the same region for all experiments.
- (2) For testing the noise correction methods, FA was calculated as described in (1). Besides that, signal and noise were determined as shown in figure 2.7 for the image without and with diffusion weighting. From these data the signal intensities were corrected as follows:

Power image method:

$$S_k^2 = \langle M_k^2 \rangle - \langle n_k^2 \rangle$$

*Equation 2.32*

Factor methods:

$$S_k^2 = \left| \langle M_k \rangle^2 - \frac{2}{\pi} * \langle n_k \rangle^2 \right|$$

or

$$S_k^2 = \left| \langle M_k \rangle^2 - \frac{2}{4 - \pi} * std(n_k)^2 \right|$$

*Equation 2.33*

Where  $n_k$  denoted noise data set;  $M_k$  denoted measured data set;  $S_k$  denoted corrected signal input;  $N$  denoted gradient directions number ( $k=0,1,2,\dots,N$ ).

$\langle \rangle$  represented: mean value;  $\text{std}$  represented: standard deviation;  $|\ |$  represented: absolute.

After correction, FA was calculated on a pixel-by-pixel basis and the FA histograms were determined from a ROI inside the fiber strand.

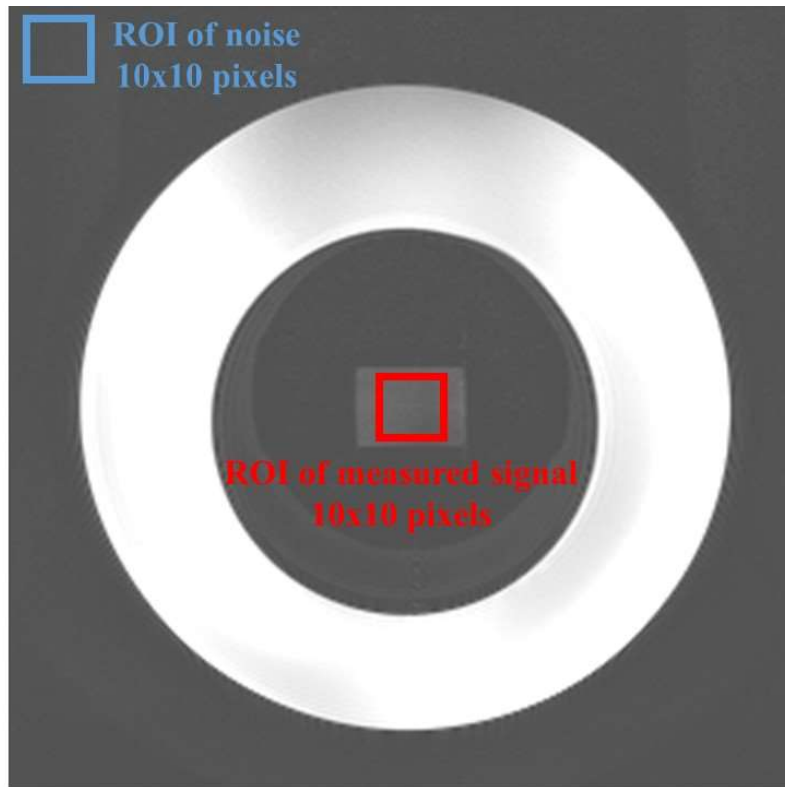


*Figure 2.7: Data sets extraction for the inputs of FA derivation in MATLAB program.*



## 3 RESULTS

### 3.1 Tailored Gradient Vectors Scheme

In a first step, the results of the optimization of the tailored DGV scheme is presented. Then in a second step – the optimized tailored DGV scheme is compared to other established DGV schemes.

#### 3.1.1 Coverage of the DGV scheme

The simulation results show that the deviation of the determined FA from the true FA values depends on the value of FA, the number of the diffusion vectors and the angle of the cone  $\Theta_{\max}$  (cf. figure 3.1-3.4).

For  $N=6$  and true  $FA=0.8$  the determined FA showed least deviation from the true FA for all  $\Theta_{\max}$ . In case of  $\Theta_{\max} > 30^\circ$ , the determined FA was within a 5% margin of the true FA value. For  $FA = 0.6$  and  $FA=0.8$  the deviation was higher than 5% even for full coverage of the diffusion direction sphere, i.e. for  $\Theta_{\max}=180^\circ$  (cf. figure 3.1); FA was overestimated. The higher the number of diffusion gradients, the higher the accuracy of the determined FA. The maximum cone angle necessary to guarantee that FA is within an error margin of 5% from the true FA, depended on the number of diffusion directions and on the true FA. For  $N=10$ , the 5% error margin criterion was reached for  $\Theta_{\max}=30^\circ$  ( $FA=0.8$ ), for  $\Theta_{\max}=45^\circ$  ( $FA=0.6$ ), and for  $\Theta_{\max}=60^\circ$  ( $FA=0.4$ ), cf. figure 3.2. For  $N=20$ , FA was within the 5% error margin from  $\Theta_{\max}=30^\circ$  ( $FA=0.8$ ), and from  $\Theta_{\max}=45^\circ$  ( $FA=0.6$  and  $0.4$ ), cf. figure 3.3. For  $N=30$ , the 5% error margin criterion was reached for  $\Theta_{\max}=30^\circ$  ( $FA=0.8$  and  $0.6$ ), and for  $\Theta_{\max}=45^\circ$  ( $FA=0.4$ ), cf. figure 3.4.

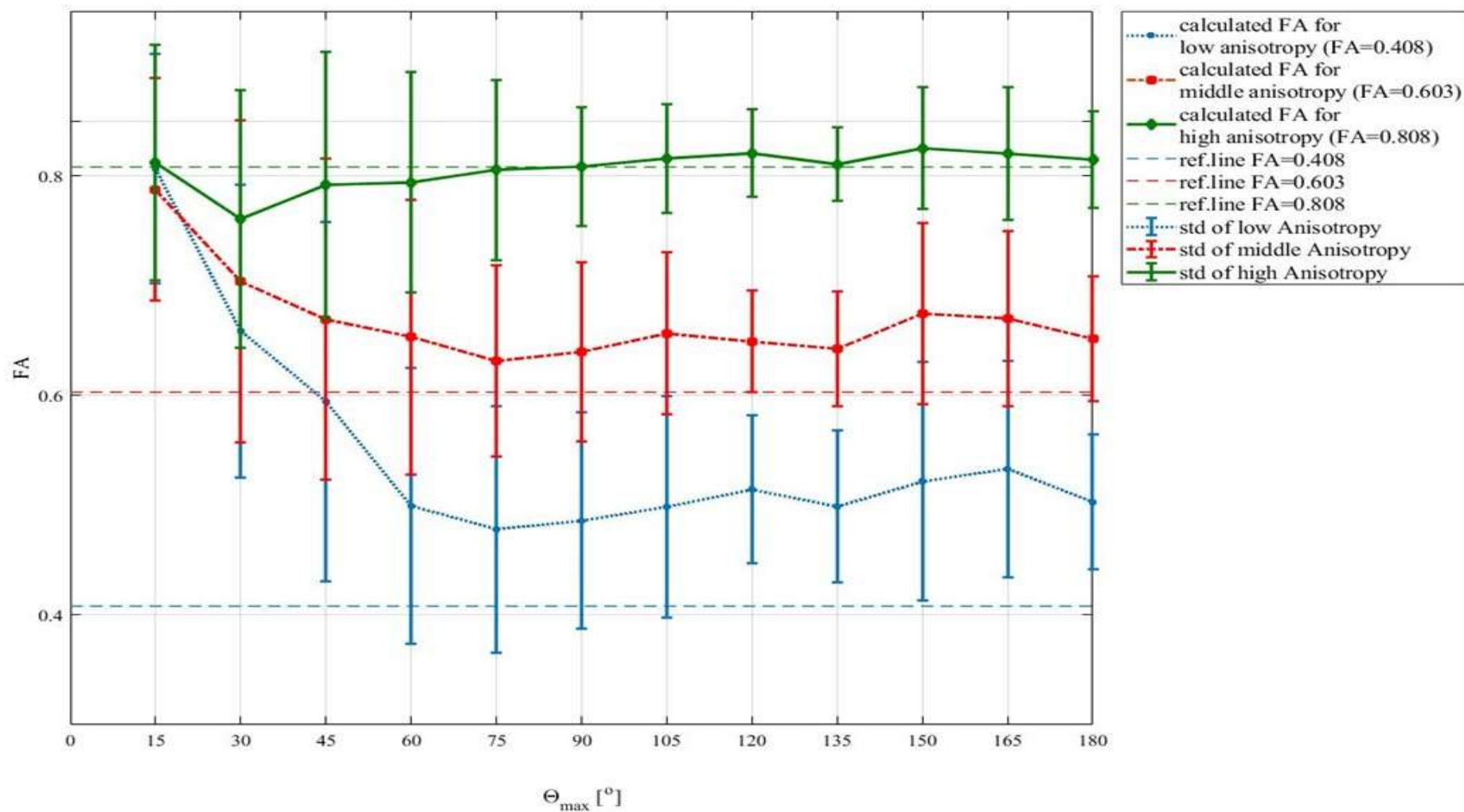


Figure 3.1: Result of the simulation for DGV with  $N=6$  and different coverage ( $\Theta_{max}$ ) The symbols (circles, squares, diamonds) mark the simulated results, the dashed lines in the same color mark the theoretical value of FA that was used as input for the simulation and the corresponding mean and standard deviation of 10,000 times simulated FA display below the dashed lines.

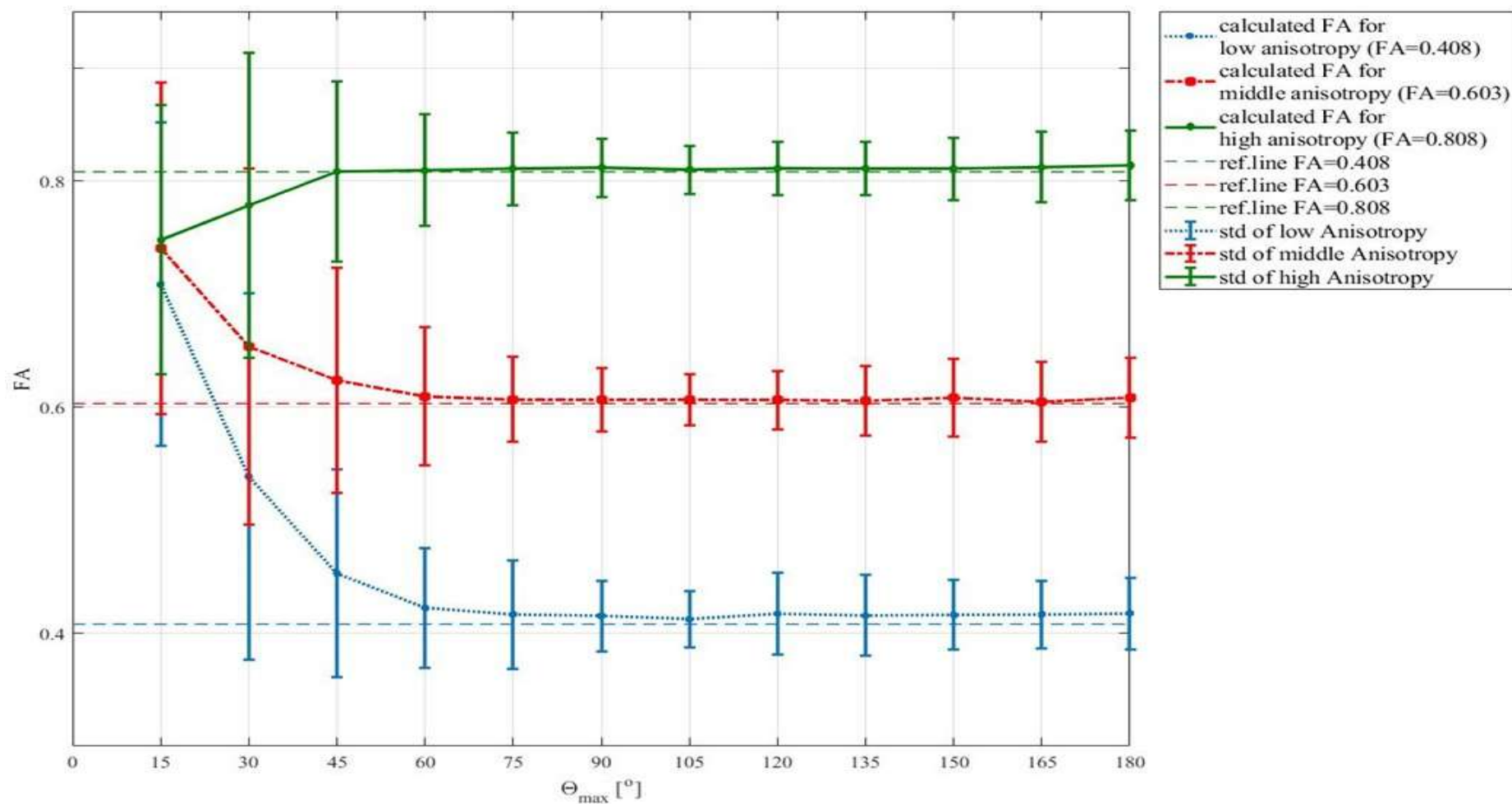


Figure 3.2: Result of the simulation for DGV with  $N=10$  and different coverage ( $\Theta_{max}$ ). The symbols (circles, squares, diamonds) mark the simulated results, the dashed lines in the same color mark the theoretical value of FA that was used as input for the simulation and the corresponding mean and standard deviation of 10,000 times simulated FA display below the dashed lines.

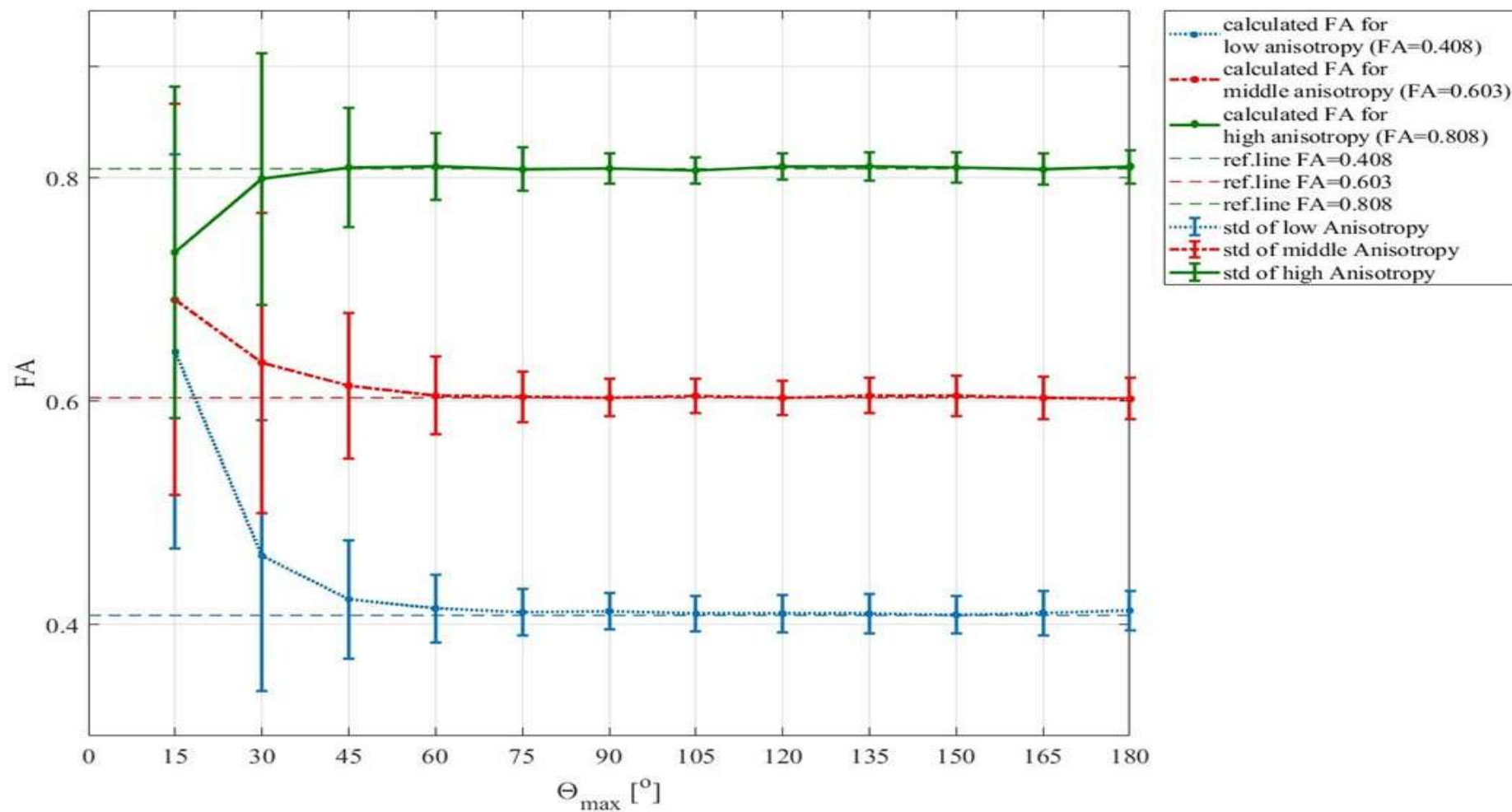


Figure 3.3: Result of the simulation for DGV with  $N=20$  and different coverage ( $\Theta_{max}$ ). The symbols (circles, squares, diamonds) mark the simulated results, the dashed lines in the same color mark the theoretical value of FA that was used as input for the simulation and the corresponding mean and standard deviation of 10,000 times simulated FA display below the dashed lines.

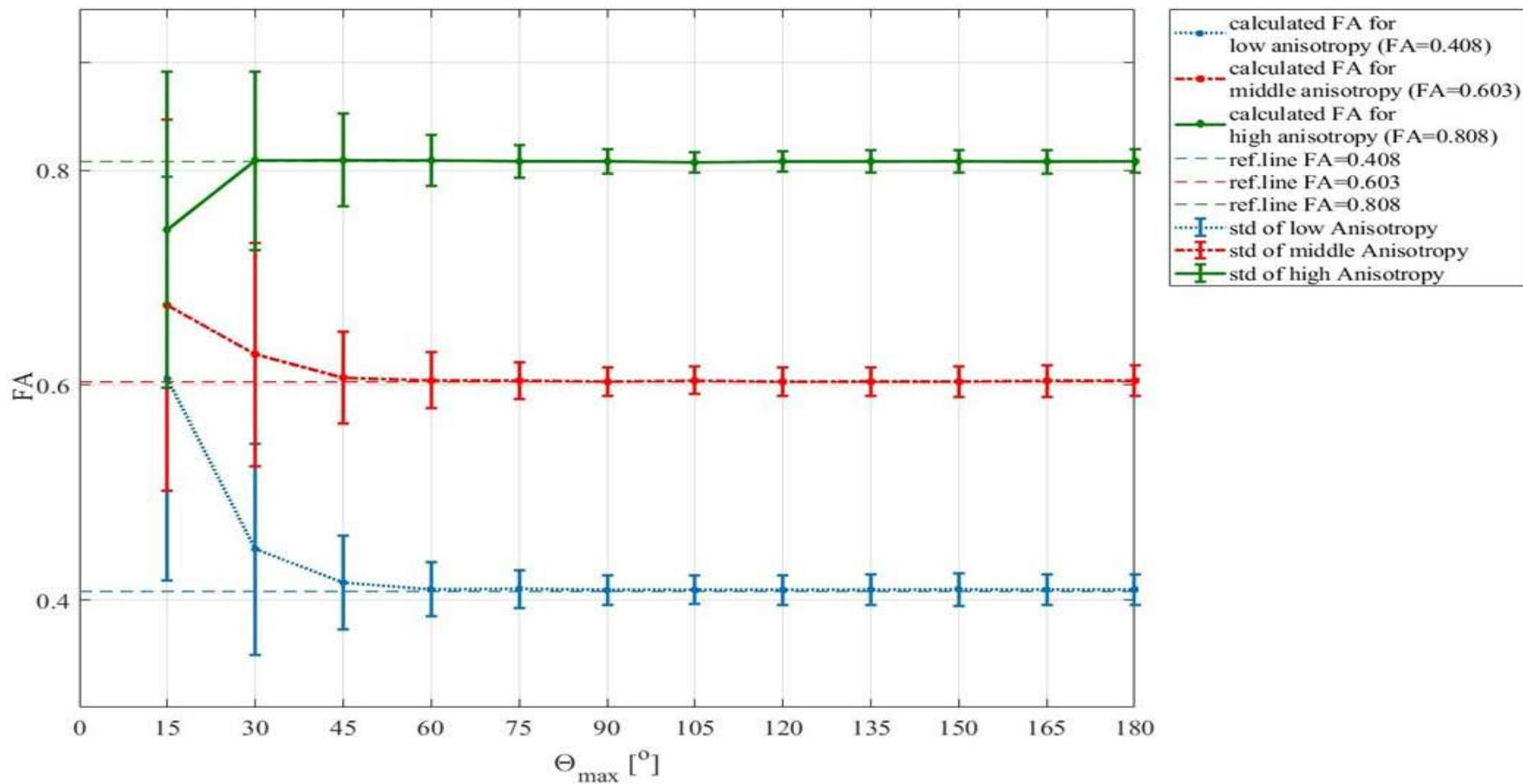


Figure 3.4: Result of the simulation for DGV with  $N=30$  and different coverage ( $\Theta_{max}$ ). The symbols (circles, squares, diamonds) mark the simulated results, the dashed lines in the same color mark the theoretical value of FA that was used as input for the simulation and the corresponding mean and standard deviation of 10,000 times simulated FA display below the dashed lines.

### 3.1.2 Finding the Optimum DGV

In order to single out the optimum DGV schemes for each anisotropy level, the schemes that showed the lowest deviation from the expected FA were analyzed by calculation of CN for each  $N$  and  $\Theta_{\max}$ . CN showed a distinct decrease for low  $\Theta_{\max}$  with a minimum CN between  $\Theta_{\max}=90^\circ$  and  $120^\circ$ . For  $\Theta_{\max}>120^\circ$  CN increased slightly.

The dependency of CN from  $\Theta_{\max}$  did not vary significantly between  $N=10, 20$  and  $30$ . There was, however, a more undulating curve for CN ( $\Theta_{\max}$ ) for  $\Theta_{\max}>90^\circ$  (see figure 3.5).

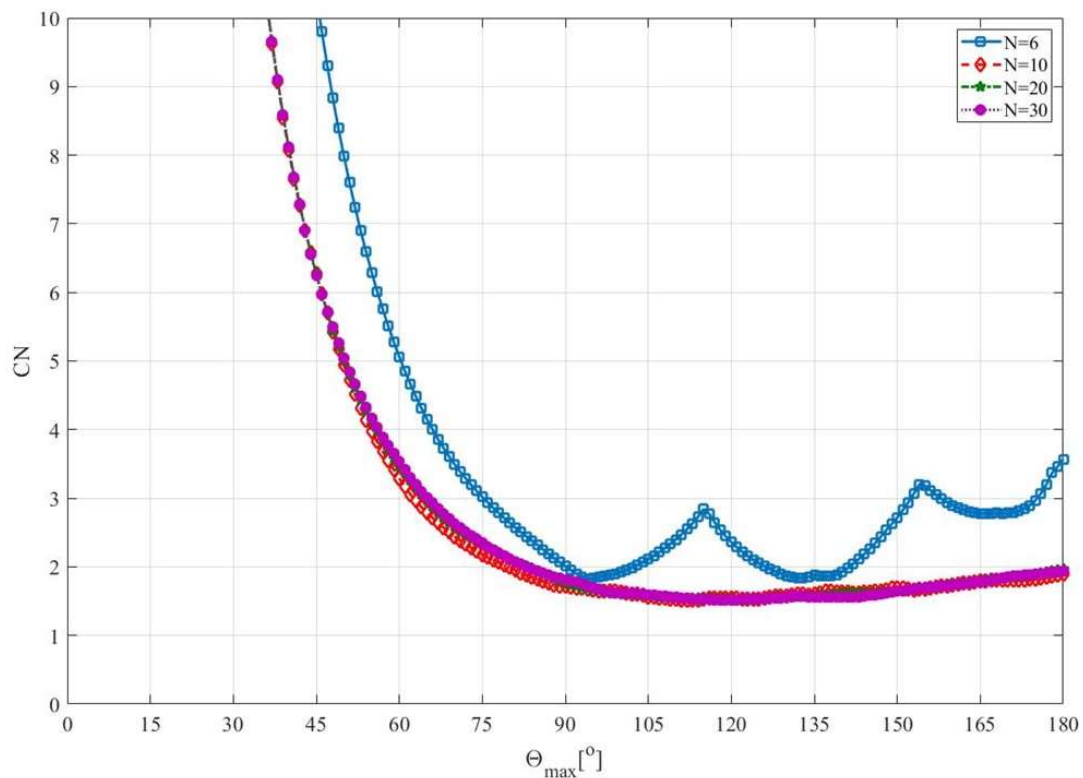


Figure 3.5: Condition Number CN as function of  $\Theta_{\max}$  and  $N$ , which are calculated from the premium DGV for each  $\Theta_{\max}$  by means of lowest deviation from the expected FA. In the figure, CN was calculated for  $\Theta_{\max}$  between  $15^\circ$  and  $180^\circ$  in steps of  $1^\circ$  and only the DGVs with  $CN < 10$  are displayed for sake of clarity.

### 3.1.3 Validation of simulation results in Phantom study

In addition to calculation of the condition numbers the phantom experiments were performed with the optimum DGV found in **chapter 3.1.2**. In these experiments, FA was calculated from the measurements for different  $\Theta_{\max}$  and  $N$ . Figure 3.6 shows the results: For all  $N$ , FA is overestimated for  $\Theta_{\max}=15^\circ$ , while there is a slight underestimation of FA for  $\Theta_{\max}=45^\circ$  and  $60^\circ$  for  $N>6$ . From  $\Theta_{\max}>75^\circ$ , there is no significant difference between the calculated FA and the real FA (0.65). Interestingly, the underestimation of FA for  $\Theta_{\max}=45^\circ$  and  $60^\circ$  could not be shown in the simulation study (**chapter 3.1.1**).

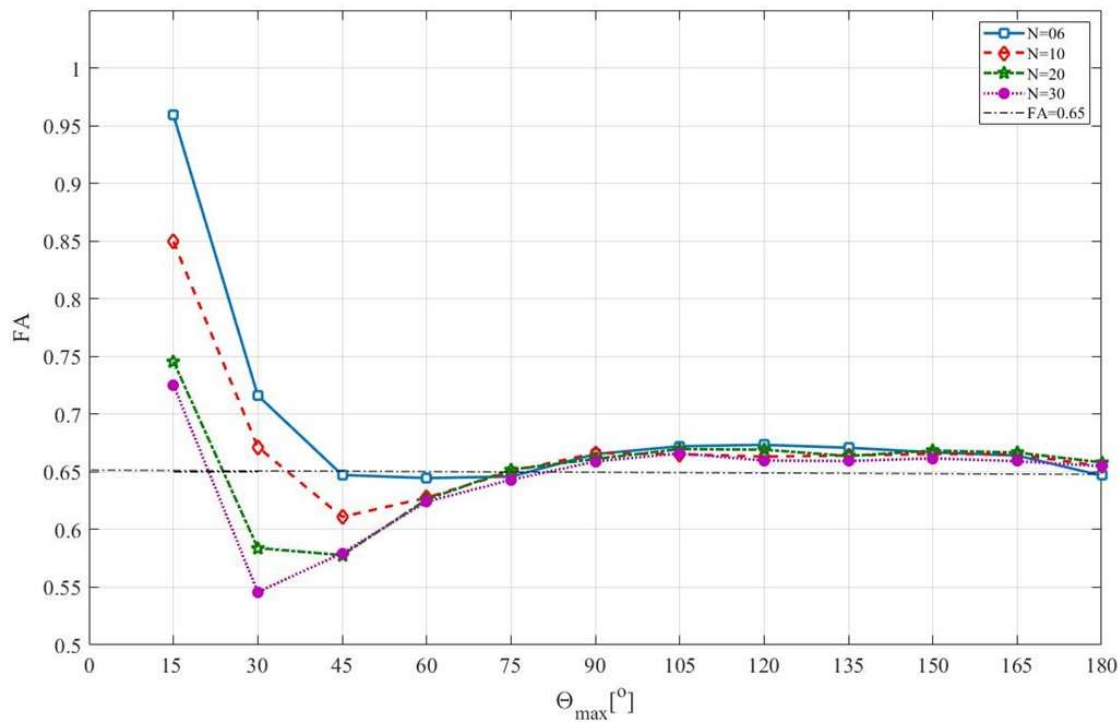


Figure 3.6: FA determined from the phantom experiments for different  $N$  and  $\Theta_{\max}$ .

Based on the minimization of CN, the optimum DGV schemes for N=6, 10, 20 and 30 were selected as shown in table 3.1.

Table 3.1: Final Optimal DGV Schemes

N=6 (CN=1.82)			N=20 (CN=1.50)			N=30 (CN=1.53)		
$g_x$	$g_y$	$g_z$	$g_x$	$g_y$	$g_z$	$g_x$	$g_y$	$g_z$
0.4988	0.8639	-0.0698	0.9456	0.3072	0.1071	0.9743	0.2071	-0.0883
-0.3657	0.6334	0.6820	0.6819	0.4955	-0.5380	0.8714	0.3880	-0.3002
-0.9793	0.0000	0.2022	0.2558	0.3521	0.9003	0.7143	0.5190	0.4695
-0.1350	-0.2339	0.9628	0.3016	0.9282	0.2181	0.1904	0.2115	0.9587
0.4442	-0.7693	0.4592	0.0000	0.7837	0.6211	0.4336	0.7510	-0.4980
0.5200	0.0000	0.8542	-0.2775	0.8541	-0.4399	0.1091	0.3357	0.9356
			-0.0660	0.0909	0.9937	0.0984	0.9361	0.3376
			-0.6865	0.4987	0.5292	-0.0843	0.8019	0.5915
			-0.6743	0.2191	0.7053	-0.3090	0.9509	-0.0163
			-0.9736	0.0000	-0.2284	-0.2097	0.3633	0.9078
			-0.7391	-0.2402	-0.6293	-0.3237	0.3595	0.8752
			-0.2681	-0.1948	0.9435	-0.1737	0.1262	0.9767
			-0.3137	-0.4317	0.8457	-0.9061	0.4034	0.1276
			-0.2921	-0.8990	0.3264	-0.7449	0.1583	0.6481
			0.0000	-1.0000	-0.0052	-0.8290	0.0000	-0.5592
			0.2910	-0.8957	-0.3363	-0.9095	-0.1933	-0.3681
			0.3675	-0.5058	0.7804	-0.6512	-0.2899	0.7013
			0.7302	-0.5305	0.4305	-0.1163	-0.0845	0.9896
			0.2123	-0.0690	0.9748	-0.3651	-0.4055	0.8380
			0.9931	0.0000	-0.1175	-0.0360	-0.0624	0.9974
						-0.2784	-0.8567	-0.4342
						-0.1024	-0.9747	0.1988
						0.1007	-0.9579	0.2689
						0.2826	-0.8697	0.4046
						0.3023	-0.5236	0.7965
						0.6605	-0.7336	-0.1599
						0.5343	-0.3882	0.7509
						0.7736	-0.3444	0.5319
						0.9766	-0.2076	0.0558
						0.9730	0.0000	-0.2306



### 3.1.4 Comparison with Established Gradient Schemes

In a final step, we compared the final optimized DGV schemes for different  $N$  (see **chapter 3.1.3**) with other gradient schemes developed for applications outside peripheral nerve imaging: The standard gradient scheme of the manufacturer (SIEMENS), Jones' optimal schemes (Jones, 2004) and the schemes found by Downhill Simplex Minimization (DSM) (Skare *et al.*, 2000a). For this comparison, we performed simulations according to the simulations described in **chapter 2.1.2.3**, and also calculated CN of the respective schemes.

The results of these simulations/calculations are given in figure 3.7. They show that for high  $N$ , the DSM scheme produces the lowest condition number, followed by the DGV scheme developed in this project. The standard gradient scheme of the manufacturer (SIEMENS) and the Jones scheme show higher systematic errors compared to DGV and DSM. For  $N=6$ , the Jones scheme is superior to the DGV and SIEMENS scheme.

With respect to the standard deviation of FA, the SIEMENS and Jones scheme are superior to DSM and DGV. This difference, however, decreases with the number of gradients. For  $N>20$  standard deviation of FA is comparable for all schemes.

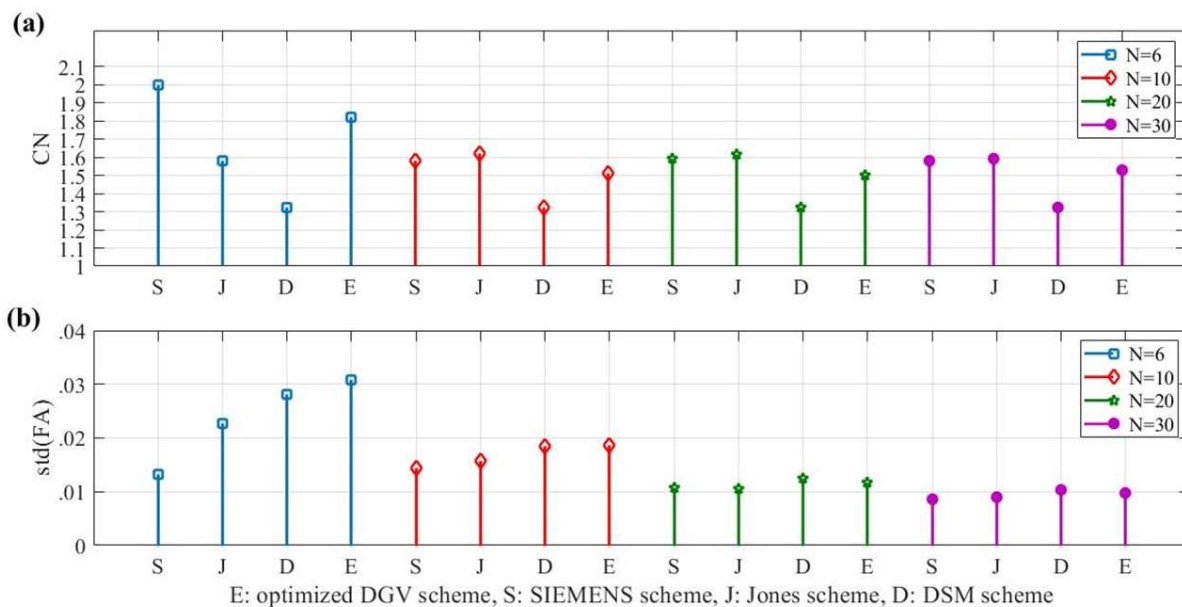
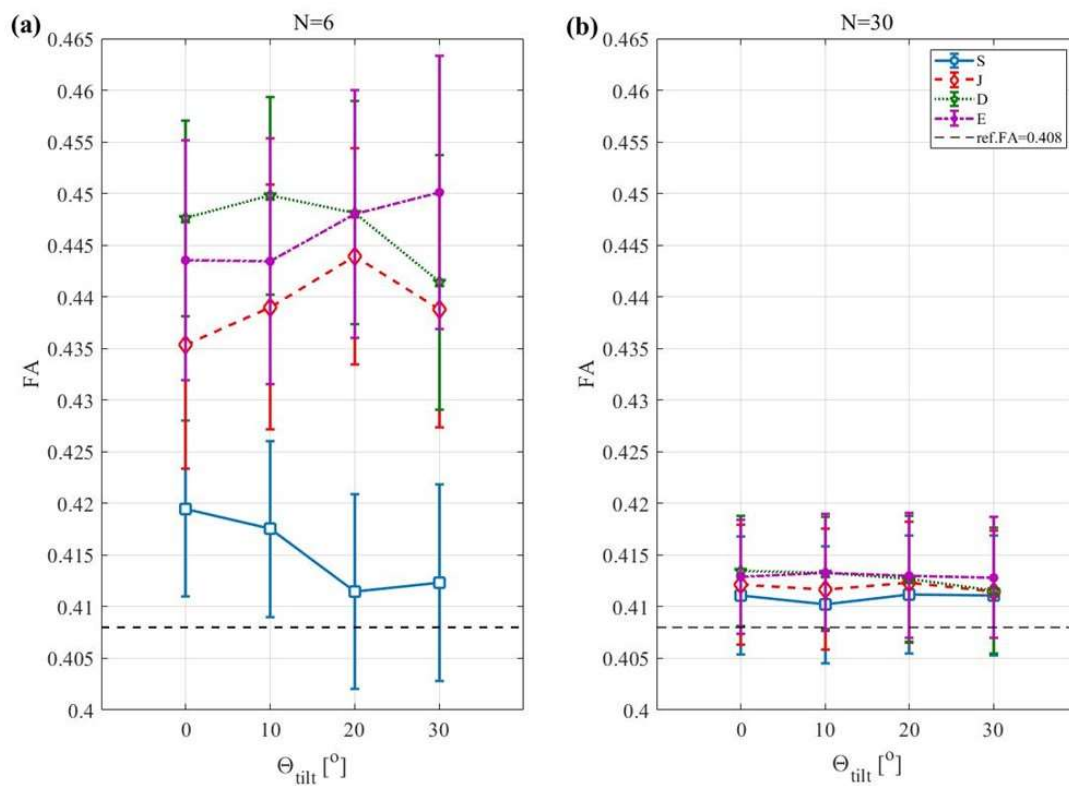


Figure 3.7: Comparison of the optimum Directional Gradient Vector schemes with other optimized gradient vector schemes for different number of gradients,  $N$ : (a) Condition number. (b) Standard deviation of FA.

In a final step, we tested the susceptibility of all schemes with regards to small deviations of the nerve axis from the z-axis (scanner axis). This is important, because the general concept of DGV is based on the fact that even for the peripheral nerves there are slight variations in alignment with regard to the body (and scanner) axis.

The results (figure 3.8) show that all schemes except the SIEMENS scheme produce consistent results even for an angle of  $30^\circ$  between nerve and z-axis. The SIEMENS scheme, however, underestimates the FA for low N ( $N=6$ ), if the tilting angle between nerve and z-axis exceeds 10 degrees.



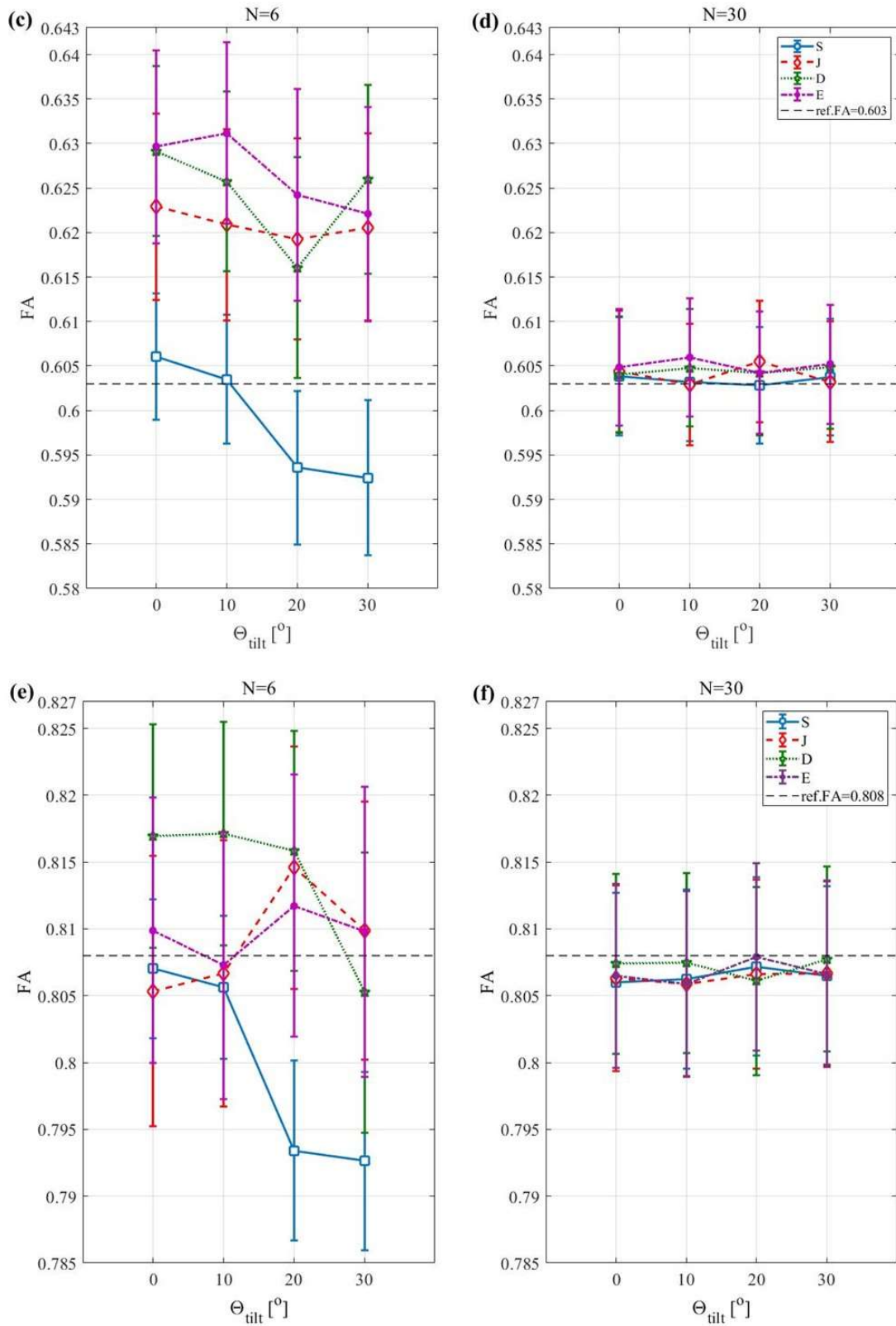


Figure 3.8: Simulation results of Fractional Anisotropy (FA) for  $N=6$  and  $N=30$  for different tilting angles of the nerve structure with respect to the z-axis ( $\Theta_{\text{tilt}}$ ). E: optimized DGV scheme, S: SIEMENS scheme, J: Jones scheme, D: DSM scheme.

### 3.2 Noise Correction

In simplest case of a one channel receiving coil, the MRI image is reconstructed by Fourier transform as magnitude image from received complex signal. In this case, the background noise follows a Rayleigh distribution. Nowadays multichannel phase array receiving coils allow for a faster data acquisition with higher SNR. At the same time, statistical distribution of image noise is affected by the signal combination. In this case, the conventional practice to calculate SNR using the signal mean value and the standard deviation of a background ROI will lead to inaccurate estimations of the true SNR (Dietrich *et al.*, 2007).

In this study, the different performances of the noise correction methods presented in **chapter 2.2.2** was examined in a simulation study and in a phantom scanning experiment for different coil combination algorithms.

#### 3.2.2 Noise propagation correction

To evaluate the efficacy of the noise correction methods, these methods were applied to the simulated DTI data. After correction, FA was calculated. Figure 3.9 shows the FA histograms derived from the DTI data without and with noise correction. A distinct underestimation of the pre-defined FA value was found, due to the noise bias (Damon, 2008; Dietrich *et al.*, 2001; Jones and Basser, 2004). Without correction, the median FA ( $FA_{\text{median}}$ ) was 0.583 instead of the pre-defined FA=0.603. Furthermore, the high FWHM (0.050 without correction) reveals a high uncertainty of the calculated FA. FWHM is 0.050 without correction. Both power images correction and the correction factor method (correction factor: power of deviation from background noise value) lead to a significant decrease of FWHM (power images: FWHM=0.006, correction factor: FWHM=0.010) and to a shift of the median FA toward the real FA (power images:  $FA_{\text{median}}$ =0.603, correction factor:  $FA_{\text{median}}$ =0.605).

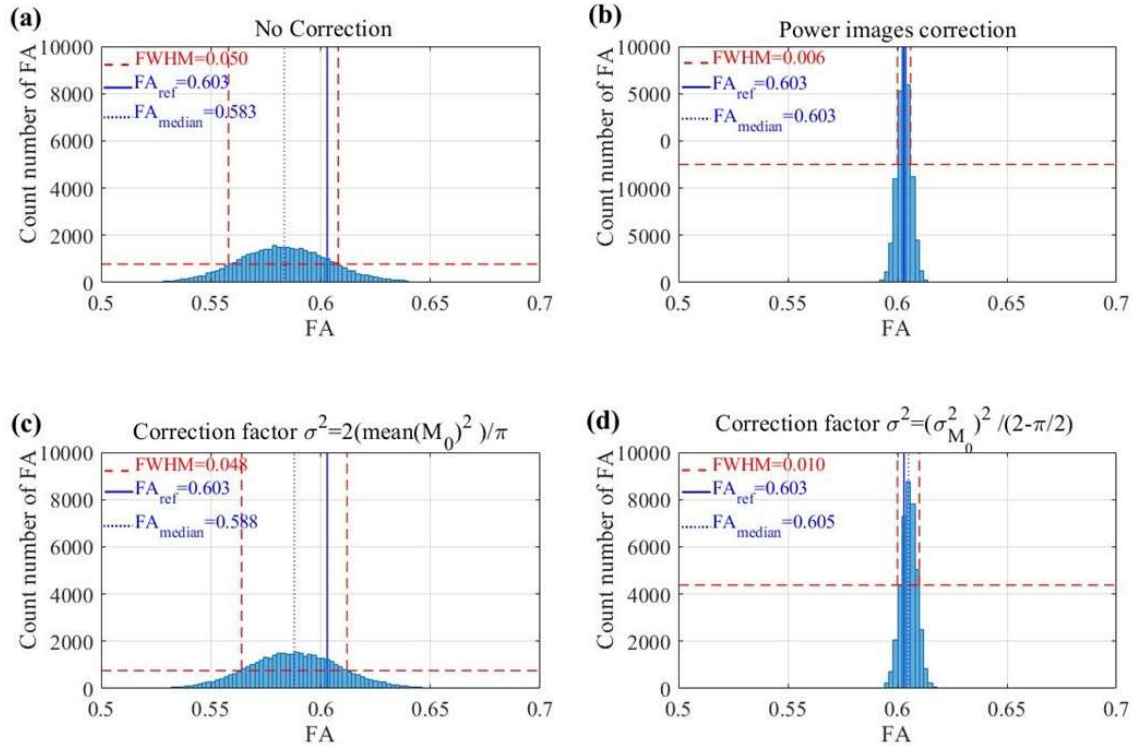


Figure 3.9: Efficacy of different noise correction methods: the simulation study (a) FA without noise correction. (b) FA with power images correction method. (c) FA with correction factor by mean of noise values. (d) FA with correction factor by power of deviation from noise values. The solid blue line marks the pre-defined FA, the dotted blue line marks the median FA of the simulated data and the dashed red line FWHM.

In order to verify the results of the simulation study, a phantom study was performed as described in **chapter 2.3.2**. Different from the simulation study, there is no absolute certainty about the ground truth of FA. Therefore, when testing the efficacy of the correction methods, we had to rely on the assumption that the FA value given by the phantom manufacturer  $FA=0.65$  is the true value. Furthermore, due to time restriction, the measurements were repeated 100 times instead of 10000 times as done in the simulation study.

Figure 3.10 displays the FA histograms derived from the phantom study. It confirmed that FA is underestimated without noise correction:  $FA_{\text{median}}$  was 0.595 instead of the reference  $FA=0.65$ . Furthermore, the phantom study revealed a FWHM (FWHM=0.04) comparable to that of the simulation study (FWHM=0.05) which shows in turn that the noise level in the simulation study was chosen appropriately. The power images correction method lead to an increase of  $FA_{\text{median}}$  to 0.65, i.e. produced exactly the FA value specified by the manufacturer. Also FWHM was reduced considerably to 0.02. The correction factor method (correction factor:

mean of noise) performed better than in the simulation study: FA was shifted toward the reference FA ( $FA_{\text{median}}=0.626$ ), and FWHM was reduced (FWHM=0.03). The correction factor method (correction factor: power of deviation) in turn performed less well than in the simulation study: Although FA was shifted towards the reference value ( $FA_{\text{median}}=0.620$ ), FWHM was not reduced (FWHM=0.04) and the histogram showed a double peak in contrast to the histogram of the uncorrected data and the histograms of the other correction methods.

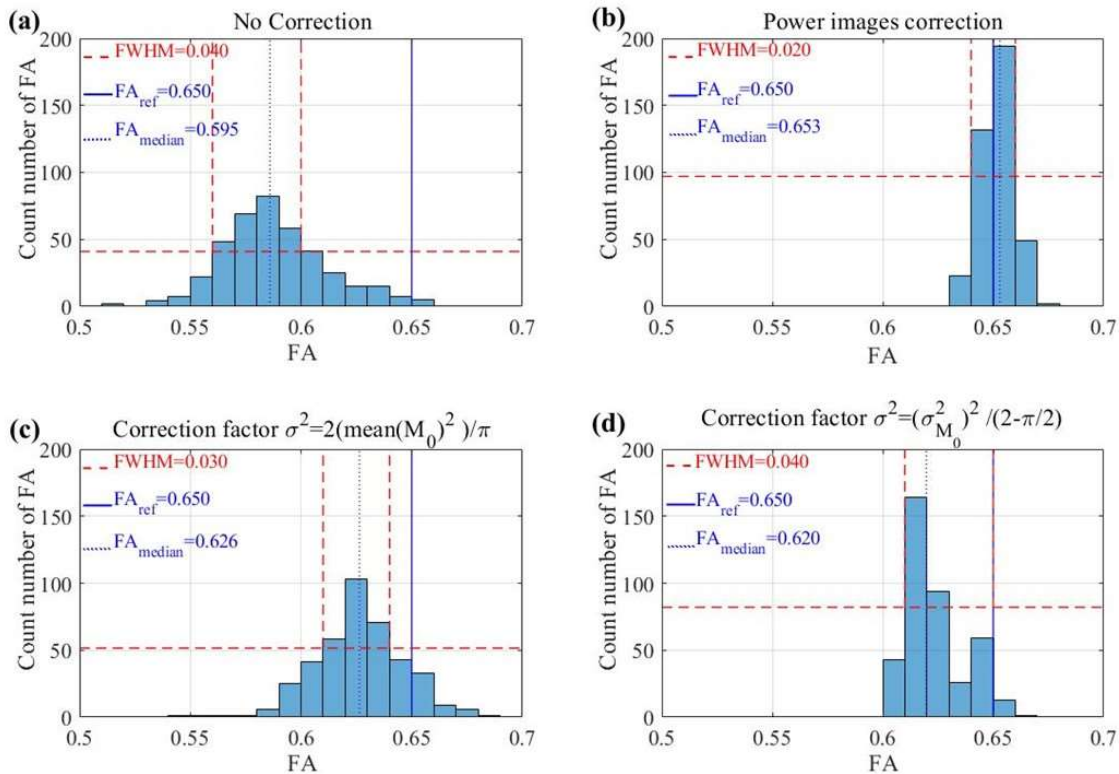


Figure 3.10: Efficacy of different noise correction methods: the phantom measurements results with coil combination by Sum-Of-Squares (SOS). (a) FA without noise correction. (b) FA with power images correction method. (c) FA with correction factor by mean of noise values. (d) FA with correction factor by power of deviation from noise values. The solid blue line marks the FA specified by the manufacturer, the dotted blue line marks the median FA of the simulated data and the dashed red line marks the FWHM.

Figure 3.11 shows the histograms of signal and noise for SOS signal combination for different number of diffusion gradients. While the level of signal from  $b=0$  and the noise level stay constant for all numbers of diffusion gradients, the diffusion weighted signal in the measurements for  $N \geq 10$  is lower than the diffusion weighted signal for  $N=6$ . This leads to an underestimation of FA for  $N \geq 10$  after noise correction. Combination of all data from  $N=6, 10, 20$  and  $30$ , in turn, lead to the double peak found in Figure 3.10(d).

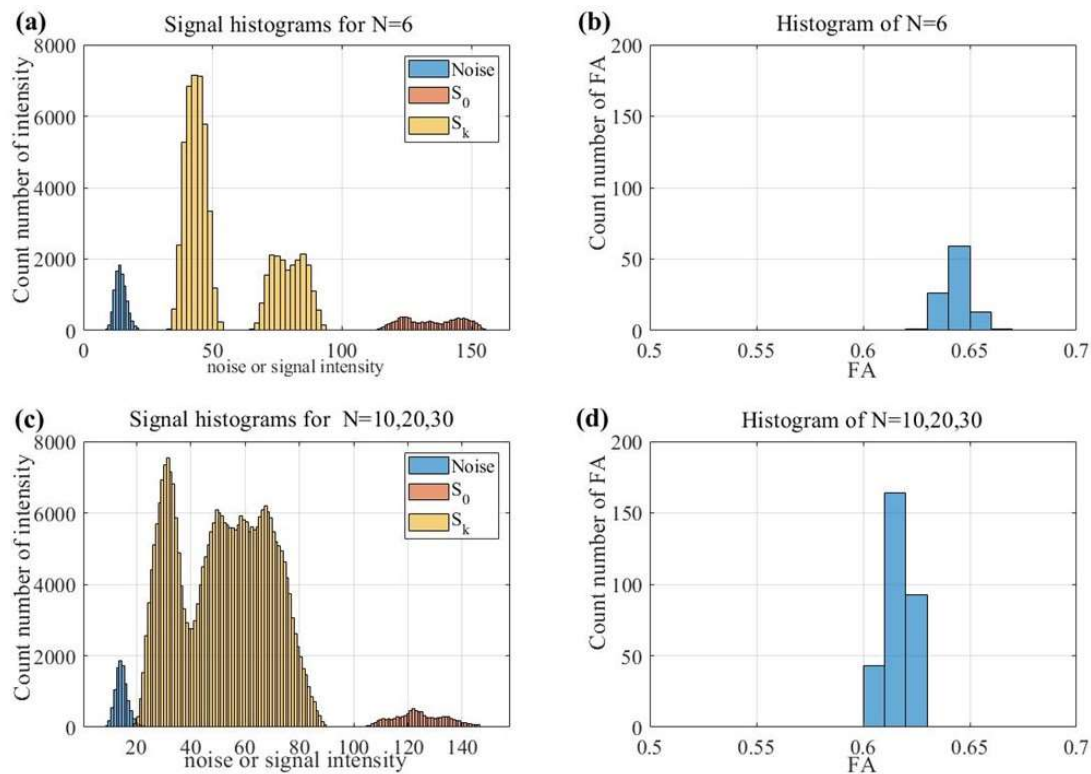


Figure 3.11: Phantom measurement with coil combination by Sum-Of-Squares (SOS). (a): histograms of noise and signal intensity for  $b=0$  and  $1000s/mm^2$  for  $N=6$ . (b): histogram of corrected FAs by the correction factor method with power of noise deviation. (c): histograms of noise and signal intensity for  $b=0$  and  $1000s/mm^2$  for  $N=10, 20$  and  $30$ . (d): Assembled histogram of corrected FA by the correction factor method with power of noise deviation.

The noise floor is expected to be lower when using the Adaptive Combine algorithm for coil combination compared to the noise floor when using SOS. Figure 3.12 shows the FA histogram derived from phantom scanning data sets with the AC coil combination. Without noise correction, the median FA (0.616) is closer to the reference FA (0.650) than the uncorrected FA with SOS signal combination (0.595). The FWHM for the uncorrected FA based on AC signal combination, however, is even higher (0.050) than that based on SOS (0.040). The correction factor method (mean of noise values) lead to a shift of the median FA towards the reference FA without resulting in a decreased FWHM. In contrast to this method, the power image method and the correction factor method (power of deviation) showed equally good results with a shift of the median FA (0.654) to the reference FA (0.650) and narrowing down the FWHM to 0.020. The AC signal combination eliminated the double peaks in the factor correction method (power of noise deviation) that was seen in the SOS signal combination method.

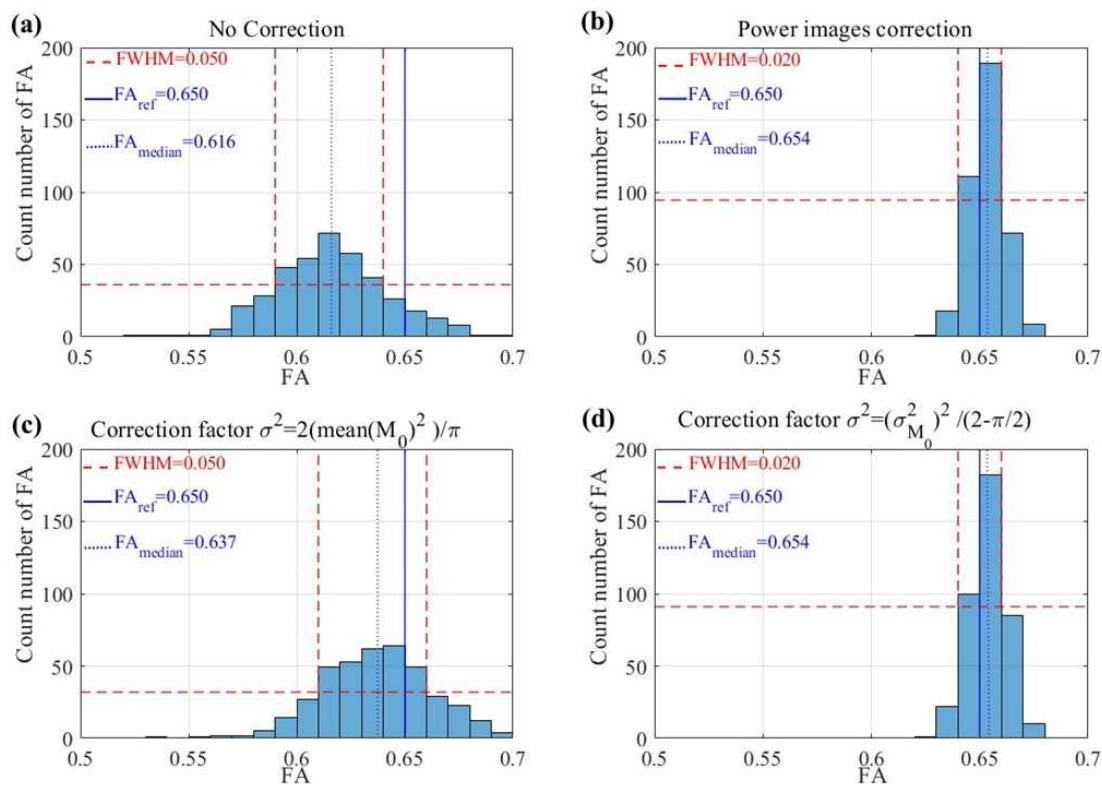


Figure 3.12: Efficacy of different noise correction methods: the phantom measurements results with coil combination by Adaptive Combine (AC). (a) FA without noise correction. (b) FA with power images correction method. (c) FA with correction factor by mean of noise values. (d) FA with correction factor by power of deviation from noise values. The solid blue line marks the FA specified by the manufacturer, the dotted blue line marks the median FA of the simulated data and the dashed red line marks the FWHM.



To examine the influence of the noise floor upon FA calculation for AC coil combination, histograms of signal and noise and histograms of FA were examined for different numbers of gradient directions. Figure 3.13 shows the respective histograms. In contrast to SOS coil combination (figure 3.11), the histograms of signal and noise based on AC coil combination follow Rayleigh distribution; furthermore the histogram maxima for noise,  $S_0$  and  $S_k$  are comparable for all numbers of diffusion directions. As a result of this distribution, the FA histograms for  $N=6$  and  $N \geq 10$  are centered around the same FA value.

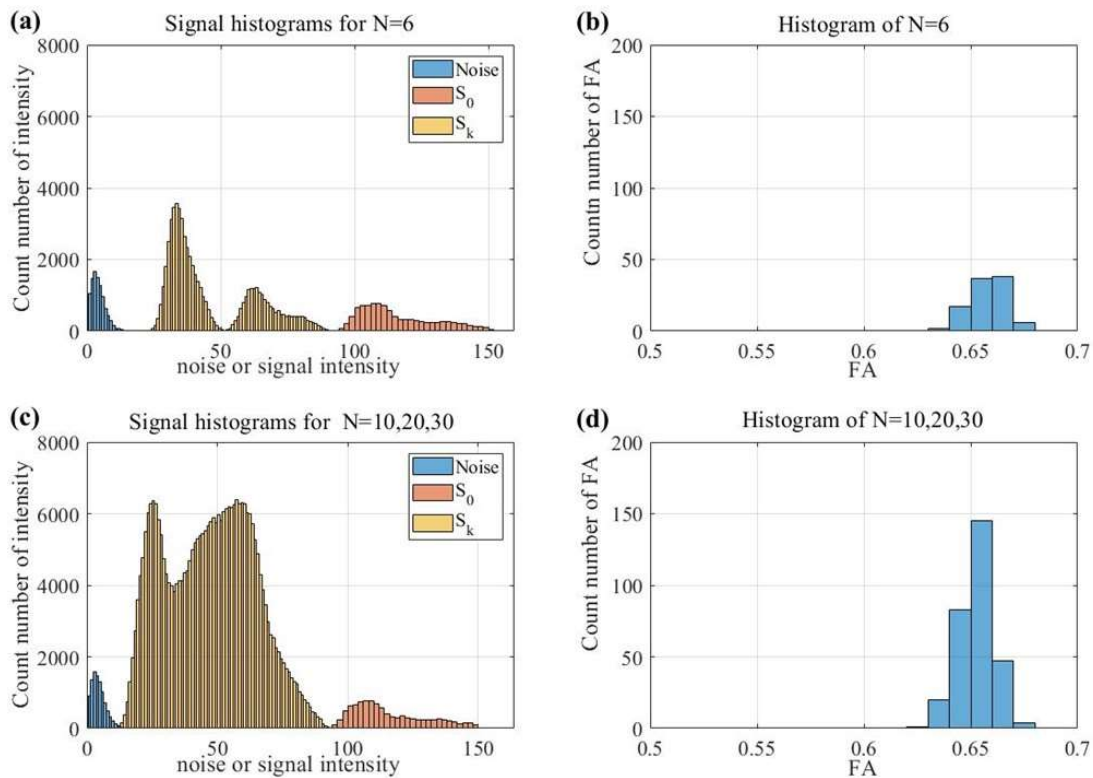


Figure 3.13: Phantom measurement with coil combination by Adaptive Combine (AC). (a): histograms of noise and signal intensity for  $b=0$  and  $1000s/mm^2$  for  $N=6$ . (b): histogram of corrected FAs by the correction factor method with power of noise deviation. (c): histograms of noise and signal intensity for  $b=0$  and  $1000s/mm^2$  for  $N=10, 20$  and  $30$ . (d): Assembled histogram of corrected FA by the correction factor method with power of noise deviation.

To focus on the pure effects of correction methods without influence of the number of diffusion gradient directions, the simulation data for  $N=30$  are separately displayed in figure 3.14. Best results regarding median FA and FWHM were achieved by the power image correction method, directly followed by the correction factor method (using power of noise deviation). The correction factor method (using mean of noise values) in turn did not result in any improvement compared to the original distribution.

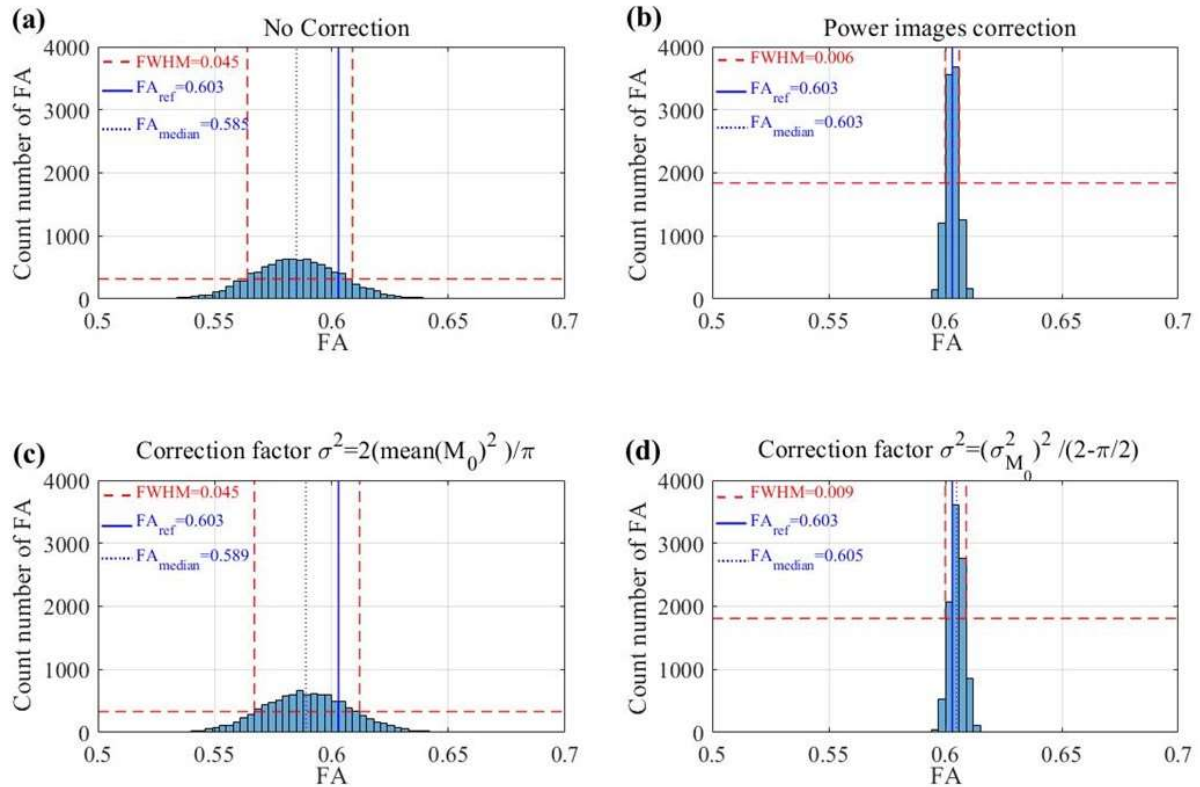


Figure 3.14: Efficacy of different noise correction methods: the simulation study results with  $N=30$ . (a) FA without noise correction. (b) FA with power images correction method. (c) FA with correction factor by mean of noise values. (d) FA with correction factor by power of deviation from noise values. The solid blue line marks the pre-defined FA, the dotted blue line marks the median FA of the simulated data and the dashed red line FWHM.

When comparing the correction methods in phantom experiments (figure 3.15), however, the performance of the methods is different to that of the simulation study. The correction method using power images performed best with consistently good results for both methods of coil combination. The correction factor method (using power of deviation) did only perform well for AC coil combination but did fail for SOS coil combination. The correction factor method (using mean of noise values) enabled a shift of the FA median towards the reference FA; this method, however, failed to reduce FWHM.

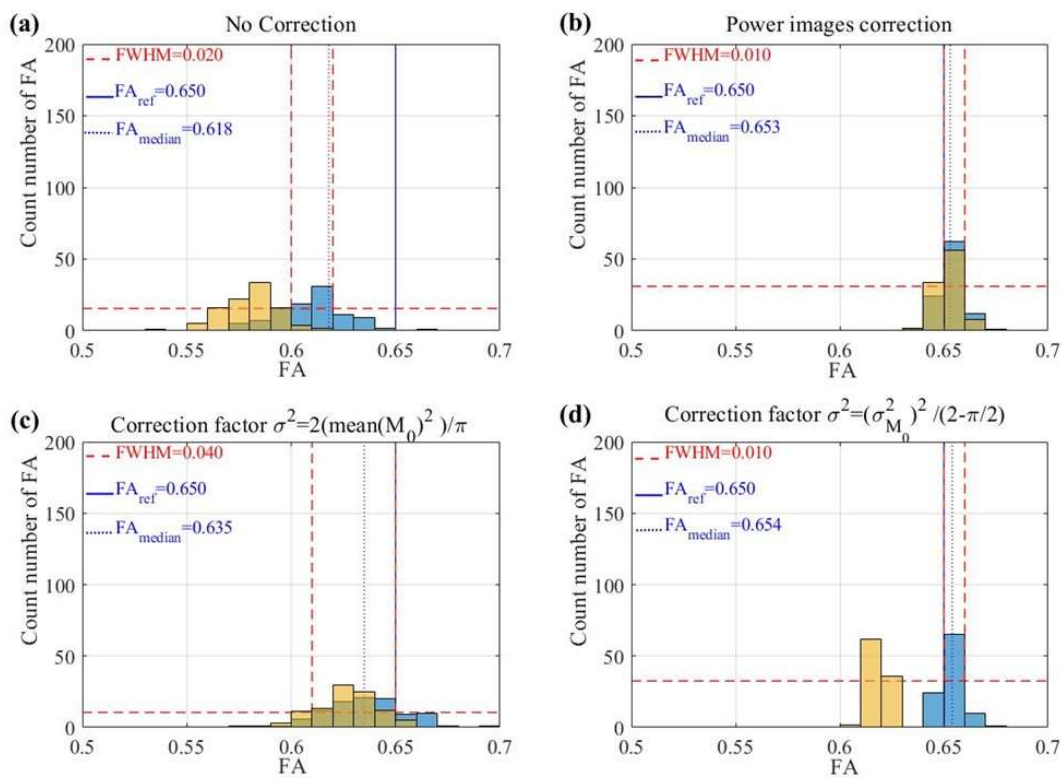


Figure 3.15: Efficacy of different noise correction methods: the phantom measurements results with  $N=30$ . The blue histograms originate from coil combination by AC and the yellow histograms originate from coil combination by SOS. (a) FA without noise correction. (b) FA with power images correction method. (c) FA with correction factor by mean of noise values. (d) FA with correction factor by power of deviation from noise values. The solid blue line marks the FA specified by the manufacturer, the dotted blue line marks the median FA of the simulated data and the dashed red line marks the FWHM.

Comparison of the noise pattern in simulation and in the phantom study (figure 3.16) showed that noise followed Rayleigh distribution for  $b=0$  and  $1000 \text{ s/mm}^2$  in simulation and in the phantom experiment. Deviation from the Rayleigh curve in the phantom experiment at  $b=0$  resulted from low number of pixels.

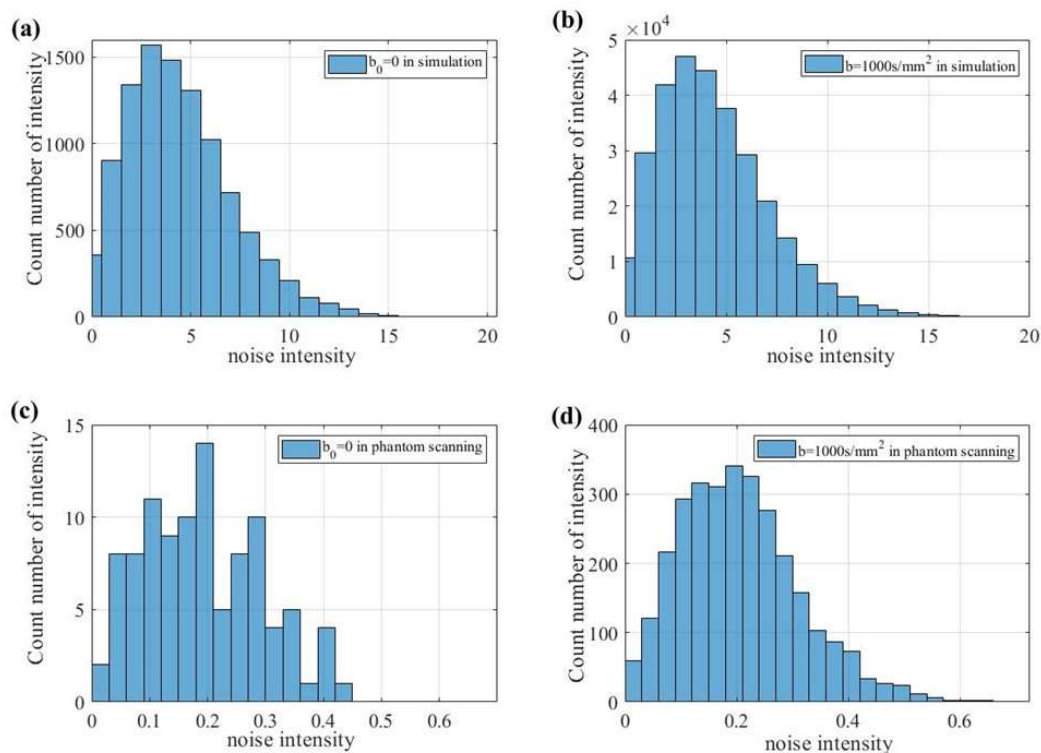


Figure 3.16: Histograms of noise distribution for  $N=30$  resulting from simulation and phantom experiment. (a) Statistic noise data of in simulation for  $b=0$ . (b) Statistic noise data in simulation for  $b=1000 \text{ s/mm}^2$ . (c) statistic noise data within the phantom image at  $b=0$ . (d) statistic noise data within the phantom images (30 directions) at  $b=1000 \text{ s/mm}^2$ .

## 4 DISCUSSION

### 4.1 Tailored diffusion gradient scheme for peripheral nerves

The optimized gradient schemes published so far were designed without consideration for the preferential direction of the imaged anatomical structure. Regardless of the respective algorithm (uniform principal, geometric shapes or electrostatic repulsion), the gradient vector scheme is designed to cover the sphere of possible directions as uniformly as possible. The higher the number of gradient directions, the more precise the directional resolution; however, this comes at the cost of long acquisition time (Jones *et al.*, 1999; Papadakis *et al.*, 1999; Xing *et al.*, 1997). Uniformly distributed gradient schemes are widely applied in DTI of the brain as there is a wide variety of fiber directions as well as fiber branching and fiber crossing. However, even in the brain there are substructures that show a limited range of directions, e.g. the corticospinal tract. Peng and Arfanakis showed that in this case it might be advantageous to use a non-uniformly distributed set of gradients (Peng and Arfanakis, 2007). They performed their simulations and experiments in structures with higher FA (around 0.8) than that of the peripheral nerves and used only 6 directions. Peng *et al.* used the ICOSA6 gradient scheme (Hasan *et al.*, 2001) and adjusted the gradient vector distribution to minimize the total variance of FA for tensors whose primary eigenvectors were uniformly scattered within a cone with a 30° opening angle around the Z-axis. They showed that a gradient scheme which is uniformly distributed in space is not the ideal scheme if the imaged structure has a limited range of orientation. A restriction of the gradient scheme to diffusion directions close to the axis of the imaged structure was also applied by Yanasak and coworkers (Yanasak *et al.*, 2008). They also found that by restricting the phase encoding directions to a cone aligned to the preferred direction of the structure, the accuracy of FA increased.

Although the present study uses a different gradient distribution and different numbers of gradients than the studies of Peng *et al.* and Yanasak *et al.*, we could confirm the finding that restricting the gradient directions to a cone aligned to the direction of the nerve produces more reliable FA than the uniformly distributed gradient scheme. Depending on the FA of the structure, a cone with  $\Theta_{\max}$  of 45-60° was sufficient for a reliable determination of FA although the condition number called for larger  $\Theta_{\max}$ . Furthermore, the tailored DGV performed equally well as the Jones- and DSM schemes in case of slight variation of the structure orientation, and

performed better than the gradient scheme used by the manufacturer, when using only the minimum number of gradient directions.

The study presented here also shows that the number of gradient vectors is an important factor influencing the reliability of FA determination.

Principally, the diffusion tensor can be estimated from one image with  $b_0$  and six diffusion weighted images (encoding gradients applied along six non-collinear orientations). However, due to noise and more complicated structures such as fiber crossings and fiber branching, studies have revealed that the minimum number of non-collinear encoding directions for a robust estimation of FA is between 18 and 21 (Bastin *et al.*, 1998). In contrast to the study of Bastin *et al.*, Jones found in a simulation study that the minimum number of diffusion gradients for a robust estimation of FA is 20, and 30 for a robust estimation of the eigenvectors and the mean diffusivity (Jones, 2004). For DTI of white matter, such a high number of gradient directions is reasonable because there is no prior knowledge of the direction of the tissue structure. An alternative to a high number of gradient directions could be the use of only a basic set of gradient directions in addition to signal averaging. However, Ni and coworkers found that for a given acquisition time, a gradient scheme with a high number of diffusion directions is superior to the use of a low number of diffusion directions in addition to signal averaging, as it reveals more reliable FA (Ni *et al.*, 2006).

In the present study, it has been shown that in case of predictable and limited directions of the fibers within the imaged structure, it is possible to narrow down the range of the gradients; nevertheless, the use of more non-collinear gradients was beneficial for an accurate calculation of the parameter FA. In contrast to the study of Yanasak (Yanasak *et al.*, 2008), which used 15 to 36 gradient directions, the present study also examined whether a lower number of non-collinear gradients is sufficient to reliably calculate FA. The results showed that with the lowest possible number of gradients ( $N=6$ ), there is a systematic error in FA even for high  $\Theta$ . However, when using 10 or more non-collinear gradients, FA could be determined reliably for  $\Theta_{\max} \geq 60^\circ$ . This may be due to the fact, that the majority of diffusion information in a highly oriented tissue is contained in the cone with  $\Theta$  between  $15^\circ$  and  $45^\circ$ , as shown by Yanasak and coworkers (Yanasak *et al.*, 2008).

In our study we restricted the range of FA to 0.4 – 0.8 to match the situation in peripheral nerves. Several groups have shown that FA is within this range for healthy subjects of different age (Kronlage *et al.*, 2018) and for patients with different types of nerve pathology (Guggenberger *et al.*, 2012; Simon *et al.*, 2017). The present study showed, that  $\Theta_{\max}$  slightly

varied between  $45^\circ$  and  $60^\circ$  depending on the given FA and N. However, for  $\Theta_{\max} \geq 60^\circ$  all gradient schemes performed well.

The condition number (CN) of the DGV scheme developed in the present study was in the range of the CN values determined from other established gradient schemes, but produced higher values than the Jones and DSM schemes. However, we expected higher CN values for the DGV scheme than for schemes with uniform gradient distribution, as uniform gradient distribution should in theory be least sensitive to noise and other input errors (Skare *et al.*, 2000a).

A systematic input error to a non-uniform gradient scheme occurs if the structure orientation does not match the axis of the diffusion gradient cone. The present study, however, could show that the developed DGV scheme is insensitive to small deviations ( $\leq 30^\circ$ ) between structure- and cone axis. This condition is valid for all major peripheral nerves (e.g. sciatic nerve, peroneal nerve, tibial nerve), if the patient is positioned appropriately within the scanner.

## 4.2 Robust noise correction method in DTI

Noise and its correction is an important topic in diffusion, particularly due to the extremely low SNR in high spatial resolution PNS DTI. The noise in the DW images propagates into the diffusion tensor elements and produces systematic errors and uncertainties in parameters calculated from DTI, such as FA (Jones and Basser, 2004).

To correct for noise effectively, prior knowledge of the noise distribution pattern is mandatory. However, it is very difficult to precisely describe the noise distribution because there are several sources of noise which exhibit different noise properties. Noise arising from RF electronics can be described well by a probability distribution function (McVeigh *et al.*, 1985). Noise arising from physiological processes, on the other hand, has no defined distribution and is difficult to model (Brooks *et al.*, 2013).

It is well accepted that in magnitude MR images, noise arising from hardware components follows the Rayleigh distribution. Several studies have shown this distribution and have developed methods to reduce this noise component (Dietrich *et al.*, 2001; Gudbjartsson and Patz, 1995; Skare *et al.*, 2000b). There are many papers on noise reduction by hardware improvement (Kathiravan and Kanakaraj, 2013) and sequence optimization (Lagana *et al.*,

2010; Nana *et al.*, 2008). In comparison to this, however, a-posteriori noise correction methods are discussed and applied less commonly. So far, there are mainly two different methods for noise correction, which were developed in the 1990s: The power image method (Miller and Joseph, 1993) and correction factor method (Gudbjartsson and Patz, 1995). Both methods, however, have not yet been applied for DTI in practice. In the present work, the two methods were applied for the first time in DTI, to examine their effectiveness and feasibility in DTI of the PNS in particular.

The results revealed that the power image method is the most effective and robust method and lead to correction of systematic errors (elimination of FA bias) and to correction of the statistic errors (decrease of FWHM). The method worked well regardless of the method used for combination of the coil channels (AC and SOS). In contrast, the correction factor method using the power of deviation from noise showed good results for AC but not for SOS. The correction factor method using the mean of noise values did not lead to a substantial reduction of systematic and statistic FA arising from noise. In the phantom study, the power image method again performed best and lead to the lowest FWHM; furthermore, the measured FA was closest to that given by the phantom manufacturer. The efficacy of the power image method was independent from the number of diffusion gradients used.

Although the correction factor method based on the mean of noise did not perform well in the simulation study, it was able to reduce the FA bias in the phantom study. However, it could not significantly decrease the FWHM, i.e. it could not address the statistical error. This is in contrast to its use in routine magnitude MR images, where it is able to effectively correct for noise (McGibney and Smith, 1993). The most likely reason for the failure in FA correction is the insufficient correction of the signal intensity. From equation 2.25, the signal magnitude in first order can be approximated as follows:

$$M \approx \sqrt{A_R^2 + A_I^2 + 2 * SNR * n_R < n_R > + 2 * SNR * n_I < n_I > + < n_R^2 > + < n_I^2 >}$$

With  $n_R \approx < n_R >$  and  $n_I \approx < n_I >$ , the term  $2 * SNR * n_R < n_R > + 2 * SNR * n_I < n_I > + < n_R^2 > + < n_I^2 >$  can be approximated by

$$(2 * SNR + 1)(< n_R^2 > + < n_I^2 >)$$

Which falls in the range of [ $< n_R^2 > + < n_I^2 >$ ,  $(2 * SNR + 1)(< n_R^2 > + < n_I^2 >)$ ] according to value of SNR, while the correction of  $\sigma^2 = \frac{2}{\pi} * (\bar{M}_0)^2 \approx 0.64 * (< n_R^2 > + < n_I^2 >)$



is obviously out of this range. This shows that the correction of signal intensity is not sufficient, even in the case of  $SNR=1$ . This under-correction of signal intensities is the reason why the method failed to correct for the systematic and statistical errors in FA.

In contrast, the correction factor method based on the power of deviation from the background (equation 2.29) is actually the direct transformation of powered true variance which performed better than using mean of noise.

In the present study, we used different coil combination modes: SOS and AC. Both combination modes can be used in clinical MRI scanning, yet sometimes the mode is changed within a study. This is critical when using the correction factor method, because SOS produces a higher noise floor than AC while the correction factor method worked well for AC, but does not for SOS.

A general problem in DTI experiments is the definition of SNR, because SNR depends not only on the b-value, but also on the anatomical location and the direction of the diffusion gradient. Therefore, most studies dealing with SNR in DTI refer to the SNR of the  $b_0$  image. For DTI in the PNS, the application relevant for this study, SNR is about 6 in the images without diffusion weighting and is between 1 and 3 in the diffusion weighted images. According to Gudbjartsson and Patz this is the range, where noise is no longer governed by Gaussian distribution (Gudbjartsson and Patz, 1995). This is in accordance with our findings from both simulation and phantom study, where we found that the noise was governed by Raleigh distribution.

## 5 SUMMARY

Diffusion Tensor Imaging (DTI) is a method widely used in research and clinical application, particularly for the depiction and connectivity analysis of the white matter tracts within the brain. Regardless of the many possibilities offered by DTI, this method suffers from an inherently low signal-to-noise ratio (SNR) as both the long echo time and the diffusion gradients have a signal-reducing effect. The SNR is particularly low if a high spatial resolution is mandatory, e.g. in DTI of peripheral nerves. Low SNR leads to systematic and statistical errors in parameters derived from DTI, e.g. in fractional anisotropy (FA). This downside can be overcome in part by increasing the number of diffusion directions and by applying methods for post-hoc noise correction. It is generally accepted that for anatomical structures of unknown orientation, the most robust method is to uniformly cover the space with the diffusion gradients. If the preferred direction of the anatomical structure is known beforehand, however, it might be advantageous to restrict the diffusion gradients to a cone centered around the axis of the structure. The aim of this thesis was to develop an optimized DTI method with increased accuracy and reliability for application in peripheral nerves. Two methods to reduce noise bias were examined: (1) A newly developed tailored diffusion gradient vector (DGV) scheme with vectors restricted to a cone with an aperture angle  $\Theta$  and (2) different post-hoc noise correction methods.

The examinations were performed using Monte Carlo simulation based on realistic assumptions of diffusivity, FA and noise levels that were obtained from clinical examinations and studies performed in the Department of Neuroradiology, University Hospital Heidelberg. Furthermore, the methods were tested in a custom-built phantom that simulates diffusion in peripheral nerves (FA=0.65) using a 3 Tesla whole-body Magnetic Resonance (MR) scanner. In both parts of the study systematic deviations of FA from the ground truth and statistical errors of FA were measured to determine the accuracy and reliability of DTI incorporating these methods for noise correction. The newly developed tailored DGV scheme was also compared to gradient schemes with uniform coverage (Jones scheme, downhill simplex method (DSM) scheme, gradient scheme of the manufacturer) by means of their condition number (CN).

The study showed that the tailored DGV is able to measure FA accurately if  $\Theta$  is at least  $45^\circ$  or  $60^\circ$ . This minimum  $\Theta$  depends on the number of gradient directions and on the FA of the

measured structure. Generally, the tailored DGV performed better, the higher the FA value and the higher the number of gradients. For  $N=30$ , DGV allowed accurate determination of FA for the whole range of FA examined in this study (0.4 – 0.8) for  $\Theta \geq 45^\circ$ . It could also be shown that a small tilt of the structure (up to  $30^\circ$ ) from the cone axis does not impact the accuracy of the tailored DGV scheme. The condition number of the tailored DGV scheme was higher than CN of the Jones' and the DSM scheme for  $N=6$ , and higher than CN of the DSM scheme for  $N \geq 10$ ; however, it cannot be expected that a method restricting the gradient vectors to a limited space performs as well as other schemes with uniform gradient distribution when it comes to the susceptibility to small perturbances. Nevertheless, CN of the tailored DGV scheme was in the same range as the other schemes.

Comparing of the different post-hoc noise correction techniques revealed that the power image method is the most effective and robust method, eliminating the systematic errors in FA as well as the statistic errors. The efficacy of the power image method is independent from the number of diffusion gradients used. Furthermore, the method works reliably regardless of the method used for coil combination (sum of squares or adaptive combination). In contrast, both correction factor methods used in this study showed less or no correction and depended on the method of coil combination.

In conclusion, the tailored DGV scheme developed in this study in combination with the power image method for post-hoc noise correction allow for DTI of peripheral nerves with high SNR, high accuracy and reliability of the parameters determined from DTI and without further increasing acquisition time. Therefore, the results of this study call for application of the tailored DGV scheme and the power image method in clinical practice and in research.

## **Zusammenfassung auf Deutsch:**

Die Diffusions-Tensor-Bildgebung (DTI) ist eine in Forschung und Klinik weit verbreitete Methode, insbesondere zur Darstellung und Konnektivitätsanalyse der Weißen Hirnsubstanz. Ungeachtet der vielen Möglichkeiten, die DTI bietet, leidet dieses Verfahren unter einem inhärent niedrigen Signal-Rausch-Verhältnis (SNR), da sowohl die lange Echozeit als auch die Diffusionsgradienten das Signal schwächen. Das SNR ist vor allem bei hoher Ortsauflösung niedrig, z.B. bei der DTI von Nerven. Ein niedriges SNR führt zu systematischen und statistischen Fehlern bei Parametern, die aus der DTI berechnet werden, z.B. bei der fraktionalen Anisotropie (FA). Ein niedriges SNR kann teilweise kompensiert werden, indem die Zahl der Diffusionsrichtungen erhöht wird oder Methoden für eine a posteriori Rauschkorrektur verwendet werden. Das robusteste Verfahren bei anatomischen Strukturen mit unbekannter Orientierung besteht darin, die Diffusionsgradienten gleichmäßig im Raum zu verteilen. Wenn jedoch die Vorzugsrichtung der anatomischen Struktur im Voraus bekannt ist, kann es vorteilhaft sein, die Diffusionsgradienten auf einen um die Achse der Struktur zentrierten Kegel zu beschränken. Ziel dieser Arbeit war es, eine DTI-Methode mit hoher Genauigkeit und Zuverlässigkeit für die Anwendung in peripheren Nerven zu entwickeln. Es wurden zwei Methoden zur Reduzierung des Bildrauschens untersucht: (1) Ein neu entwickeltes Schema von Diffusionsgradienten-Vektoren (DGV), bei dem die Vektoren auf einen Kegel mit einem Öffnungswinkel  $\Theta$  um die Achse des Nerven beschränkt sind und (2) verschiedene Methoden für eine a posteriori Rauschkorrektur.

Hierzu wurden Monte-Carlo-Simulationen durchgeführt, die auf realistischen Werten für Diffusivität, FA und Rauschen beruhen, die aus klinischen Untersuchungen und Studien gewonnen wurden. Außerdem wurden die Methoden in einem speziell angefertigten Phantom getestet, das die Diffusion in peripheren Nerven simuliert (FA = 0,65). Diese Untersuchungen wurden an einem 3-Tesla-Ganzkörper-Magnetresonanz (MR)-Scanner durchgeführt. Um die Genauigkeit und Zuverlässigkeit der DTI unter Verwendung der jeweiligen Meß- oder Korrekturverfahren zu bestimmen, wurden systematische Abweichungen von FA vom Ausgangswert und der statistische Fehler von FA gemessen. Das neu entwickelte DGV-Schema mit eingeschränkter Raumabdeckung wurde mit Gradientenschemata mit uniformer Raumabdeckung (Jones, Downhill-Simplex-Methode (DSM), Gradientenschema des Herstellers) anhand ihrer Konditionszahl (CN) verglichen.

Die Studie zeigte, dass mit dem neu entwickelten DGV Schema FA mit hoher Genauigkeit gemessen werden kann, wenn  $\Theta$  mindestens  $45^\circ$  bzw.  $60^\circ$  beträgt. Das minimale  $\Theta$  hängt dabei von der Zahl der Gradientenrichtungen und von FA ab. Grundsätzlich ist die Genauigkeit des DGV Schemas umso besser, je höher der FA-Wert und je größer die Zahl der Gradienten ist. Für  $N = 30$  ermöglichte die DGV eine genaue Bestimmung der FA für den gesamten in dieser Studie untersuchten FA-Bereich (0,4 - 0,8), wenn  $\Theta \geq 45^\circ$  war. Es konnte gezeigt werden, dass bei Verwendung des neuen DGV-Schemas eine geringfügige Neigung der untersuchten Struktur ( $\leq 30^\circ$ ) keinen Einfluss auf die Genauigkeit von FA hat. CN des entwickelten DGV-Schemas war für  $N = 6$  höher als CN des Jones-Schemas und des DSM-Schemas; für  $N \geq 10$  war CN des neuen DSM-Schemas kleiner als die des Jones-Schemas. Es ist jedoch auch nicht zu erwarten, dass ein Verfahren, das die Gradientenvektoren auf ein begrenztes Segment des Raums konzentriert, ebenso unempfindlich gegenüber Störungen ist wie Schemata mit gleichmäßiger Gradientenverteilung. Trotzdem lag die CN des neuen DGV-Verfahrens in der gleichen Größenordnung wie die der anderen Verfahren.

Ein Vergleich der verschiedenen a posteriori Korrekturverfahren ergab, dass die Power-Image-Methode die effektivste und robusteste Methode ist und sowohl die systematischen als auch die statistischen Fehler von FA kompensiert. Die Effizienz der Power-Image-Methode ist unabhängig von der Anzahl der verwendeten Diffusionsgradienten. Darüber hinaus funktioniert das Verfahren zuverlässig - unabhängig von der für die Spulenkombination verwendeten Methode (Quadratsumme versus adaptive Kombination). Im Gegensatz dazu waren beide in dieser Studie verwendeten Korrekturfaktor-Verfahren weniger effizient hinsichtlich der Korrektur des Rauschens; außerdem hing die Korrektoreffizienz von der Methode der Spulenkombination ab.

Zusammenfassend lässt sich festhalten, dass eine Kombination des neu entwickelten DGV-Schemas mit der Power-Image-Methode für die a posteriori Korrektur es ermöglicht, DTI von peripheren Nerven mit hohem SNR, hoher Genauigkeit und Zuverlässigkeit der berechneten Parameter (z.B. FA) durchzuführen, ohne dass zusätzliche Akquisitionszeit erforderlich ist. Bislang ist allerdings eine Anwendung dieser neu entwickelten und getesteten Verfahren in Studien bzw. bei klinischen Untersuchungen noch nicht erfolgt.

## 6 REFERENCES

- Alexander, A. L., Hasan, K. M., Lazar, M., Tsuruda, J. S. and Parker, D. L. (2001). **Analysis of partial volume effects in diffusion-tensor MRI**. *Magn Reson Med* 45, 770-780.
- Alves, G. S., Sudo, F. K., Alves, C. E. O., Ericeira-Valente, L., Moreira, D. M., Engelhardt, E. and Laks, J. (2012). **Diffusion tensor imaging studies in vascular disease: A review of the literature**. *Dement Neuropsychol* 6, 158-163, doi: 10.1590/S1980-57642012DN06030008.
- Assaf, Y. and Basser, P. J. (2005). **Composite hindered and restricted model of diffusion (CHARMED) MR imaging of the human brain**. *Neuroimage* 27, 48-58, doi: 10.1016/j.neuroimage.2005.03.042.
- Aung, W. Y., Mar, S. and Benzinger, T. L. (2013). **Diffusion tensor MRI as a biomarker in axonal and myelin damage**. *Imaging Med* 5, 427-440, doi: 10.2217/iim.13.49.
- Baete, S. H., Cho, G. and Sigmund, E. E. (2013). **Multiple-echo diffusion tensor acquisition technique (MEDITATE) on a 3T clinical scanner**. *NMR Biomed* 26, 1471-1483, doi: 10.1002/nbm.2978.
- Baliyan, V., Das, C. J., Sharma, R. and Gupta, A. K. (2016). **Diffusion weighted imaging: Technique and applications**. *World J Radiol* 8, 785-798, doi: 10.4329/wjr.v8.i9.785.
- Basser, P. J., Mattiello, J. and LeBihan, D. (1994). **MR diffusion tensor spectroscopy and imaging**. *Biophys J* 66, 259-267, doi: 10.1016/S0006-3495(94)80775-1.
- Bastin, M. E., Armitage, P. A. and Marshall, I. (1998). **A theoretical study of the effect of experimental noise on the measurement of anisotropy in diffusion imaging**. *Magn Reson Imaging* 16, 773-785.
- Basu, S., Fletcher, T. and Whitaker, R. (2006). **Rician noise removal in diffusion tensor MRI**. *Med Image Comput Comput Assist Interv* 9, 117-125.
- Bernstein, M. A., King, K. F. and Zhou, X. J. (2004). **Handbook of MRI Pulse Sequences, CHAPTER 17 - ADVANCED PULSE SEQUENCE TECHNIQUES**, Elsevier Science, pp. 802-954.
- Bevington, P. and Robinson, D. K. (2003). **Data Reduction and Error Analysis for the Physical Sciences.**, 3rd. edn, McGraw-Hill Education, Boston, MA, United States.

- Brooks, J. C., Faull, O. K., Pattinson, K. T. and Jenkinson, M. (2013). **Physiological noise in brainstem FMRI**. *Front Hum Neurosci* 7, 623, doi: 10.3389/fnhum.2013.00623.
- Brown, R. (1828). **XXVII. A brief account of microscopical observations made in the months of June, July and August 1827, on the particles contained in the pollen of plants; and on the general existence of active molecules in organic and inorganic bodies**. *The Philosophical Magazine* 4, 161-173, doi: 10.1080/14786442808674769.
- Budde, M. D., Kim, J. H., Liang, H. F., Russell, J. H., Cross, A. H. and Song, S. K. (2008). **Axonal injury detected by in vivo diffusion tensor imaging correlates with neurological disability in a mouse model of multiple sclerosis**. *NMR Biomed* 21, 589-597, doi: 10.1002/nbm.1229.
- Chhabra, A., Thakkar, R. S., Andreisek, G., Chalian, M., Belzberg, A. J., Blakeley, J., Hoke, A., Thawait, G. K., Eng, J. and Carrino, J. A. (2013). **Anatomic MR imaging and functional diffusion tensor imaging of peripheral nerve tumors and tumorlike conditions**. *AJNR Am J Neuroradiol* 34, 802-807, doi: 10.3174/ajnr.A3316.
- Chianca, V., Albano, D., Messina, C., Cinnante, C. M., Triulzi, F. M., Sardanelli, F. and Sconfienza, L. M. (2017). **Diffusion tensor imaging in the musculoskeletal and peripheral nerve systems: from experimental to clinical applications**. *European Radiology Experimental* 1, 12, doi: 10.1186/s41747-017-0018-1.
- Damon, B. M. (2008). **Effects of image noise in muscle diffusion tensor (DT)-MRI assessed using numerical simulations**. *Magn Reson Med* 60, 934-944, doi: 10.1002/mrm.21707.
- Dietrich, O., Heiland, S. and Sartor, K. (2001). **Noise correction for the exact determination of apparent diffusion coefficients at low SNR**. *Magn Reson Med* 45, 448-453.
- Dietrich, O., Raya, J. G., Reeder, S. B., Reiser, M. F. and Schoenberg, S. O. (2007). **Measurement of signal-to-noise ratios in MR images: influence of multichannel coils, parallel imaging, and reconstruction filters**. *J Magn Reson Imaging* 26, 375-385, doi: 10.1002/jmri.20969.
- Doob, J. L. (1942). **The Brownian Movement and Stochastic Equations**. *Annals of Mathematics* 43, 351-369, doi: 10.2307/1968873.
- Douek, P., Turner, R., Pekar, J., Patronas, N. and Le Bihan, D. (1991). **MR color mapping of myelin fiber orientation**. *J Comput Assist Tomogr* 15, 923-929.

- Einstein, A. (1905). **Über die von der molekularkinetischen Theorie der Wärme geforderte Bewegung von in ruhenden Flüssigkeiten suspendierten Teilchen.** *Annalen der Physik* 322, 549-560, doi: 10.1002/andp.19053220806.
- Farrance, I. and Frenkel, R. (2012). **Uncertainty of Measurement: A Review of the Rules for Calculating Uncertainty Components through Functional Relationships.** *Clin Biochem Rev* 33, 49-75.
- Farrell, J. A., Landman, B. A., Jones, C. K., Smith, S. A., Prince, J. L., van Zijl, P. C. and Mori, S. (2007). **Effects of signal-to-noise ratio on the accuracy and reproducibility of diffusion tensor imaging-derived fractional anisotropy, mean diffusivity, and principal eigenvector measurements at 1.5 T.** *J Magn Reson Imaging* 26, 756-767, doi: 10.1002/jmri.21053.
- Farzinfar, M., Li, Y., Verde, A. R., Oguz, I., Gerig, G. and Styner, M. A. (2013). **DTI Quality Control Assessment via Error Estimation From Monte Carlo Simulations.** *Proc SPIE Int Soc Opt Eng* 8669, 1667549, doi: 10.1117/12.2006925.
- Geva, T. (2006). **Magnetic resonance imaging: historical perspective.** *J Cardiovasc Magn Reson* 8, 573-580.
- Gudbjartsson, H. and Patz, S. (1995). **The Rician distribution of noisy MRI data.** *Magn Reson Med* 34, 910-914.
- Guggenberger, R., Markovic, D., Eppenberger, P., Chhabra, A., Schiller, A., Nanz, D., Prussmann, K. and Andreisek, G. (2012). **Assessment of median nerve with MR neurography by using diffusion-tensor imaging: normative and pathologic diffusion values.** *Radiology* 265, 194-203, doi: 10.1148/radiol.12111403.
- Gullmar, D., Jaap, T., Bellemann, M. E., Haueisen, J. and Reichenbach, J. R. (2002). **DTI measurements of isotropic and anisotropic media.** *Biomed Tech (Berl)* 47 Suppl 1 Pt 1, 420-422.
- Hasan, K. M., Parker, D. L. and Alexander, A. L. (2001). **Comparison of gradient encoding schemes for diffusion-tensor MRI.** *J Magn Reson Imaging* 13, 769-780.
- Henkelman, R. M. (1985). **Measurement of signal intensities in the presence of noise in MR images.** *Med Phys* 12, 232-233, doi: 10.1118/1.595711.
- Jaffe, J. S. (2005). **Three-Dimensional Probability Density Functions via Tomographic Inversion.** *SIAM Journal on Applied Mathematics* 65, 1506-1525.



- Jeon, T., Fung, M. M., Koch, K. M., Tan, E. T. and Sneag, D. B. (2018). **Peripheral nerve diffusion tensor imaging: Overview, pitfalls, and future directions**. *J Magn Reson Imaging* 47, 1171-1189, doi: 10.1002/jmri.25876.
- Jones, D. K. (2004). **The effect of gradient sampling schemes on measures derived from diffusion tensor MRI: a Monte Carlo study**. *Magn Reson Med* 51, 807-815, doi: 10.1002/mrm.20033.
- Jones, D. K. and Basser, P. J. (2004). **"Squashing peanuts and smashing pumpkins": how noise distorts diffusion-weighted MR data**. *Magn Reson Med* 52, 979-993, doi: 10.1002/mrm.20283.
- Jones, D. K., Horsfield, M. A. and Simmons, A. (1999). **Optimal strategies for measuring diffusion in anisotropic systems by magnetic resonance imaging**. *Magn Reson Med* 42, 515-525, doi: 10.1002/(Sici)1522-2594(199909)42:3<515::Aid-Mrm14>3.0.Co;2-Q.
- Kathiravan, S. and Kanakaraj, J. (2013). **A review on potential issues and challenges in MR imaging**. *ScientificWorldJournal* 2013, 783715, doi: 10.1155/2013/783715.
- Khalil, C., Budzik, J. F., Kermarrec, E., Balbi, V., Le Thuc, V. and Cotten, A. (2010). **Tractography of peripheral nerves and skeletal muscles**. *Eur J Radiol* 76, 391-397, doi: 10.1016/j.ejrad.2010.03.012.
- Kronlage, M., Schwehr, V., Schwarz, D., Godel, T., Uhlmann, L., Heiland, S., Bendszus, M. and Baumer, P. (2018). **Peripheral nerve diffusion tensor imaging (DTI): normal values and demographic determinants in a cohort of 60 healthy individuals**. *Eur Radiol* 28, 1801-1808, doi: 10.1007/s00330-017-5134-z.
- Lagana, M., Rovaris, M., Ceccarelli, A., Venturelli, C., Marini, S. and Baselli, G. (2010). **DTI parameter optimisation for acquisition at 1.5T: SNR analysis and clinical application**. *Comput Intell Neurosci*, 254032, doi: 10.1155/2010/254032.
- Landman, B. A., Farrell, J. A., Huang, H., Prince, J. L. and Mori, S. (2008). **Diffusion tensor imaging at low SNR: nonmonotonic behaviors of tensor contrasts**. *Magn Reson Imaging* 26, 790-800, doi: 10.1016/j.mri.2008.01.034.
- Landman, B. A., Farrell, J. A., Jones, C. K., Smith, S. A., Prince, J. L. and Mori, S. (2007). **Effects of diffusion weighting schemes on the reproducibility of DTI-derived fractional anisotropy, mean diffusivity, and principal eigenvector measurements at 1.5T**. *Neuroimage* 36, 1123-1138, doi: 10.1016/j.neuroimage.2007.02.056.

- Larsson, E. G., Erdogmus, D., Yan, R., Principe, J. C. and Fitzsimmons, J. R. (2003). **SNR-optimality of sum-of-squares reconstruction for phased-array magnetic resonance imaging**. *J Magn Reson* *163*, 121-123.
- Laun, F. B., Schad, L. R., Klein, J. and Stieltjes, B. (2009). **How background noise shifts eigenvectors and increases eigenvalues in DTI**. *MAGMA* *22*, 151-158, doi: 10.1007/s10334-008-0159-6.
- Le Bihan, D. (2014). **Diffusion MRI: what water tells us about the brain**. *EMBO Mol Med* *6*, 569-573, doi: 10.1002/emmm.201404055.
- Le Bihan, D., Breton, E., Lallemand, D., Grenier, P., Cabanis, E. and Laval-Jeantet, M. (1986). **MR imaging of intravoxel incoherent motions: application to diffusion and perfusion in neurologic disorders**. *Radiology* *161*, 401-407, doi: 10.1148/radiology.161.2.3763909.
- McGibney, G. and Smith, M. R. (1993). **An unbiased signal-to-noise ratio measure for magnetic resonance images**. *Med Phys* *20*, 1077-1078, doi: 10.1118/1.597004.
- McVeigh, E. R., Henkelman, R. M. and Bronskill, M. J. (1985). **Noise and filtration in magnetic resonance imaging**. *Med Phys* *12*, 586-591, doi: 10.1118/1.595679.
- Michalet, X. (2010). **Mean square displacement analysis of single-particle trajectories with localization error: Brownian motion in an isotropic medium**. *Phys Rev E Stat Nonlin Soft Matter Phys* *82*, 041914, doi: 10.1103/PhysRevE.82.041914.
- Miller, A. J. and Joseph, P. M. (1993). **The use of power images to perform quantitative analysis on low SNR MR images**. *Magn Reson Imaging* *11*, 1051-1056.
- Moseley, M. E., Cohen, Y., Mintorovitch, J., Chileuitt, L., Shimizu, H., Kucharczyk, J., Wendland, M. F. and Weinstein, P. R. (1990). **Early detection of regional cerebral ischemia in cats: comparison of diffusion- and T2-weighted MRI and spectroscopy**. *Magn Reson Med* *14*, 330-346.
- Nana, R., Zhao, T. and Hu, X. (2008). **Single-shot multiecho parallel echo-planar imaging (EPI) for diffusion tensor imaging (DTI) with improved signal-to-noise ratio (SNR) and reduced distortion**. *Magn Reson Med* *60*, 1512-1517, doi: 10.1002/mrm.21770.

- Naraghi, A. M., Awdeh, H., Wadhwa, V., Andreisek, G. and Chhabra, A. (2015). **Diffusion tensor imaging of peripheral nerves**. *Semin Musculoskelet Radiol* 19, 191-200, doi: 10.1055/s-0035-1546824.
- Neetu, S., Sunil, K., Ashish, A., Jayantee, K. and Usha Kant, M. (2016). **Microstructural abnormalities of the trigeminal nerve by diffusion-tensor imaging in trigeminal neuralgia without neurovascular compression**. *Neuroradiol J* 29, 13-18, doi: 10.1177/1971400915620439.
- Ni, H., Kavcic, V., Zhu, T., Ekholm, S. and Zhong, J. (2006). **Effects of number of diffusion gradient directions on derived diffusion tensor imaging indices in human brain**. *AJNR Am J Neuroradiol* 27, 1776-1781.
- Oppedal, K. (2005) **Quantitative Analysis of Magnetic Resonance Diffusion Tensor Imaging of the Human Brain – The effect of varying number of acquisitions and number of diffusion sensitizing directions**. Master thesis, The University of Bergen. URL: <http://hdl.handle.net/1956/1264> [Stand:09.06.2006].
- Ozcan, A. (2005). **(Mathematical) Necessary conditions for the selection of gradient vectors in DTI**. *J Magn Reson* 172, 238-241, doi: 10.1016/j.jmr.2004.10.013.
- Paniandi, V., George, J., Goh, K. J. and Tan, L. K. (2018). **MR neurography of median nerve using diffusion tensor imaging (DTI) and its efficacy to diagnose carpal tunnel syndrome in Malaysian population**. *Neurology Asia* 23(1), 17-25.
- Papadakis, N. G., Xing, D., Huang, C. L., Hall, L. D. and Carpenter, T. A. (1999). **A comparative study of acquisition schemes for diffusion tensor imaging using MRI**. *J Magn Reson* 137, 67-82, doi: 10.1006/jmre.1998.1673.
- Peng, H. and Arfanakis, K. (2007). **Diffusion tensor encoding schemes optimized for white matter fibers with selected orientations**. *Magn Reson Imaging* 25, 147-153, doi: 10.1016/j.mri.2006.10.013.
- Pierpaoli, C., Jezzard, P., Basser, P. J., Barnett, A. and Di Chiro, G. (1996). **Diffusion tensor MR imaging of the human brain**. *Radiology* 201, 637-648, doi: 10.1148/radiology.201.3.8939209.
- Polzehl, J. and Tabelow, K. (2016). **Low SNR in Diffusion MRI Models**. *Journal of the American Statistical Association* 111, 1480-1490, doi: 10.1080/01621459.2016.1222284.

- Poonawalla, A. H. and Zhou, X. J. (2004). **Analytical error propagation in diffusion anisotropy calculations.** *J Magn Reson Imaging* 19, 489-498, doi: 10.1002/jmri.20020.
- Schmid, A. B., Campbell, J., Hurley, S. A., Jbabdi, S., Andersson, J. L., Jenkinson, M., Bangerter, N. K., Bennett, D. L., Tracey, I., Frost, R. and Clare, S. (2018). **Feasibility of Diffusion Tensor and Morphologic Imaging of Peripheral Nerves at Ultra-High Field Strength.** *Invest Radiol* 53, 705-713, doi: 10.1097/RLI.0000000000000492.
- Server, A., Graff, B. A., Josefsen, R., Orheim, T. E., Schellhorn, T., Nordhoy, W. and Nakstad, P. H. (2014). **Analysis of diffusion tensor imaging metrics for gliomas grading at 3 T.** *Eur J Radiol* 83, e156-165, doi: 10.1016/j.ejrad.2013.12.023.
- Simon, N. G., Lagopoulos, J., Paling, S., Pfluger, C., Park, S. B., Howells, J., Gallagher, T., Kliot, M., Henderson, R. D., Vucic, S. and Kiernan, M. C. (2017). **Peripheral nerve diffusion tensor imaging as a measure of disease progression in ALS.** *J Neurol* 264, 882-890, doi: 10.1007/s00415-017-8443-x.
- Skare, S., Hedehus, M., Moseley, M. E. and Li, T. Q. (2000a). **Condition number as a measure of noise performance of diffusion tensor data acquisition schemes with MRI.** *J Magn Reson* 147, 340-352, doi: 10.1006/jmre.2000.2209.
- Skare, S., Li, T., Nordell, B. and Ingvar, M. (2000b). **Noise considerations in the determination of diffusion tensor anisotropy.** *Magn Reson Imaging* 18, 659-669.
- Stein, D., Neufeld, A., Pasternak, O., Graif, M., Patish, H., Schwimmer, E., Ziv, E. and Assaf, Y. (2009). **Diffusion tensor imaging of the median nerve in healthy and carpal tunnel syndrome subjects.** *J Magn Reson Imaging* 29, 657-662, doi: 10.1002/jmri.21553.
- Stejskal, E. O. and Tanner, J. E. (1965). **Spin Diffusion Measurements: Spin Echoes in the Presence of a Time Dependent Field Gradient.** *The Journal of Chemical Physics* 42, 288-292, doi: 10.1063/1.1695690
- Tae, W. S., Ham, B. J., Pyun, S. B., Kang, S. H. and Kim, B. J. (2018). **Current Clinical Applications of Diffusion-Tensor Imaging in Neurological Disorders.** *J Clin Neurol* 14, 129-140, doi: 10.3988/jcn.2018.14.2.129.

- Takagi, T., Nakamura, M., Yamada, M., Hikishima, K., Momoshima, S., Fujiyoshi, K., Shibata, S., Okano, H. J., Toyama, Y. and Okano, H. (2009). **Visualization of peripheral nerve degeneration and regeneration: monitoring with diffusion tensor tractography**. *Neuroimage* 44, 884-892, doi: 10.1016/j.neuroimage.2008.09.022.
- Taylor, P. A., Alhamud, A., van der Kouwe, A., Saleh, M. G., Laughton, B. and Meintjes, E. (2016). **Assessing the performance of different DTI motion correction strategies in the presence of EPI distortion correction**. *Hum Brain Mapp* 37, 4405-4424, doi: 10.1002/hbm.23318.
- Turner, R., Le Bihan, D., Maier, J., Vavrek, R., Hedges, L. K. and Pekar, J. (1990). **Echo-planar imaging of intravoxel incoherent motion**. *Radiology* 177, 407-414, doi: 10.1148/radiology.177.2.2217777.
- Vaeggemose, M., Pham, M., Ringgaard, S., Tankisi, H., Ejksjaer, N., Heiland, S., Poulsen, P. L. and Andersen, H. (2017). **Diffusion tensor imaging MR neurography for the detection of polyneuropathy in type 1 diabetes**. *J Magn Reson Imaging* 45, 1125-1134, doi: 10.1002/jmri.25415.
- Walsh, D. O., Gmitro, A. F. and Marcellin, M. W. (2000). **Adaptive reconstruction of phased array MR imagery**. *Magn Reson Med* 43, 682-690.
- Wang, J. Y., Abdi, H., Bakhadirov, K., Diaz-Arrastia, R. and Devous, M. D., Sr. (2012). **A comprehensive reliability assessment of quantitative diffusion tensor tractography**. *Neuroimage* 60, 1127-1138, doi: 10.1016/j.neuroimage.2011.12.062.
- Wirestam, R., Bibic, A., Latt, J., Brockstedt, S. and Stahlberg, F. (2006). **Denoising of complex MRI data by wavelet-domain filtering: application to high-b-value diffusion-weighted imaging**. *Magn Reson Med* 56, 1114-1120, doi: 10.1002/mrm.21036.
- Xing, D., Papadakis, N. G., Huang, C. L., Lee, V. M., Carpenter, T. A. and Hall, L. D. (1997). **Optimised diffusion-weighting for measurement of apparent diffusion coefficient (ADC) in human brain**. *Magn Reson Imaging* 15, 771-784.
- Yanasak, N., Allison, J. D., Zhao, Q., Hu, T. C. and Dhandapani, K. (2008). **Non-uniform gradient prescription for precise angular measurements using DTI**. *Med Image Comput Assist Interv* 11, 866-873.
- Zhou, Y., Narayana, P. A., Kumaravel, M., Athar, P., Patel, V. S. and Sheikh, K. A. (2014). **High resolution diffusion tensor imaging of human nerves in forearm**. *J Magn Reson Imaging* 39, 1374-1383, doi: 10.1002/jmri.24300.

## **7 PAPERS PUBLISHED**

The results of this theses were not published so far.

## 8 CURRICULUM VITAE

### PERSONAL DATA

Family Name / Given:	Ma
Name:	Bo
Birthday:	06.06.1979
Birthplace:	Peking, China
Nationality:	Chinese
Marital status:	Married, 1 Child

### EDUCATION BACKGROUND

1985 – 1991	Primary School, Peking
1991 – 1994	Middle School, Peking
1994 – 1997	High School, Peking
28.07.1997	High School Diploma

### UNIVERSITY

28.08.1997 – 28.07.2002	Bachelor of Biomedical Engineering in Capital University of Medical Science. China
01.09.2002 – 01.05.2005	Master of Biomedical Engineering in Shanghai Jiao Tong University. China

## CAREER EXPERIENCE

05/2005 – 12/2006	Clinical Specialist at Siemens Healthcare China: Clinical workflow training for customer in Head Quarter in MR sector;
12/2006 – 05/2009	MRI Instructor at Siemens AG Healthcare Germany: Delivering Technical MRI training courses globally and Participating new MRI scanner design.
05/2009 – 07/2013	MRI Instructor by Siemens Healthcare China: Setting up the global training center in China and Supporting the Clinical Application for customers.
07/2013 – Present	Doctoral student in Medical University Heidelberg in Germany.



## 9 ACKNOWLEDGEMENT

This thesis has been carried out at the Department of Neuroradiology at the Heidelberg University Hospital. During this time, the intensive collaboration with supervisors and colleagues did not only lead to a gain of expertise in my dedicated scientific subject, but also to development on a personal level. Here, I wish to express my sincere gratitude and appreciation to everyone who in one way or another have supported me:

- Prof. Dr. med. Martin Bendszus. Thank you for offering me the opportunity to work and study in this active department with its warm and harmonious atmosphere.
- Prof. Dr. rer. nat. Sabine Heiland, as my supervisor. You have been an exceptional and supportive mentor; I am very grateful for introducing me to the research field of diffusion tensor imaging. During the development of my project, you have been an invaluable source of inspiration and guidance on key points.
- Dr. sc. hum. Marcel Prager. Thank you for always offering constructive support and help both, in research and in daily work.
- Ms. Dorothea Willich, my trusted colleague. Thanks to your support with the scanning schedule, I was always able to obtain MRI data in a timely fashion which played an important role in my research progress.
- Mr. Manuel Fischer. Without your patient support in phantom design, I could not have put my idea of a diffusion phantom in practice.
- Dr. rer. nat. Volker Sturm. I enjoyed our discussion about noise pattern simulation and would like to thank you for your thorough advice on programming the simulation in MATLAB.
- Ms. Hanna Leisz. Thank you very much for editing my dissertation.

## 10 EIDESSTAATLICHE VERSICHERUNG

1. Bei der eingereichten Dissertation zu dem Thema „*Effect of Gradient Vectors Scheme and Noise Correction on Fractional Anisotropy in Diffusion Tensor Imaging of the Peripheral Nervous System*“ handelt es sich um meine eigenständig erbrachte Leistung.
2. Ich habe nur die angegebenen Quellen und Hilfsmittel benutzt und mich keiner unzulässigen Hilfe Dritter bedient. Insbesondere habe ich wörtlich oder sinngemäß aus anderen Werken übernommene Inhalte als solche kenntlich gemacht.
3. Die Arbeit oder Teile davon habe ich bislang nicht an einer Hochschule des In- oder Auslands als Bestandteil einer Prüfungs- oder Qualifikationsleistung vorgelegt.
4. Die Richtigkeit der vorstehenden Erklärungen bestätige ich.
5. Die Bedeutung der eidesstattlichen Versicherung und die strafrechtlichen Folgen einer unrichtigen oder unvollständigen eidesstattlichen Versicherung sind mir bekannt. Ich versichere an Eides statt, dass ich nach bestem Wissen die reine Wahrheit erkläre und nichts verschwiegen habe.

Heidelberg, 2019

MA, BO